Investigation of Electrochemistry using a Localized Surface Plasmon Sensor

Diplomarbeit

Dermutz Harald

Betreuer:
Dr. Takumi Sannomiya
Begutachter:
Dipl.–Chem. Dr.rer.nat. Marcel Scheideler

Laboratory of Biosensors and Bioelectronics
Swiss Federal Institute of Technology
Institute for Genomics and Bioinformatics
Graz University of Technology

Zürich, Graz im Juli 2010

Statutory Declaration

I declare that I have authored this thesis independently, that I have not used other than the declared sources / resources, and that I have explicitly marked all material which has been quoted either literally or by content from the used sources.

....	....
(Place, Date)	(Harald Dermutz)

Eidesstattliche Erklärung

Ich erkläre an Eides statt, dass ich die vorliegende Arbeit selbstständig verfasst, andere als die angegebenen Quellen/Hilfsmittel nicht benutzt, und die den benutzten Quellen wörtlich und inhaltlich entnommene Stellen als solche kenntlich gemacht habe.

....	....
(Ort, Datum)	(Harald Dermutz)

Acknowledgement

It is impossible to include all the names to thank in this acknowledgment list, however, I still list some names that are more or less directly related to this work.

First of all, I would like to thank Prof. Janos Vörös for giving me the opportunity to work at his institute, all his patience with me and his warm and friendly character. It is needless to say that it was a great experience for me. Takumi Sannoyama, I thank for his wonderful support during my work as my supervisor and his amazing patience with me. I enjoyed working under his supervision. I was always impressed how fast he could give me an answer to the numerous questions I asked him. It is impossible to find the right words to express my gratitude. Stephen Wheeler I thank for helping me to resolve mechanical problems and building the flow cell used in this work. Andreas Dahlin i want to thank for his online support on electrochemistry when Takumi was not around. Orane Guillaume-Gentil I want to thank for all the valuable discussions and her help with all the chemistry related questions. I also want to thank all those friends and people I got to know at the LBB. I will never forget that time with you. Thank you Norma Graf, Marta Bally, Ana Sala, Kaori Sugihara, Michael Gabi, Dominik Textor, Pascal Behr, Elsa Thomasson, Robert MacKenzie, Andreas Binkert, Rami Mhanna, Raphael Zahn, Victoria Delange, Alexander Larmagnac for all the time I was allowed to spend with you during this year.

In Graz I want to thank Dr. Marcel Scheideler to accept to be assessor and his uncomplicated support. Prof. Roland Würschum and Prof. Christian Magele I want to thank for accepting to be co-referee within such short notice. Prof. Zlatko Trajanoski I thank for his help during my exchange year at ETHZ. Astrid Brodtrager I thank for her great administrative support. For correcting my numerous mistakes in English, I want to especially thank not only the great proofreaders but also really good friends James Yeo, Ulrike Weiß, Mimo Saleh, Denise Mühlbacher and Brian and Theresa Bridges. During my studies I was lucky to get to know many friends, who are impossible to list here, so I only name those who more or less directly gave me feedback on this work. Thank you Johannes Peham, Mario Bellina, Robert Arnold, Albert Kemetinger, Sebastian Tschiatschek, Thomas Morocutti, Simone Kopeinig, Kajetan Hacker, Tobias Böhlen, Lars Aprin, Elisabeth Lindner, Ingrid Hauser and Manuel Kürzenberger.

For my family Waltraud, Günter and Claudia. Thank you for being in my wonderful life so far. Without my parents, neither me nor my work would be in this world…

Kurzfassung

Lokalisierte Oberflächen Plasmon Sensoren (LSPR) zeichnen sich durch ihre adaptierbare Größe der Partikel und eine annähernd gleich gute Sensitivität wie bereits kommerziell etablierte Oberflächen Plasmon Sensoren (SPR) aus.

Im Zuge dieser Arbeit wurde die Antwort des optischen Signals eines solchen LSPR-Systems auf elektrochemische Prozesse an der Oberfläche der Nanopartikel untersucht, um eine zukünftige Anwendung einer Kombination aus einem elektrochemischen Sensor mit einem LSPR-Sensor möglich zu machen. Durch die hohe lokale Sensitivität der LSPR-Sensoren konnten detailliertere Informationen über die elektrochemischen Prozesse an der Oberfläche gesammelt werden. Die Ergebnisse in der folgenden Arbeit sind in zwei Teile geteilt.

Im ersten Teil (Kapitel 4) wurde das Spektrum des LSPR-Sensor Systems bei elektrochemischen Vorgängen an der Oberfläche der Partikel untersucht. Dafür wurde, parallel zum optischen Spektrum der Gold-Nanopartikel, die Spannung zyklisch angelegt (cyclic voltammetry, CV) und aufgezeichnet. Die Nanopartikel wurden auf einem Glasträger mit einer Indium-tin-oxid(ITO)-Schicht gebunden. Das gemessene Spektrum der Partikel zeigte sowohl im kapazitiven Regime als auch bei chemischer Reaktion bei weiter erhöhtem Potential eine sensitive Antwort. Durch eine parallel durchgeführte numerische Simulation konnte das aufgenommene Spektrum durch die Ausbildung eines "lossy layer" erklärt werden. Dieser "lossy layer" besteht einerseits aus der Ionenschicht außerhalb des Partikels und andererseits aus einer Schicht mit abnehmender Elektronendichte in der äußersten Schicht des Gold Nanopartikels. Mit einem Potential über dem Oxidationspotential von Gold konnte im aufgezeichneten Spektrum eine Änderung der Oberfläche der Partikel beobachtet werden.

Im zweiten Teil der Arbeit (Kapitel 5) wurde untersucht, ob der LSPR-Effekt auch einen Einfluss auf die Reaktionsrate des chemischen Prozesses hat. Dazu wurden konstante Potentiale verschiedener Stärke an die Partikel angelegt und unter Bestrahlung mit Licht der resultierende Strom gemessen. Es wurde zwar eine Erhöhung der gemessenen Stromdichte aufgezeichnet, ein direkter Zusammenhang mit einem durch Plasmonen induzierten Effekt konnte allerdings nicht festgestellt werden, da die Stromdichte auch im Kontrollexperiment, durchgeführt an einer soliden Goldschicht, anstieg. Dieses Verhalten ließ sich durch eine Temperaturerhöhung an der Goldoberfläche erklären.

Abstract

Localized surface plasmon resonance (LSPR) biosensors are expected to play an important role in the next generation sensing method. The intrinsically small size of the plasmonic nanoparticles, the simple sensing mechanism and a detection limit in the range of commercially established surface plasmon resonance (SPR) biosensors make them well-suited to achieve high-throughput chip-size devices.

The scope of this work was to study the behavior of the optical response to electrochemical processes, to gain a basic understanding for future applications of a combined LSPR and electrochemical sensing system. The electric conductivity of the gold nanoparticles allows a directly applied voltage, initiating electrochemical processes. Due to the high local sensitivity of LSPR sensors, a more detailed information of processes in vicinity of the surface could be obtained.

The results in this work are divided into two parts. In the first part the response in the LSPR spectra to ongoing electrochemical processes in vicinity of the surface was investigated. Therefore a synchronized cyclic voltammetry (CV) and a localized surface plasmon resonance (LSPR) measurement on gold nanoparticles, immobilized on an indium tin oxide (ITO) substrate was conducted. The recorded LSPR showed to be sensitive to chemical surface reactions, as well as to the formation of electric double layers. Furthermore, a numerical simulation suggested a formation of a lossy layer by electron depletion and negative ion adsorption already in the capacitive charging regime. Above the oxidation potential, gold was found to be dissolved and during the reduction re-deposited, which led to a change in size and configuration of the gold nanoparticles.

In the second part a possible influence of the LSPR on electron transfer reactions was investigated. Different constant potentials were applied between the ITO substrate with immobilized gold nanoparticles and the reference electrode. The current over the counter electrode was continuously recorded. During the measurement a light source was switched on by a mechanical shutter, resulting in an increase of current. A direct relation between the increased current and the LSPR could not be observed, since the control experiment with a solid gold film showed similar response. The most proper explanation was given by a local temperature increase at the gold surface.

Contents

Nomenclature **IV**
Abbreviations IV
Notation IV
Operators and Functions V
Symbols V

1 Introduction **1**
1.1 Sensor and signal transduction 1
1.2 Biosensor 3
1.2.1 Optical transducer 4
1.2.2 Electrochemical transducer 6
1.2.3 State of the art optical biosensors 8
1.3 Scope of this work 9

2 Principle **10**
2.1 Plasmon Resonance 10
2.1.1 Electrical conduction in metals 10
2.1.2 Optical and electric properties of metals 10
2.1.3 Surface plasmon polaritons at plane interfaces 12
2.1.4 Localized Surface Plasmon Resonance (LSPR) 12
2.1.5 Localized Surface Plasmon Resonance Biosensing 14
2.2 Electrochemistry 16
2.2.1 Electrolyte 16
2.2.2 Electrified interfaces in solution 17
2.2.3 Kinetics 17

3 Method **21**
3.1 Flow Cell design 21
3.2 Preparation of samples 23
3.2.1 Attaching the gold colloids on the ITO substrate 23

3.2.2 Mounting the flow cell . . . 24
3.3 Preparation of solutions . . . 25
3.3.1 Buffer solution . . . 25
3.3.2 Gold colloid solution . . . 25
3.3.3 Polymer . . . 25
3.3.4 Electrolyte solution . . . 25
3.4 Measurement . . . 26
3.4.1 Spectroscopic Measurements . . . 26
3.4.2 Electrochemical detection Measurements . . . 27

4 Electric Double layer formation 28
4.1 Introduction . . . 28
4.2 Experimental setup . . . 29
4.2.1 Combined cyclic voltammetry and LSPR sensing . . . 29
4.2.2 Dynamics of the electric double layer forming at different concentrations upon potential jumps . . . 30
4.3 Results . . . 30
4.3.1 LSPR response by electrochemical stimuli . . . 30
4.3.2 Dynamics of the electric double layer forming at different concentrations . . . 35
4.4 Discussion . . . 37
4.4.1 An applied voltage of maximal 500 mV . . . 37
4.4.2 Kinetics and salt concentration . . . 41
4.4.3 An applied voltage of maximum 800 mV . . . 42
4.4.4 An applied voltage over 1000 mV . . . 43
4.5 Conclusion . . . 43

5 Enhancement of chemical reaction by LSPR 46
5.1 Introduction . . . 46
5.2 Experimental setup . . . 46
5.3 Results . . . 48
5.3.1 Bare ITO . . . 48
5.3.2 ITO covered with plasmonic nanoparticles . . . 49
5.3.3 ITO covered with plasmonic nanoparticles with Ferrocyanide solution 51
5.3.4 ITO covered with plasmonic nanoparticles with constant flow . . . 53
5.4 Discussion . . . 58
5.5 Conclusion . . . 60

6 Summary **61**
6.1 Electric Double Layer formation 61
6.2 Enhancement of chemical reaction by LSPR 62

Bibliography **63**

Appendices **72**

A Overview of the Mie Scattering **73**
A.1 Scattering 74

B Influence of diffusion layer on the LSPR shift **78**

Nomenclature

Abbreviations

CV	cyclic voltammetry
OCP	open circuit potential
$\mathrm{E}^{\ominus}$	standard state potential
EDL	electric double layer
OHP	outer Helmholtz plane
IHP	inner Helmholtz plane
redox	reduction-oxidation
UV	ultraviolet
IR	infrared
SPR	surface plasmon resonance
LSPR	localized surface plasmon resonance
SEM	scanning electron microscope
CCD	charged coupled device
ITO	Indium tin oxide
NaCl	Sodium chloride
DNA	deoxyribonucleic acid

Complex and Vector Notation

$\boldsymbol{E}$	vector (within Figures: $\vec{E}$)
$\boldsymbol{a}^T$	transposed of vector $\boldsymbol{a}$
$\underline{a}$	complex–valued variable
$\underline{a}^*$	conjugate complex of $\underline{a}$
j	imaginary unit

Operators and Functions

$\Im\{\ldots\}$	imaginary part
$\Re\{\ldots\}$	real part
$\nabla(\ldots)$	nabla operator
$\nabla^2(\ldots)$	Laplace operator
$\delta(\ldots)$	Dirac's delta function
$(\ldots)^*$	complex conjugation

Symbols

η	overpotential
c_0	speed of light in free space
ϵ_0	dielectric constant of free space
μ_0	permeability of free space
k	wave number in free space $k = \frac{\omega}{c_0} = \omega\sqrt{\mu_0\epsilon_0}$
$\boldsymbol{E}$	vector of electrical field strength
Φ	electrical potential
σ_{ext}	extinction cross section
n	refractive index
λ	wavelength
i	electric current
j	electric current density
$\hbar$	reduced Planck constant $\hbar = \frac{h}{2\pi}$
ω	angular frequency

Chapter 1

Introduction

1.1 Sensor and signal transduction

Even before we are able to understand the first sentence of this thesis, our body already begins to use sensor systems to process information. The cone and rod cells in our eyes are able to discriminate different wavelengths and different intensities of light. This physical information is converted into an electrochemical signal and transmitted to our brain, which makes it possible for us to enjoy a colorful sunset on the beach. Or, as another example, the different sensory nerves in our skin are able to recognize pressure, heat or cold and again transmit this information via an electric signal to our brain [1]. With these numerous examples evident in the human body, it was only a matter of time before scientists began to reproduce what nature demonstrates every day.

In a very general description a sensor receives a certain stimulus and converts it into a signal, which is easy to process. This stimulus can be of any change in a physical, chemical or biological parameter (temperature, pressure, concentration of molecules, identity of molecules *etc.*) depending on the task of the device where the sensor is implemented. For example, think of an air conditioning system in a car. First of all the system needs to sense the actual temperature in the car, so that the central processing unit is able to decide, if heating or cooling is necessary. Additionally, since all logic decisions and signal processing are mostly implemented by electric circuits, the temperature sensor should already react to the change in temperature with a corresponding electric signal. This conversion of energy can be done in many ways [2]. One way is to utilize the fact that the electrical resistance of various metals and semiconductors depends on temperature [2]. If the material is in direct contact with the object, heat transfer through thermal conduction will occur. Thus, if the temperature coefficients of the used material are known, a change in current flowing through the material can directly be related to a temperature change, using Ohm's law. Thermal energy is therefore directly converted into electric energy (direct sensor).

Another way relies on the fluorescence of a special phosphor compound under UV-light.

Although these sensors do not apply in an air conditioning system, they are a good example of sensors where the stimulus is not directly converted into an electric signal. Due to its consistency the phosphor compound can be painted directly over the measured surface. The fluorescence decay of the painting after the excitation is then related to its temperature [3]. Therefore the energy conversion in such fluoroptic-sensors can be separated into two steps. First the thermal energy is converted by the phosphor compound into optical energy. Elements, converting a form of energy into another are termed transducers. In the second step, the electromagnetic radiation (light) is converted into charge carrier (current) by a quantum detector (photodiodes, phototransistors, photoresistors). In figure 1.1 the basic principle of the described optical sensor is shown, together with the common terms used in literature.

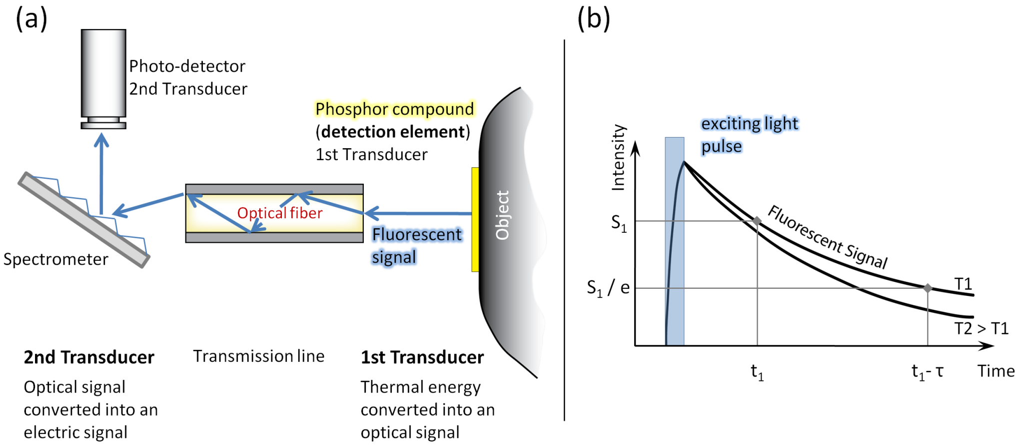

Figure 1.1: Schematic illustration of the described fluoroptic-sensor. The phosphor compound at the object surface is illuminated by UV-light and emits the fluorescent signal which is detected at the photo-detector (a). The decay of the fluorescent signal depends on the surface temperature as shown in (b). At higher temperature the fluorescent signal decreases faster. Adapted from [2].

Beside their already mentioned application in the Automotive Technology, today's sensors became essential in almost every field of technology [4]. The field of application has also a considerable influence on the design itself. Considering the two described ways of temperature sensing again, high electric fields in the vicinity of the measured object, for example, would disturb the electric signal. Thus, one would probably stick to the second way of conversion, since the conversion of the optical signal into an electric signal can be done at a certain distance from the object. Additionally, often different features of the sensors are important. Sometimes a certain dynamic of the heat transfer between the object and the sensor is required, or a certain sensitivity of the sensor is needed to be able to resolve slight changes in temperature (for further information on sensor characteristics like sensitivity or dynamic of the response see [2]). As a consequence, effects of the stimulus on the detection element need to be understood and often specific properties of materials turn out to be promising for sensor applications (*e.g.* the plasmonic resonance in nanoparticles, which will play an important role in this work). This is one of the reasons why sensor design is highly interdisciplinary today. In the following section a type of sensor is introduced which is a good example of such interdisciplinary research.

1.2 Biosensor

For an explanation of the idea of a biosensor let us return to the very beginning of this chapter. More in detail, the energy conversion and transmission of the electrochemical signal to our brain is a rather complex process reliant on many parameters [5], [1]. Small amounts of an injected anesthetic, for example, can lead to an interruption in the signal transmission and inhibit therefore the sense of pain. Thinking of this high sensitivity and accuracy (only certain chemicals can inhibit the process), the isolated responsible compound would give a good detection element for chemical compounds (analyte). This is the principle idea of a biosensor.

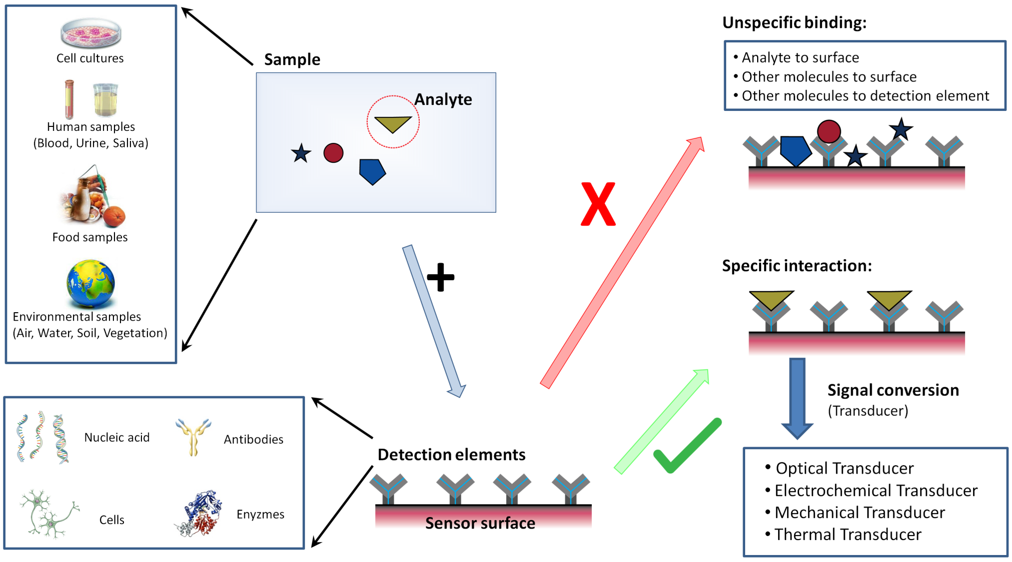

Figure 1.2: Principle of biosensors. The sample containing the analyte is brought into contact with the sensor. The detection elements, which are depending on the application, are attached to the sensor surface. Between the species in solution and the detection elements (later named recognition element) occurs either unspecific binding (other species than the analyte) or specific binding (analyte-detection element). The binding event leads to a change in specific parameters (mechanical, optical, thermal *etc.*) which is converted into a processable signal by the transducer.

Biosensors, per definition [6], are devices that use biochemical reactions mediated by enzymes, immunosystems, tissues, organelles or whole cells as a recognition element for chemical compounds (detection element; bioreceptor). Hence one can already imagine why biosensors are a highly interdisciplinary field today and often need a combined knowledge from different fields.

Biosensors can again be divided in the same parts already stressed in the section before. The main principle is sketched in figure 1.2. Biochemical reactions between the recognition element and the analyte (analyte-bioreceptor interaction) will lead to a change in a parameter, which can be monitored and converted into an electrical signal (transducer). To increase the sensitivity, additional filtering components are often used to lower the chance of unspecific interactions with the recognition element. Since the size of the recognition elements in biosensors is rather small, the change in a measurable parameter will often be in a small range and only detectable in a small vicinity of the recognition element, thus making it necessary to investigate new transduction systems.

The focus of this work will be on a combination of an optical and an electrochemical transduction system. Therefore only these two principles will be mentioned, whereas also other detection mechanisms exist (mechanical, thermal *etc.*). Furthermore, the surface functionalization for specific elements, which is essential for a high accuracy, is not part of this work either and the interested reader is therefore referred to certain literature such as Zourob *et al.* [7] or the review paper of Borisov *et al.* [8].

1.2.1 Optical transducer

One example of an optical transducer, although not in the field of biosensors, was already given in the introduction when the fluoroptic temperature sensor was described (section 1.1). The idea of energy conversion into light by a fluorescent element also plays an important role in biosensing. Here the analyte is coupled with a fluorophore. Hence, a binding event of the analyte can then be detected in analyzing the spectra for the specific wavelength emitted by the fluorophore [9]. Beside the fluorescence-based detection methods, label-free optical biosensing methods are used today. These methods allow a detection of the binding event of the analyte without additional processes. It is therefore possible to also study the kinetics of the binding process in contrast to detection methods, which require a second recognition element.

In general, label-free optical biosenors are always based on collecting light from an illuminated surface, measuring a change in different optical parameters (polarization or phase of the collected light, or its intensity) caused by the adsorption of molecules.

Surface plasmon resonance (SPR)

Surface plasmon resonance (SPR) biosensors utilize the dependence on the propagating surface plasmon polariton on the optical properties of the surface. The propagating surface plasmon can be excited in thin metal films at the interface to a dielectric by light illumination under certain conditions (see also section 2.1.3). Changes of the refractive index in vicinity of the sensor surface can be detected as a change in the resonant coupling angle [10], the resonant wavelength [11] or the resonant intensity [12], depending on the excitation method of the SPR (prism coupling, waveguide coupling, optical fiber coupling).

Ellipsometry

Ellipsometry analyses the polarization of the reflected, or more seldom of the transmitted light, by an adsorbed layer. The polarization change is related to the properties of the sample (thickness, complex refractive index) and can therefore be used to extract information about the optical properties [13]. Although high precision in the measured optical parameters can be obtained, the setup is usually large and therefore not that often used in commercially available biosensors.

Waveguide-based biosensors

The waveguide mode depends on the refractive index of the layers at the boundaries of the waveguide. This fact is used by waveguide-based sensors gaining information about the change of optical properties at the waveguide-solution interface. One example of an established waveguide based sensor would be the optical waveguide light-mode spectroscopy (OWLS) sensor [14], whereas there are several different designs [15].

Interferometry

Interference-based sensors split a light wave equally into two branches, one interacts with the sample while the reference branch is protected from outer influences. The two branches are interfered at the output, giving information about the optical properties of the surface layer. Although interference based sensors have often an excellent detection limit, the instrumentation is relatively large and therefore more suited for research purpose [16],[15].

Resonator

In ring resonators the input light has, in contrast to simple waveguide sensors, more opportunities to interact with the target molecule [17]. So called whispering gallery modes, or circulating waveguide modes, are developed due to the total internal reflection of light along the curved boundary of the ring and circulating in the resonator. Information about the surrounding refractive index is gained by the wavelength shift of the whispering gallery mode. However, the fabrication of ring resonators, such as precise shape and coupling of the light, is not yet ready for mass production.

Photonic crystal-based sensors

The dielectric structure in photonic crystals is designed in a way, such that a photonic band gap is formed, prohibiting wavelengths within the bandgap to propagate through the crystal. By introducing a defect in the crystal structure, the wavelength in resonance with the degenerated structure can pass through it. This photonic band is sensitive to the refractive index of the medium. The possibility of introducing defects in various directions allows the design of 3D photonic devices.

1.2.2 Electrochemical transducer

Most biological interaction processes are, as already mentioned, often combined with electrochemical reactions. During the interaction, electrochemical species are produced or consumed, leading to a change in the electrical properties of the complex. Electrochemical transducers use this fact to extract information about the ongoing processes by the measurement of electric properties. However, it is often challenging to find the right recognition element and connect it directly to an electronic device, so that the sensor provides to be specific and sensitive to the analyte [7]. The three electrodes named reference, counter or auxiliary and working electrode, are usually used for the measurement of the electric properties. The working electrode is in direct contact with the recognition element and therefore also often named sensing or redox (reduction-oxidation) electrode. In a three electrode setup, current is always applied between the counter and the working electrode. Hence both electrodes should be chemically almost inert and conductive [18]. The reference electrode serves as a reference point for an applied potential to the electrochemical cell and should therefore maintain a known and stable potential. This is also the reason why three electrode setups are preferred over two electrode setups. For the two electrode setup a current would also pass through the reference electrode making it difficult to maintain a constant value. Depending on the parameter under investigation, the following detection techniques can be differentiated.

Amperometric devices

Nowadays most of the available electrochemical sensors are amperometric sensors. Amperometric devices continuously measure the current response of the system under investigation at a known potential. An often cited example is the measurement of glucose by an enzyme electrode. The glucose oxidase enzyme (GOx) catalyzes the reaction of glucose and oxygen (glucose + $O_2 \xrightleftharpoons[\text{oxidase}]{\text{glucose}}$ gluconic acid + H_2O). Therefore measuring the concentration of O_2 will give a direct conclusion about the concentration of glucose in the solution. The concentration of oxygen can further be related to a measured current at an oxygen electrode (using the redox reaction $O_2 + 4H^+ + 4e^- \rightleftharpoons 2H_2O$ at an applied potential of $-0.6\,\mathrm{V}$ against Ag/AgCl). In contrast to sensors where a direct electron transfer occurs, these sensors work over an intermediate step (oxygen as mediator).

Cyclic Voltammetry (CV) as a special technique in the category of amperometric devices, is useful to obtain basic information about the analyte solutions such as redox potential and for the semiquantitative analysis of electrochemical reaction rates. In the case of CV, the voltage is cycled between two values at a fixed scan rate (V/s). The recorded current consists of a faradaic current, if the applied potential is in the relevant zone where electrode reaction occurs, and also of a capacitive contribution due to double layer charge. The typical peaks occurring in the voltammogram, when the current is plotted over the voltage, can be understood in the following way. When the applied potential is shifted from equilibrium towards a potential where the electrode reaction begins, the current rises. At a potential more positive than the equilibrium potential this will lead to a net anodic current (electron from the solution layer to the electrode) and vice versa at a more negative applied potential would result in a net cathodic current. However, consumption of electroactive species results in a decrease of current, since the supply of electroactive species begins to fall. Due to the creation of a concentration gradient, electroactive species diffuse from bulk towards the electrode. The current is then controlled by the diffusion. If the reaction is reversible, a similar peak will occur when the scan is reversed, but this time the current would flow in the opposite direction. The equilibrium potential of the reaction lies in between the oxidation and reduction peak. An increased scan rate leads to an increase of the charging current of the double layer and the reduction and oxidation peaks become more separated [18].

Potentiometric devices

Potentiometric devices record the voltage between the working electrode and the reference electrode in a range so that no significant current flows. The electrochemical cell is therefore at equilibrium and it is possible to conclude about the activity coefficients of the ions [19].

Conductometric devices

The electrical resistance of a medium is dependent on the concentration of charge carriers. Hence, a change in concentration of an electroactive substance can be related to the electric resistance. Conductometric devices are often used with enzymes, where the ionic strength and thus the conductivity changes as a result of enzymatic reaction [20]. Electrochemical impedance spectroscopy (EIS) is one example of a resistance measurement techniques.

The impedance of the cell or electrode is measured as a function of the frequency of an alternating current source (AC-source). Electrochemical impedance spectroscopy is often used for studies of double layer structure since information about the capacitance can also be gained [21].

1.2.3 State of the art optical biosensors

Today biosensors play an important role in manifold applications like in biomedical research, healthcare, drug research and environmental monitoring. The needs they have in common are high sensitivity and accuracy, as well as high throughput of samples. It is often the case, that only a few copies of the important marker analyte for diagnostics are present in a sample [22], [23]. Higher sensitivity can therefore lower the needed sample volume, which becomes important for many applications where the amount of starting material is often limited and very expensive (*e.g.* cancer tissue, stem cells), [24], [25]. Furthermore, for certain analytes (*e.g.* proteins) no amplification strategies, equivalent to the polymerase chain reaction (PCR) for deoxyribonucleic acid (DNA), are available so far. Beside a decrease in the required sample volume, a lowered detection limit of certain analytes could lead to direct improvement of the application. In homeland security, for example, detection of explosives at very low concentrations could lead to the information if the object was even only in contact with explosives. Or in medical diagnostics early recognition of pathological values of analytes could improve possible treatments. Medical diagnostics gives also a good example for the importance of high throughput of samples. Today proteins are understood to play an essential role in biological organisms and therefore also become more and more important in drug research [22], [26], [27]. Whereas DNA can only assume a few different structures and consists of four types of nucleotides, proteins are made of 20 kinds of standard amino acids with often complicated structures. To find important candidates of proteins in certain biological processes it is therefore often necessary to scan for many different proteins only manageable by high throughput of samples.

Today the majority of commercially available optical biosensors still use labels due to their high accuracy, although label-free biosensing is starting to play an important role [28]. In the field of labeled biosensing single molecule detection has become a keyword [9]. Optical biosensors with fluorescence readout have the power to achieve those high sensitivities.

One way to increase the detection limit relies on increasing the light hitting the detector, due to interference layers reflecting the light. Fluorescence signals normally absorbed by the substrate can hence still contribute to the detected signal [29], [30]. Another approach to improve the readout quality is done by a combination with evanescent wave-based techniques such as SPR. Due to the exponential decay of the field into the medium fluorescence excitation is only limited to the vicinity of the surface resulting in significant reduction of the background noise.

A second way to improve the detection limit, is done by improving the label itself. First to overcome drawbacks of organic dyes like bleaching or quenching effects, and second to be able to narrow the broad emission spectra of normal dyes. The products of nanotechnology started to play an important role in replacing the traditionally used fluorescent dyes [31].

1.3 Scope of this work

In contrast to other optical sensing methods the excitation of the plasmon-polariton at localized surface plasmon resonance (LSPR) biosensors can be readily triggered by simple plane wave illumination with light in the visible spectra (see also 2.1.4), which allows for simpler devices. Therefore LSPR sensors are expected to play an important role in future sensing devices. The intrinsically small size of the plasmonic nanoparticles, combined with the high local sensitivity comparable to todays SPR sensors, is well-suited for high-throughput sensing devices [32].

As a next step towards future application one could think of combining LSPR sensors with other transduction mechanisms in order to further improve the quantity of the determinable parameters or even overcome the inherent limitations of a single method. As already mentioned before, one of the main advantages of optical label-free biosensors, such as LSPR sensors, is their possibility to be able to study binding kinetics. In combination with an electrochemical system this would allow further information to be gained on ongoing processes at the surface when electrochemical reactions occur. In a long term view, this could be a promising technique studying the response of cell membranes, incorporated on substrates, to different drugs [33].

The scope of this work is to design and construct a LSPR sensor with an electrochemical sensing device and study the behavior of the LSPR response to basic electrochemical processes. To realize the simultaneous acquisition of optical and electrical information, a setup was designed consisting of a conductive substrate with attached gold plasmonic nanoparticles mounted in an electrochemical flow cell.

In the first part, the optical response of the system to the electrochemical reactions was characterized. Besides the chemical reactions at the electrode, whether the formation of the electric double layer could be resolved in the optical signal was also investigated.

In the second part, the influence of the LSPR to occurring surface reactions was investigated. It was tried to observe an increased current density at the sample under illumination compared to the sample measured in the dark. An observed increase in the current density was investigated further, to be attributed to a certain physical effect.

Chapter 2

Principle

The following section aims to give a basic understanding of the physics of the localized surface plasmon resonance as well as the electrochemical theory, needed for the measurements done in this work. The first part shows the special electrical and optical characteristics of metals causing the effect of plasmon resonance. Coming from the atomic structure in metals, allowing an almost free movement of valence electrons, the volume plasma frequency of metals will be introduced. Furthermore by confining the possible directions of plasma oscillations, the basic theory behind plasmon resonance sensors will be stressed.

The second part of this chapter will give a short overview of the processes occurring on charged surfaces in an ionic solution. Starting with a short introduction on ionic conduction some basic theories on the behavior of charged surfaces in electrolytic solutions will be mentioned. Finally this will lead to a short overview on electron transfer processes when the electrochemical cell is out of equilibrium due to an applied potential by an electrode.

2.1 Plasmon Resonance

2.1.1 Electrical conduction in metals

Different from an isolated atom with its discrete energy levels, the periodic structure of atomic nuclei in a crystal leads to energy bands at the outer orbitals. At low potential energies of the electrons, the influence of neighboring atoms increases and the orbitals overlap allowing tunneling of the electrons through the potential barrier. At even lower energy regions the energy bands become thicker and the wave function spreads over the whole crystal. This is the typical case in pure crystals of metal atoms.

2.1.2 Optical and electric properties of metals

Due to the dimensions of particles, in the range of a few nanometers, it is mostly sufficient to describe light in the visible wavelength (about 400 nm–700 nm) by adopting the electromagnetic wave picture. Thus classical field theory based on Maxwell's equation can be used to describe analytically the interaction of light with nanoparticles. Of course, when the size of the objects interacting with light is in the range of a few atoms (atomic radius of gold: about 135 pm), often a quantum description of the material properties becomes necessary and sometimes the use of simple boundary conditions becomes doubtful, as it will be mentioned later in this work. As mentioned in section 2.1.1, ionization energy of the valence electrons in metals is very low and they are quasi-free to move. Electromagnetic waves will therefore mostly interact with these quasi-free electrons. Similar to the characteristics of gas plasma, also for metals a material specific plasma frequency exists. Local change in electron density will result in an electric field, accelerating surrounding electrons. As a result this leads to a collective movement of electrons relative to the ionized atomic core. The positive charge of the ionized atomic core acts as restoring force and the electron density will fluctuate with a incompressible longitudinal wave at the volume plasma or Langmuir frequency through the matter [34].

$$\omega_p = \sqrt{\frac{ne^2}{m_e \epsilon_0}} \tag{2.1}$$

In equation 2.1 ω_p is the plasma frequency, e is the charge of the free electrons and m_e is the effective mass of the free electrons. The energy of such oscillation is quantized to $\hbar\omega_p$ and thus the energy quant was named plasmon, similar to photons resulting from the energy quantization of light. In the classical picture, the valence electrons are not bound to certain atoms (electron gas, electron sea). They move through the metal with their thermal velocity until they undergo a collision within their mean free path. Considering an external electric field, accelerating the electron, this leads to the Drude-Sommerfeld equation.

$$m_e \frac{\partial^2 \mathbf{r}}{\partial t^2} + m_e \Gamma \frac{\partial \mathbf{r}}{\partial t} = e\mathbf{E}_0 e^{\mathrm{j}\omega t}, \tag{2.2}$$

where e and m_e are the charge and the effective mass of the free electrons, $\mathbf{E}_0$ the amplitude and ω the frequency of the external electric field and $\mathbf{r}$ the displacement of the electron. The scattering of electrons is considered in this equation of motion by the damping term proportional to $\Gamma = \frac{v_F}{l}$, l being the mean free path between the scattering events and v_F the Fermi velocity. Or in other words $\Gamma = 1/\tau$, the collision frequency, τ known as the relaxation time of the free electron gas. After solving equation (2.2) and introducing the solution into the macroscopic material equation, the frequency dependent dielectric function for metals predicted by Drude and Sommerfeld reads as

$$\epsilon_{\mathrm{Drude}}(\omega) = 1 - \frac{\omega_p^2}{\omega^2 + \Gamma^2} + \mathrm{j}\frac{\Gamma \omega_p^2}{\omega(\omega^2 + \Gamma^2)}, \tag{2.3}$$

where ω_p is the volume plasma frequency. For gold, as an example, this gives an accurate prediction for the interaction with wavelengths above 650 nm. Although at lower frequencies the energy of the photon is already high enough to excite lower band electrons into the conduction band and the calculated values do not fit with the real metals especially in the visible spectra. Therefore often experimental values for the dielectric constants are fitted and used in simulations (see also chapter 4).

2.1.3 Surface plasmon polaritons at plane interfaces

Experiments on the bombardment of thin metallic films by high energy electrons, showed an energy loss of the fast electrons which was less than the volume plasma energy. This indicated the existence of lower energy surface collective oscillations due to the impact of the film boundaries [35]. Still assuming a non relativistic behavior, the fluctuation in the electron density at the surface of the metal will also result in a transversal magnetic wave, caused by the interface of two different electric media. This can be shown by solving Maxwell's equation for an electromagnetic wave propagating on a plane surface between a metal and a dielectric (see [36]). By inserting the boundary conditions, the relation between the surface plasmon frequency ω_{sp} and the volume plasmon frequency ω_p is given by

$$\omega_{sp} = \frac{\omega_p}{\sqrt{1+\epsilon_m}} \tag{2.4}$$

being ϵ_m the dielectric constant of the surrounding media. Again the energy of such oscillation is quantized to $\hbar\omega_{sp}$ and thus the energy quant was named surface plasmon [37]. The electron density oscillation is naturally coupled with an electromagnetic wave and thus termed surface plasmon polariton. Excitation of the surface plasmon polariton by light is only possible if both the energy and momentum conservation is fulfilled. Considering the dispersion relation of surface plasmon polaritons this can only be achieved when the wavevector component of the exciting light matches the free-space value. This is done with different experimental approaches (prism coupling, waveguide coupling, optical fiber coupling) [15].

2.1.4 Localized Surface Plasmon Resonance (LSPR)

Considering now a metallic particle of the size smaller than the wavelength of the incident light, the electric field of light would cause a displacement in the charge distribution (figure 2.1). This will again lead to a collective oscillation of the valence electrons but this time confined in all directions and it is therefore termed LSPR. LSPR can be excited by light in the visible range in contrast to bulk metals. As a result metal nanoparticles have different absorption bands than bulk metals and express different colors (*e.g.* metal colloid solution shines red).

As already mentioned, Maxwell's wave picture is usually sufficient to describe the excitation of the plasmon polariton. A solution of the Maxwell equations for the case of spherical particles was given by Mie in 1908 and simplified later by Born [38] and Stratton [39].

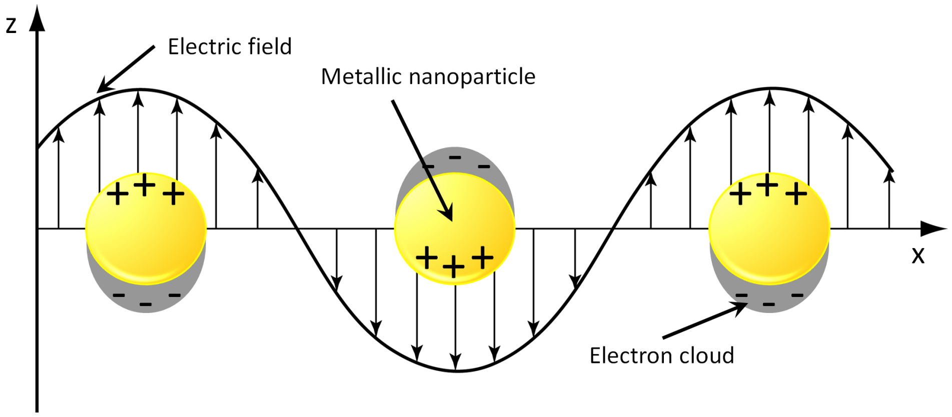

Figure 2.1: Schematic illustration of a metal nanoparticle in an electromagnetic field at the quasi-static case. The electric field causes a displacement of the electron density. Coulomb attraction towards the positively charged ion cores results in an dipole oscillation.

After the electromagnetic problem is solved the material properties are introduced by the dielectric functions. The consistence between the calculation and the experiment is therefore often dependent on the accuracy of the dielectric function.
For a more intuitive explanation of the LSPR, phase retardation due to the finite size and the effect of higher multipoles are neglected in the ongoing discussion (for a description of higher order oscillations see also appendix A). Since the considered metallic particle is sufficiently small compared to the wavelength of the incident light ($\frac{R}{\lambda} \leq 0.01$), the field can be approximated as constant at a certain time (quasi-static regime). In the quasi-static regime the electric potential and the electric field are related as $\boldsymbol{E} = -\nabla\Phi$. Since in free space $\nabla \cdot \boldsymbol{E} = 0$ the potential has to satisfy the Laplace equation $\nabla^2\Phi = 0$. The resulting field can then be found with the boundary conditions between the two media [40]. Inside ($\boldsymbol{E}_1$) and outside field ($\boldsymbol{E_2}$) in spherical coordinates are given by

$$\boldsymbol{E}_1 = E_0 \frac{3\epsilon_m}{\epsilon_i(\omega) + 2\epsilon_m}(\cos(\theta)\boldsymbol{n}_r - \sin(\theta)\boldsymbol{n}_\theta) \tag{2.5}$$

$$\boldsymbol{E}_2 = E_0(\cos(\theta)\boldsymbol{n}_r - \sin(\theta)\boldsymbol{n}_\theta) + \frac{\epsilon_i(\omega) - \epsilon_m}{\epsilon_i(\omega) + 2\epsilon_m}\frac{a^3}{r^3}E_0(2\cos(\theta)\boldsymbol{n}_r + \sin(\theta)\boldsymbol{n}_\theta) \tag{2.6}$$

being $\epsilon_i(\omega) = \epsilon_1(\omega) + \mathrm{j}\epsilon_2(\omega)$ the dielectric constant of the metallic particle and ϵ_m the dielectric constant of the surrounding media. The dielectric constant of the media is assumed to be constant and real, which is normally sufficient over the visible spectra. In figure 2.1 a schematic illustration of the quasi-static case is shown at a certain time. The extinction cross section as the sum of the absorption and scattering cross section can furthermore be derived as

$$\sigma_{ext} = 9\frac{\omega}{c}\epsilon_m^{3/2}V_0\frac{\epsilon_2(\omega)}{[\epsilon_1(\omega) + 2\epsilon_m]^2 + \epsilon_2(\omega)^2} \tag{2.7}$$

$V_0 = \frac{4\pi}{3} R^3$ denotes the particle volume, ϵ_m being the dielectric function of the embedding medium and $\epsilon(\omega)$ the dielectric function of the particle material being ϵ_1 the real and ϵ_2 the imaginary part.

Resonance condition

Resonance of the internal field in equation 2.6(quasi-static regime) occurs when $|\epsilon_1 + 2\epsilon_m| = \min$. Usually the surrounding dielectric constant is taken as real and independent of frequency over the visible spectra and therefore

$$[\epsilon_1(\omega) + 2\epsilon_m]^2 + [\epsilon_2(\omega)]^2 = \min \tag{2.8}$$

From 2.8 it can be seen that a negative ϵ_1 is necessary to fulfill the resonance condition, which guarantees the proper phase relation between the field and the polarization of the metal plasmonic particle. Furthermore with the assumption of small $\epsilon_2(\omega)(\epsilon_2 \ll 1)$, *i.e.* small damping, or a small frequency dependence of $\frac{\partial \epsilon_2}{\partial \omega}$ the resonance condition can be written as

$$\epsilon_1 = -2\epsilon_m \tag{2.9}$$

This relation intuitively shows the dependence of the resonance on the LSP supporting material. Only a few metals exhibit the requirement of small damping (*i.e.* $\ll \epsilon_2$) and quasi-free conduction electrons at frequencies close to the surface plasmon resonance. Mostly gold and silver particles are used in biosensor applications, thus they are chemically nearly inert.

In figure 2.2 the dielectric constants of gold and silver are shown. The region, where the resonance condition is fulfilled for the most common surrounding media (dielectric constant of air $\epsilon_m = 1$; water about $\epsilon_m = 1.77$ in the visible frequency range; glass about $\epsilon_m = 2.25$), is highlighted. In vicinity of the resonance frequency the imaginary part of gold shows a steep increase due to the possible interband transitions.
In the end it should be mentioned again, that the resonance conditions presented here are only valid in the quasi-static regime. For particles bigger than the skin depth d of the metal ($d = \frac{\lambda}{(4\pi\sqrt{\epsilon})}$), higher order resonances come into play [42].

2.1.5 Localized Surface Plasmon Resonance Biosensing

The dependence of the surface plasmon resonance frequency on the surrounding media, or more precisely on its dielectric constant, is an interesting fact for sensor applications. Since $n = \sqrt{\epsilon_2}$, n being the refractive index of the medium and ϵ its dielectric constant, any change in the refractive index of the surrounding medium of the plasmonic particle should cause a shift in the resonance frequency (see equation (2.9)). A simplified describtion of

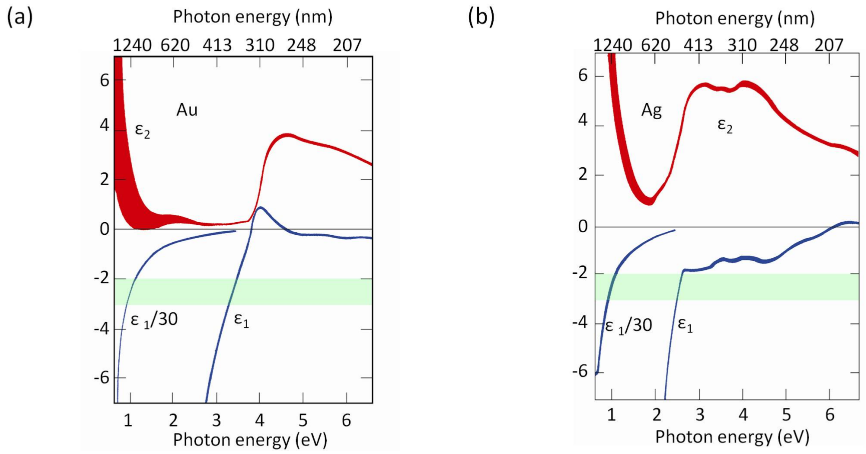

Figure 2.2: Dielectric functions of gold (a) and silver (b) as a function of photon energy. The real part of the dielectric constant is termed with ϵ_1 (blue curve) and the imaginary part with ϵ_2 (red curve) respectively. The width of the curves is representative of the instrumental error [41]. The region where the resonance condition is fulfilled for the most common surrounding media is highlighted in green. Thus one can see that the localized surface plasmon can be excited at visible wavelengths.

the LSPR peak shift response was given by [43]. The wavelength shift in the resonance frequency can be written as

$$\Delta\lambda_{\text{max}} = m(n_{\text{final}} - n_{\text{initial}}) \tag{2.10}$$

Here m tells about the sensitivity of the nanoparticle to a change in refractive index in nm/RIU (RIU: refractive index unit). The sensitivity m is characterized by the material properties and the shape of the particles [44],[45]. In equation 2.10 the wavelength shift was assumed to be linear which is normally sufficient when the change of refractive index is relatively small [46]. When the electric field is assumed to decay exponentially, the weighted sensitivity of the peak shift response can be written as

$$\Delta\lambda_{\text{max}} = m\Delta n(1 - \mathrm{e}^{\frac{-2d}{l_d}}), \tag{2.11}$$

m being the bulk refractive-index response of the nanoparticle(s); Δn is the change in refractive index, such as a molecule with higher refractive index adsorbing at the surface; d is the effective adsorbate layer thickness; and l_d is the characteristic electromagnetic-field-decay length (approximated as an exponential decay). Although the sensitivity to changes in the bulk refractive index m is much higher for SPR sensors than for LSPR sensors [47], the response of the two techniques becomes comparable when measuring short-range changes. This is a result of the much shorter decay length l_d of LSPR sensors (~5 nm–6 nm) compared to SPR sensors (~200 nm)[48].

The measurement of the LSPR spectra is commonly recorded by transmission ultraviolet-visible spectroscopy. By recording the wavelength dependence of the light passing through the sample, one gains the extinction spectrum (absorption plus scattering at the nanoparticles). The measured light intensity can then be related to the exctinction constant of the particles via the Beer-Lambert law:

$$I = I_0 \mathrm{e}^{-\gamma_e z}, \tag{2.12}$$

where γ_e is the extinction constant, I_0 the incident intensity, z the thickness of the sample and I the measured intensity at the detector. The extinction constant is connected to the extinction cross section by $N\sigma_{ext} = \gamma_e$, where N is the number of particles.

2.2 Electrochemistry

2.2.1 Electrolyte

Unlike the electronic conduction of metals and certain other substances (2.1.1), the physical charge carriers in electrolytes are ions (conductors of the second kind). Although also ionic conductors exist[49], in this work only electrolyte solutions were used. There are two ways in which electrolyte solutions become ionically conducting. The first one is chemical reactions of electrically neutral molecules. The second one is due to the dissolution of a solid lattice of ions in a solvent. The water molecules collide with the wall of the crystal enticing the ions out of the lattice. Due to the higher dielectric constant of water, the electrostatic free energy of the ion will be lowered and therefore this state is energetically favored. The electrostatic free energy in the solution is referred to as Born energy or solvation energy [50]. A rough approximation of the solvation energy can be achieved by the Born equation and is therefore often used for comparison of the solvation effects of various solvents.

Furthermore, the dissolved ion will influence the structure of the surrounding solvent. Depending on the charge and size of the solute the ion-dipole interaction with the solvent will vary. The solvation number, or in the special case of water the hydration number, is the number of the bounded molecules to the ion. Solvation gives rise to larger effective radii of the ions and thus influences their mobilities [51].

In this context the Debye-Hückel model should be mentioned, since the Debye screening length is still often used as an approximation in later theories. Within this theory, the interaction of the surrounding molecules and ions with a reference ion is simplified. The remaining ions beside the test charge are modeled as a continuous spatial distribution of charge ρ (excess charge per unit volume) and the water dipoles are replaced by the bulk dielectric constant.

2.2.2 Electrified interfaces in solution

If a charged metal electrode is brought into the electrolytic solution, the ions in its vicinity will be effected by the electric force caused by the surface charge of the metal and vice versa. Far from the interface, towards the electrolyte, the influence will decay and it can be treated as bulk. Again the decay length will depend on the composition of the electrolyte. Towards the bulk metal the charge is confined to a thin layer at the surface since charge separation inside the metal is very thin because of the high charge density.
The region close to the interface, where a reorganization of the electrolyte will occur, is termed electric double layer (EDL).

Electric double Layer

Several approaches have been made in a theoretical description of the EDL. Similar to the model of Debye and Hückel for ion-ion interaction, Gouy and Chapman solved the Poisson equation with a Boltzmann distribution of the ionic concentration. Later Stern proposed to combine the model of Helmholtz-Perrin with the one of Gouy-Chapmann to overcome the error at high concentrations (the Gouy-Chapmann theory is only applicable for potentials $<100\,\mathrm{mV}$). Figure 2.3 schematically illustrates the electric double layer with the used terms in the theories.

At the end of the 19th century Derjaguin, Landau, Verwey, and Overbeek then refined the interaction with surrounding particles resulting in the DLVO theory [52]. Lately Golovnev *et al.* published an analytic solution of the Poisson-Nernst-Plank equation (PNP-equation) [53] and several approaches are made to gain better agreements with experiments [54],[55].

2.2.3 Kinetics

Considering an electrochemical cell with two metal electrodes, the surface potential of the two metals will be different leading to two different electric double layers. Therefore, an electric potential will be measurable between the two electrodes dependent on the phase boundary at each electrode. The potential where no net current is measurable (the cell is in equilibrium) is termed open circuit potential (OCP).

In Figure 2.4 some of the steps that might occur when the interface potential at the electrode is changed are shown. At first accumulation of the species in the surface region will occur resulting in a charging current (non-Faradaic process). With increasing potential certain species can break out their solvation shell and enter the inner Helmholtz layer (IHL) and adsorb on the surface. When a certain potential is reached, chemical reaction, either preceding or following electron transfer, will occur.

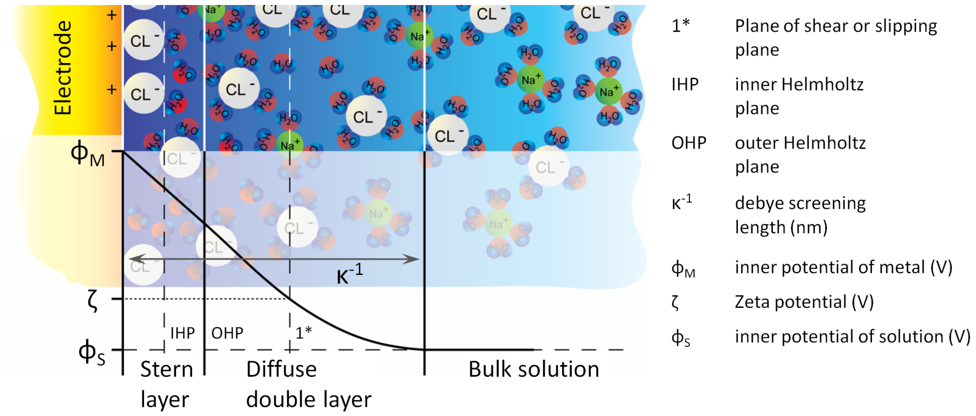

Figure 2.3: Schematic illustration of the electric double layer formed at close vicinity of the gold particle with the potential distribution into solution according to the Stern model. Additionally common terms from other models are shown. Negative ions are attracted by the positively charged electrode surface. The solvated ions arrange themselves along the surface of the electrode but are held away from it by their hydration shell. The sheet running through those hydrated ions is termed outer Helmholtz plane (OHP). Ions which have discarded their hydration shell are directly attached to the electrode by chemical bonds. This layer is termed inner Helmholtz plane (IHP). Ions inside the IHP and the OHP built the Stern Layer. Into the solution the potential decreased since it is shielded by the ions and over the diffusive double layer the interface merges into bulk. The Debye length is the length where the potential decreased to the inner potential of solution. The plane of shear is defined as the sheet of ions which stay at the surface when a shear force is applied, where so-called zeta potential (ζ) is measured.

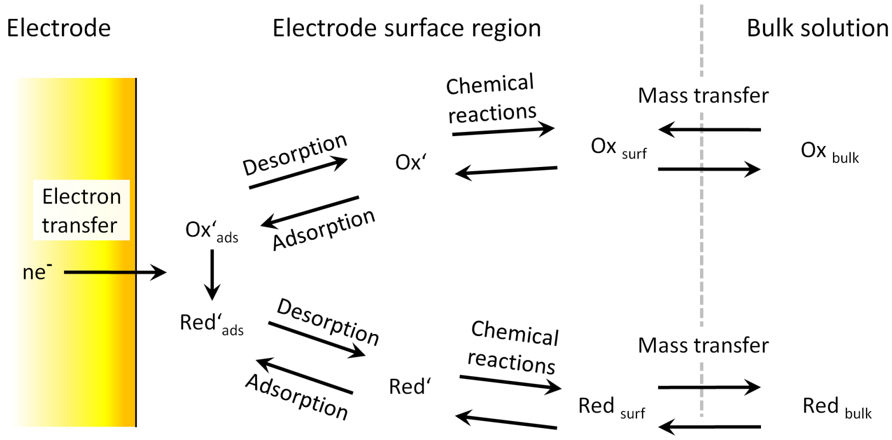

Figure 2.4: Schematic illustration of the surface region when electron transfer occurs. Due to surface reaction the concentration of either oxidized or reduced species in the surface region changes. Species will diffuse to the surface region from the bulk or away from the surface region into the bulk (mass transfer). The electric field at the surface region can furthermore lead to a change in the potential energy of the species possibly leading to chemical reactions with other species. After discarding the solvating molecules adsorption occurs and when reaching the excess potential electron transfer will occur. After the electron transfer the reduced or oxidized species will possibly desorb and diffuse away from the electrode surface. Adapted from [56].

Butler and Volmer introduced an equation for a thermodynamic description of electron transfer processes [57]. When the applied potential at the electrochemical cell is different to the standard potential of the redox-reaction a net current flow will occur, since the potential shift leads either to an increased reduction or oxidation process at the electrode. The current density $j = j_{\mathrm{anodic}} - j_{\mathrm{cathodic}}$ is according to Butler and Volmer:

$$j = j_0 \left(\exp^{\frac{(1-\alpha)\eta F}{RT}} - \exp^{\frac{-\alpha\eta F}{RT}} \right) \tag{2.13}$$

Here j_0 is called the exchange current density, F the Farraday constant, R the gas constant, T the temperature, α the transfer coefficient and η the overpotential. The transfer coefficient α (or for single step reactions β) depends on the shape of the potential-energy-distance curves of the reactant and the product of the species and can range from zero to unity [57]. The overpotential can also be written as the difference of the applied potential E to the equilibrium potential E_{eq} of the cell $\eta = E - E_{eq}$. The exchange current density occurs when the cell is balanced (equilibrium potential) and no net current j can be measured. Therefore the anodic current density j_{anodic} and j_{cathodic} must be equal and are set to j_0.

In a more detailed view, the electron transfer rates must be described at the atomic level (electrons are transfered by tunneling through a potential energy barrier) as done in a classical view by Marcus (1956) or later in a quantum mechanical view by Dogonadze and Levich (1959-1961)(see also [58], [57], [59]).

Chapter 3

Method

3.1 Flow Cell design

The first part of this work was to design and build a flow cell for the experiments (volume of 0.317 ml, dimensions of the flow area (L x W x T): 18 mm x 14 mm x 1.5 mm at the axis). To also be able to measure under dark field illumination, the flow cell was required to have a limited height and its transparent part should collect most possible light intensity. From the numerical aperture of the dark field condenser (NA = 0.95), the angle of the incoming light was calculated by the relation $\mathrm{NA} = n \cdot \sin(\alpha)$; n being the refractive index of the medium, α being the half-angle of the maximum cone of light that can enter or exit the lens. Considering the refraction at the interfaces the size of the opening was calculated. The height of the flow cell was required to be small enough to allow an almost laminar flow but needed to be of a certain height to provide enough space for the reference and counter electrode. Optimization of the inlet and outlet part was done by a numerical field flow simulation (ANSYS, Ansys Inc.). In figure 3.1a, it can be seen that the flow cell was symmetric with respect to its middle axis. Therefore, for lowering the calculation time only half of the mesh was calculated. The result of the flow simulation together with the used parameters is shown in figure 3.1c and figure 3.1d.

The upper part was manufactured with polymethylmetacrylate (PMMA), the transparent cover was a 45 mm x 45 mm x 0.25 mm glass slide. The reference electrode was a silver wire which was glued with a multi-part adhesive (epoxy resin) and the counter electrode was made of platinum and also glued with epoxy resin. The silver wire was chloridized before use to reach a semi-stable reference.

The lower part which was used to fix the sample on the flow cell was made of aluminum to reach proper mechanical stability. The sample was later isolated by a thin polytetrafluoroethylene (PTFE, Teflon) strips to avoid an electrical connection between the sample and the holder. This would lead to high electric capacitance connected over ground. A second smaller flow cell was built and used for the glass slide covered with gold in chapter 5. The

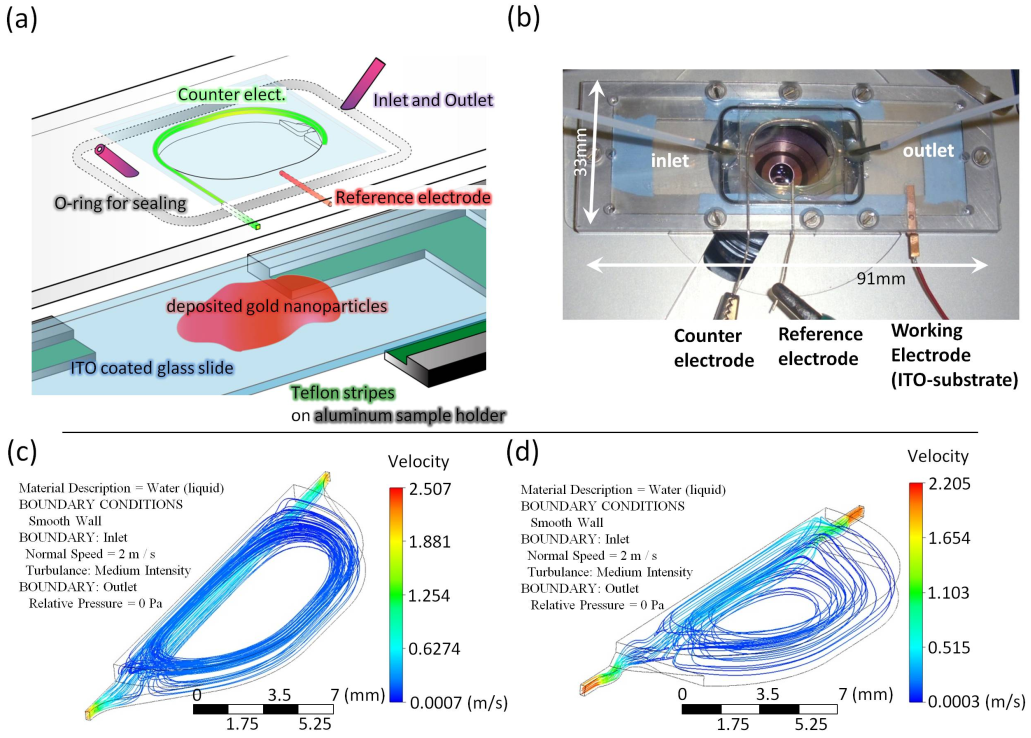

Figure 3.1: The design of the used flow cell during this work. (a) Magnified view of the flow region. The ITO slide is mounted on the sample holder and the top part is fixed with screws at the holder part. Teflon strips where used to isolate the substrate from the aluminum part. (b) Photo of the mounted flow cell under the microscope. Note the typical red reflection of the nanoparticles of this size. The electrodes where connected to the potentiostat, which is not shown in the picture. (c-d) Results of the numerical flow simulations of different geometries of the flow area. The design of (d) was chosen for production. For a demonstrative picture of the flow a particle stream was introduced. The particle tracks are shown as lines in the picture.

flow cell was made of PDMS (polydimethlysiloxane) covered with a glass slide and also adapted with a platinum counter-electrode and a silver wire as reference electrode. The volume of the flow cell was roughly 90 µl (cylindrical shape with a diameter of 2.4 mm). For the measurements the flow cell was pressed against the sample and fixed, resulting in a sealed chamber. The flow cell could then be filled over two Teflon tubes. After the measurement the sample was removed and the flow cell could be reused after the cleaning procedure (3.2.2).

3.2 Preparation of samples

3.2.1 Attaching the gold colloids on the ITO substrate

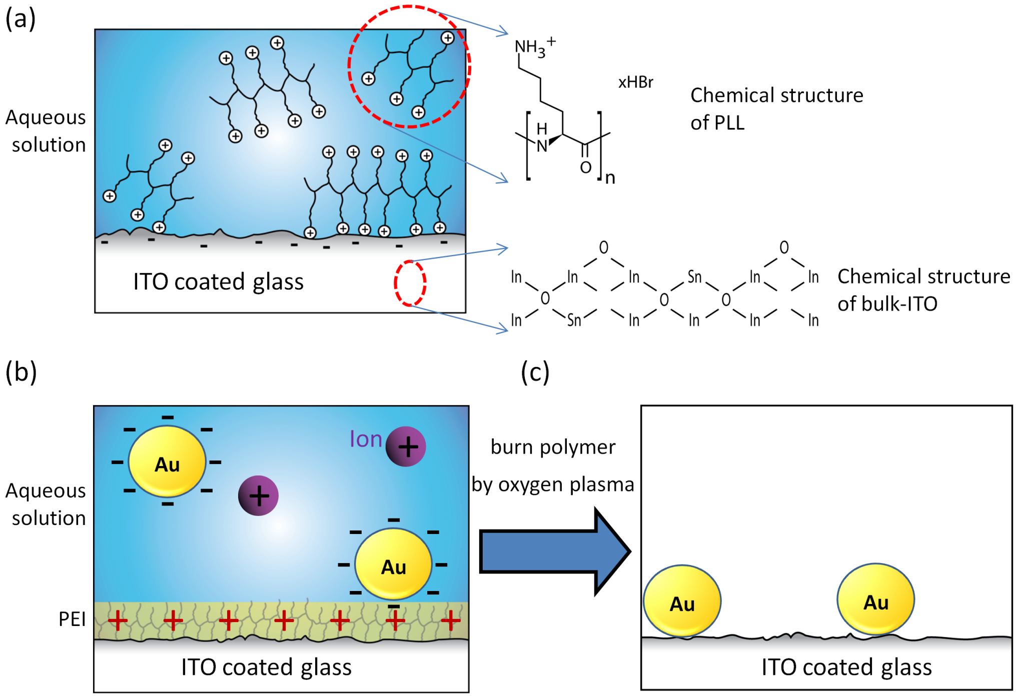

Figure 3.2: Different steps conducted to immobilize the gold nanoparticles onto the ITO surface. (a) First the deposition area was covered by a polymer solution. The positively charged polymer attached to ITO which is negatively charged in water (isoelectric point of pH ∼6) [60], [61]. The inset in (a) shows the chemical structure of ITO [62] and PLL respectively. After the sample is rinsed with ultrapure water the ITO slide was covered with aqueous gold solution (b). The surface potential of gold nanoparticles is negative in aqueous solution ([63]) and they stick to PLL. After the polymer was burned by oxygen plasma, Van-der-Waals binding is expected (c).

Indium tin oxide (ITO) coated glass slides were used as a base layer. The substrate (Univ. Neuchatel, Switzerland) was coated with a Polyethyleneimine (PEI; 1 mg/ml) layer or the second batch of ITO samples (Microvacuum, Hungary) with a Poly-L-lysine (PLL;

1 mg/ml) layer for electrostatic binding of the gold colloid nanoparticles. Onto this layer 50 nm gold colloid nanoparticles (British Biocell) were immobilized due to the electrostatic binding with the Polymer. The separate steps are shown in figure 3.2. The size of the substrate varied depending of the flow cell used in the experiments.

In detail the ITO substrate was first sonicated for 1 min in ethanol to remove possible contamination (*e.g.* oil film from the cutting process). After rinsing with ultrapure water (MilliQ, Millipore Corporation) the substrate was dried under a stream of high purity N_2. In the next step the substrate was cleaned for 1min in O_2 plasma (Harrick Plasma, US) at high power (18 W) and covered with PLL(1 mg/ml) dissolved in HEPES2 (see 3.3). To inhibit PLL solution from fast drying and crystallization, the sample was covered to avoid air flow. The sample was rinsed again with ultrapure water after a time of 30 min. Next the volume density of commercially available gold colloid solution was raised and the colloids were immobilized onto the PLL layer. Higher volume density of the colloid solution was reached by centrifuging it for 90 s to concentrate the gold colloids at the bottom of the centrifuging tube. The supernatant was removed afterwards by sucking it up with a syringe. With this process the concentration was increased by approximately 8 times, which led to a smaller interparticle distance at the final sample. Again, covering up of the sample was required to avoid it drying during the annealing time of 45 min. Afterwards the sample was rinsed again with ultrapure water to remove the unattached particles.

In the last step the sample was plasma cleaned for 1min in O_2 plasma under low pressure. The energetic plasma is expected to remove the PLL layer and the gold colloids are binding directly on the ITO substrate after the plasma cleaning. The binding was strong enough that the colloids could only be removed after wiping them away from the surface. During the project, the thickness of the indium tin oxide (ITO) layer on the glass slide changed since the substrates were produced by two different companies. The higher resistance of the second generation of substrates lead to a less homogeneous distribution of the gold nanoparticles when PEI was used for electrostatic binding on the ITO surface. After adapting the process and using PLL instead no difference between the two samples was measurable. The higher resistance of the ITO substrate increases the ohmic resistance in the electrochemical cell. Compared to the high resistance of the solid-liquid interface resistance, this influence is rather negligible.

3.2.2 Mounting the flow cell

The sample and the holder were first cleaned with water and dried with nitrogen gas immediately. This step removed unwanted particles such as dust from the surface of the materials. The holder can also be cleaned by ethyl alcohol and dried with N_2 afterwards. After cleaning both, sample and holder with water, they were treated in a plasma cleaner. The holder was cleaned with air plasma for 30 s and the sample was cleaned with pure O_2 plasma for a duration of 1 min. A solution was injected via the inlet with a syringe into the flow cell and was kept for at least 30 min to reach a stable state of the electrochemical system. The solutions used in the experiments were prepared on stock and kept at room temperature.

3.3 Preparation of solutions

3.3.1 Buffer solution

4(2-hydroxyethyl)piperazine-1-ethanesulfonic acid (HEPES) was obtained from Fluka Chemie (Switzerland). The HEPES2 buffer was prepared at a concentration of 10 mM. The pH was adjusted to 7.4 with 6 M NaOH and 150 mM NaCl was added additionally to the solution. Before use, the buffer solution was filtered (0.2 µm).
Ultrapure water (Milli-Q Gradient, A 10 system, resistance of 18 MΩ/cm, total 4ppb, Millipore Corporation, Switzerland) was used for preparation of the solutions unless specially noted.

3.3.2 Gold colloid solution

50 nm (4.5×10^{10} colloids/ml) gold colloids were purchased from British Biocell (UK) and stored in the fridge. The concentration was adjusted by centrifugation.

3.3.3 Polymer

Poly-L-lysine hydrobromide (PLL, Mw ∼15–30 kDa) and Polyethyleneimine (PEI, Mw ∼10–25 kDa) were obtained from Sigma Aldrich (Switzerland) and used at a concentration of 0.1 mg/ml in buffer solution.

3.3.4 Electrolyte solution

Sodium chloride

Sodium chloride solution was prepared from ultrapure water (MilliQ, Millipore Corporation) at a concentration of 100 mM unless specially noted.(4.3.2)

Sodium sulfate

Sodium sulfate (Na_2SO_4) solution was prepared from ultrapure water (MilliQ, Millipore Corporation) at a concentration of 100 mM.

Ferrocyanide

Potassium hexacyanoferrate(II)trihydrate ($C_6FeK_4N_6 \cdot 3H_2O$, Mw 422.39 Da) was obtained from Sigma Aldrich (Switzerland) prepared from ultrapure water (MilliQ, Millipore Corporation) at a concentration of 1 mM. Additionally 100 mM Na_2SO_4 was added to the solution.

3.4 Measurement

3.4.1 Spectroscopic Measurements

All spectra shown in this work are extinction spectra, recording the wavelength dependence of the absorption maximum of gold plasmonic particles. Spectra were recorded by an Ocean Optics spectrometer (USB2000, USA) and SpectraPro 2150 (PIXIS 400, Princeton Instruments, USA) using halogen lamp illumination and simple fiber optic readout. Generally the steps acquiring the LSPR spectra were similar in both systems (USB2000, PIXIS 400), they only differ in the handling and some features shortly noted in the following description of the basic routine.

At the very beginning information about the noise of the CCD-chip, which is mainly caused due to temperature, was acquired. Therefore the camera device needed to be turned on in advance to stabilize the chip. In both spectrometric systems the background noise was recorded over the whole exposure time, set in the software interface, times the number of averaged spectra. The noise was subtracted from the recorded spectra later automatically by the software.

In order to measure extinction of the LSP gold nanoparticles, a reference spectra of illumination light not interacting with the nanoparticles needed to be taken. Preferably this was done at a spot of the ITO substrate with no gold particles attached to. If this was not possible, the reference spectra would be taken without the sample mounted on the stage. Duration of the recording time of the reference spectra was again given by the later used exposure time and the number of averaged spectra. Final extinction spectra was obtained, by dividing the recorded spectra by the reference. Again this step was automatically done by the software. To record the extinction spectra of the plasmonic gold nanoparticles the sample was placed under the microscope, such that the desired sample area was observed and illuminated by a halogen lamp. All samples were illuminated with bright field, but unless otherwise noted, an IR-filter was used. Intensity was recorded with a CCD-chip, converted into digital values and transfered to the connected computer where the data was also stored for the offline processing. A relation between intensity and extinction is given by equation 2.12. Digitalization of the intensity was implemented in the software of each system differently. The SpectraPro 2150 system comes in a package with the commercial software WinSpec (Winspec32, Roper Scientific, USA). The USB2000 spectrometer was controlled by a custom made LabVIEW (National Instruments Corporation, USA) program. Intensity values were therefore normalized to the start value (subtracting the start value) to be able to compare the intensity change during the measurement between the two used systems directly. Since the SpectraPro 2150 system is attached to a microscope, the light can be focused in one spot and a small adjustable slit with a shutter is integrated into the light path. Therefore the spectra recorded with this system also included spatial resolution of the spectra in the y-direction (height of the slit). On the other hand the OceanOptics system is a fixed system without the ability of focusing the light. The incidence light is coupled into fiber optics and therefore the information on the spectra is limited to one point.

Analysis of the stored spectra

The stored data was evaluated with a stand-alone software (Fit1) which has been developed in Visual Basic (Microsoft, USA) [64]. With the program the digitalized intensity values could be reopened and processed with the help of the provided fitting and evaluation methods. For the finding of the extinction peak the implemented parabolic fitting algorithm was used ($f(x) = a(x-b)^2 + c$). The fitting is done in two steps. First a rough estimate of the function is done in a search range. Afterwards the second fitting process is conducted around the center of the function, $x = b$, within the entered fitting range. The second iteration process is stopped after the value converged to desired digits. Peak height corresponds to the coefficient c and the curvature can be evaluated as $\frac{1}{2}a$.

3.4.2 Electrochemical detection Measurements

After the system was stabilized and an almost constant open circuit potential (OCP) could be measured, cyclic voltammetry was conducted using a IPS Jaissle PGU10V-1A-IMP-S potentiostat (Jaissle Elektronik GmbH, Germany). All experiments were performed at a scan speed of 10 mV/s and in a three electrode setup except it is mentioned differently in the text.

Chapter 4

Electric Double layer formation

4.1 Introduction

In the following chapter the results are presented, which were obtained by conducting a synchronized cyclic voltammetry (CV) and a localized surface plasmon resonance (LSPR) spectroscopy using the already presented flow cell. The connection of the gold nanoparticles with the electric conductive indium tin oxide (ITO) makes it possible to apply also an electric potential to the gold particles. Due to the positive applied potential during the CV, a formation of ions is expected at the surface of the gold nanoparticles. As already mentioned in section 2.1.5, a change in the refractive index in close vicinity of the plasmonic nanoparticles would cause a shift in the resonance frequency. Indeed a sensitivity of the optical signal to electrochemical processes at the surface could be shown in studies of combined conventional surface plasmon resonance (SPR) with CV [65], [66]. Recently a combination of LSPR sensors with an electrochemical system was also shown in some works [67], [68], [69], [70], although an in situ combination of the LSPR sensor with CV has not been reported. Besides the observation of electrochemical reactions by optical detection methods, a response in the optical signal in the potential range of capacitive charging could also be observed by optical waveguide lightmode spectroscopy (OWLS) [71]. The changes in the LSPR signal have been reported [72].

However, the behavior of the optical signal response to an applied potential is still not fully understood. In the following measurements it was tried to gain deeper understanding of the optical response by analyzing three characteristic LSPR parameter. The resonance shift (plasmon energy), resonance peak height (plasmon magnitude), and radius of curvature changes of the resonance peak (plasmon lifetime) were recorded as functions of the applied potential sweeps.

4.2 Experimental setup

Gold nanoparticles (British Biocell, GC50), with a diameter of 50 nm, were deposited onto the ITO-substrate and mounted in the flow cell after the plasma cleaning procedure. This process already has been shown in chapter 3.2. For all experiments described later the flow cell was filled with sodium chloride solution. The three electrodes, namely working, reference and counter electrodes, were connected to the potentiostat. The basic principle of the measurement system can be seen in figure 4.1. The circuit was kept open for about 60 min to stabilize the signal.

To avoid the fluctuation of the light intensity during the experiment the spectrometer was always turned on 60 min before the experiment was started.

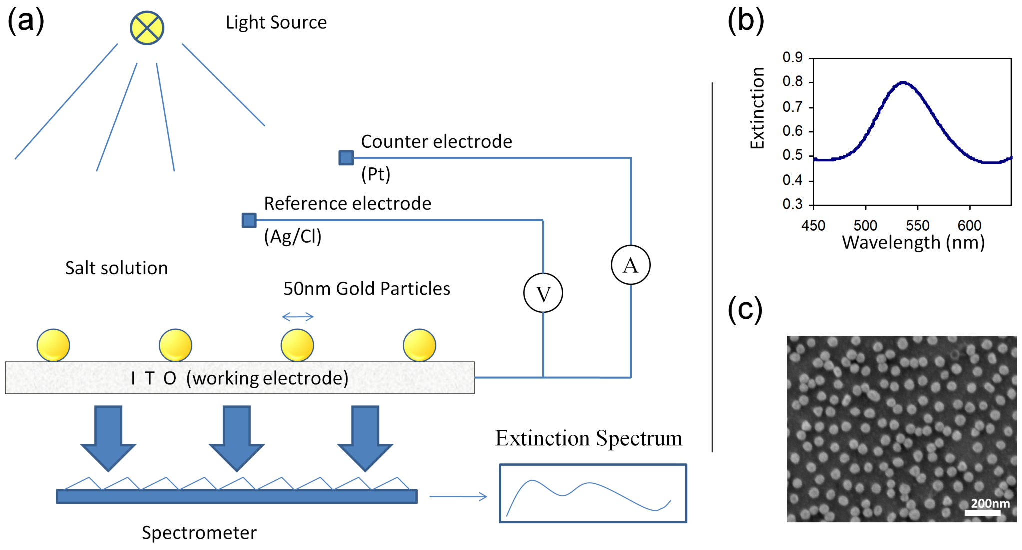

Figure 4.1: (a) Schematic illustration of the experimental setup. The flow cell was filled with salt solution and the exctinction spectrum was recorded while the voltage between the working electrode and the reference electrode was cycled between two values.

(b) Extinction spectrum and (c) SEM picture of the 50 nm gold particles immobilized on ITO.

4.2.1 Combined cyclic voltammetry and LSPR sensing

For all experiments in this section the cyclic voltammogram and the extinction spectrum were recorded simultaneously. The scan speed of the voltage sweep in the cyclic voltammetries was set to 10 mV/s.

The flow cell was mounted on the microscopy stage and adjusted so that the main point of interest on the sample was in focus. In this measurement two different read out systems were used, which have already been described in section 3.4.1. The evaluation of the recorded spectra was done by a custom-made program. The relevant peak parameters were determined by parabolic fitting of the spectra (see section 3.4.1). The peak height, peak shift and radius of curvature in the presented figures are plotted as a function of the applied potential. Since the potentiostat and the spectrometer were not time-synchronized, the voltage value in the spectrum acquisition was interpolated by the scan speed. The radius of curvature corresponds to the peak broadening. Peak broadening can occur due to a change in the nanoparticle shape or due to an accumulation of a high absorbing medium at the surrounding [73].

4.2.2 Dynamics of the electric double layer forming at different concentrations upon potential jumps

In this experiment the Ocean optics USB2000 was used because of its higher readout speed of the light intensity on the CCD-chip. The readout speed for the following presented measurements was about 25 frames per second. The preparation procedure was the same as already described in section 3.2 except that different concentrations of sodium chloride solutions were used (0.001 mM, 0.01 mM, 0.1 mM, 1 mM, 10 mM, 100 mM and 1 M). The applied voltage was changed stepwise from OCP down to 0 mV, 90 s later up to 250 mV and after 90 s the potential was released back again to 0 mV. Those potential jumps (0 mV for 90 s - 250 mV for 90 s - 0 mV for 90 s) were repeated 3 times. After each cycle (whole cycle time was 561 s), the flow cell was rinsed with deionized water (MilliQ, Millipore Corporation) and afterwards exchanged with sodium chloride solution of higher concentration. For all measurements the same substrate with deposited gold nanoparticles was used.

The extinction intensity at the resonance wavelength did not give much information as the noise level was too high whereas for resonance peak position and radius of curvature the change of the light source intensity did not play a significant role.

4.3 Results

4.3.1 LSPR response by electrochemical stimuli

Depending on the applied voltage the results are generally categorized into three types. In this thesis the most significant results are presented.

An applied voltage of maximal 500 mV

After measuring the open circuit potential for 10 s a potential between reference electrode and working electrode of 0 mV was applied. From that start potential the voltage was steadily increased up to 500 mV, decreased down to -200 mV and increased up to 0 mV again. This is defined as one cycle in the following figures. Because the first cycle always starts at equilibrium state it is inherently different from the following ones. Representatively a recorded cyclic voltammetry (measured current plotted as a function of the applied potential), the simultaneously recorded peak shift, peak height change and radius of curvature change, also plotted as a function of the applied potential, are shown in 4.2.

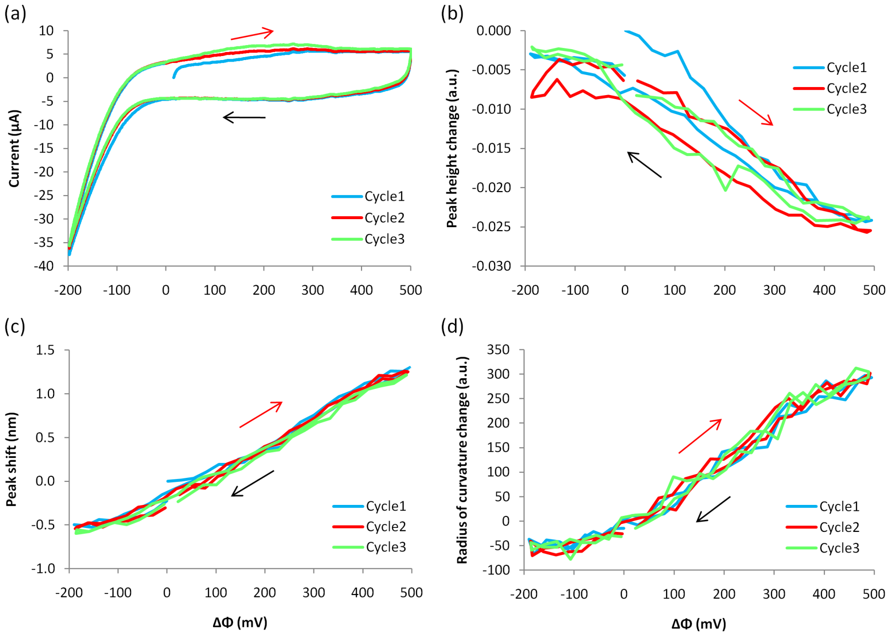

Figure 4.2: (a) Cyclic voltammetry, (b) synchronized peak position, (c) synchronized peak height and (d) synchronized peak radius of curvature plots with potential scan from −200 mV up to 500 mV in 100 mM sodium chloride solution. The three different cycles are shown in different colors. Scan speed was set to 10 mV/s.

As seen in figure 4.2a the IΦ-curve showed almost a linear increase followed by decrease of current overvoltage. Only at around 200 mV a slight increase of current is noticeable as well as hydrogen formation at the electrode at negative potential. The small peak around 200 mV could be explained by re-oxidation of hydrogen.

The corresponding resonance peak (figure 4.2b) was shifted with increasing voltage to a longer wavelength (red shift) for about 0.5 nm/200 mV resulting in an overall shift of about 1.4 nm. In this region the resonance peak shift showed linear behavior in the forward scan as well as in the backward scan. Only in the negative range a slight deviation from linearity which may correspond to hydrogen generation. The hydrogen generation is also noticeable in the cyclic voltammetry.

The radius of curvature (figure 4.2d) showed the same behavior as the peak shift, whereas there was a slightly higher deviation from linearity again in the negative region from 0 mV down to −200 mV as well as in the upper voltage region 350 mV–500 mV.

The peak height (figure 4.2c) decreased with higher voltage which indicates higher extinction intensity. Again a slight deviation from linearity can be seen in the upper (350 mV to 500 mV) as well as in the lower (0 mV to −200 mV) voltage range. Between forward and backward scan a slight hysteresis could be noticed. The first upward scan showed a higher intensity change than the following ones which may correspond to the high current seen in the cyclic voltammetry when the potential was changed from OCP to 0 mV.

An applied voltage of maximum 800 mV

In this sweep range different behavior in the LSPR-shift due to the applied potential between the forward and the backward scan was observed. Above a voltage of 300 mV the plots of the LSPR peak shift and the radius of curvature showed a hysteresis loop. The data from the cyclic voltammetry and the corresponding resonance peak parameters of the gold plasmonic nanoparticles is shown in figure 4.3.

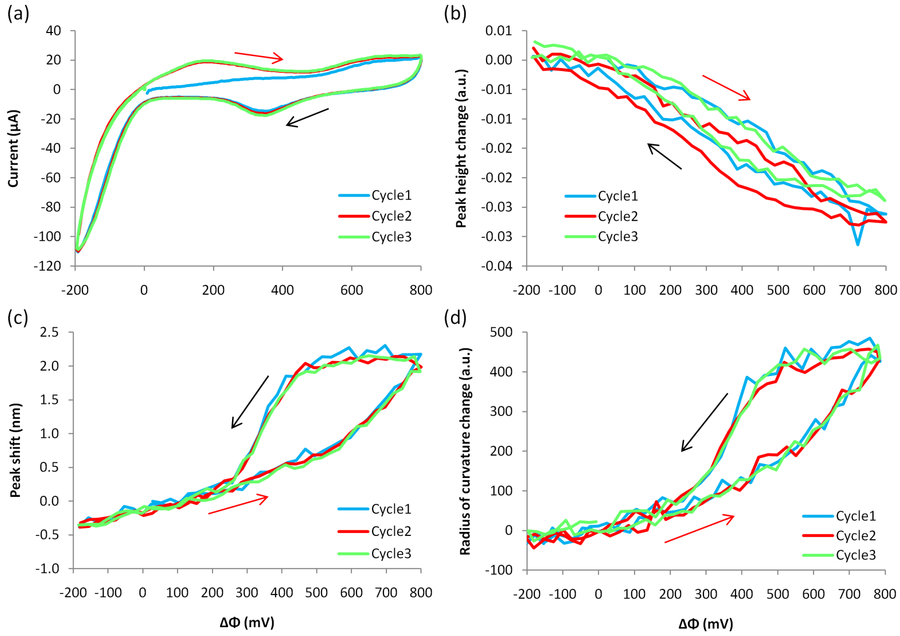

Figure 4.3: (a) Cyclic voltammetry, (b) synchronized peak position, (c) synchronized peak height and (d) synchronized peak radius of curvature plots with potential scan from −200 mV up to 800 mV in 100 mM sodium chloride solution. The three different cycles are shown in different colors. Scan speed was set to 10 mV/s.

This time the IΦ-curve (figure 4.3a) showed a slightly greater increase of current than in 4.2 at about 200 mV which is probably re-oxidation of hydrogen. At 420 mV the current started to increase again, reaching its peak value at about 650 mV. In the backward scan only one obvious peak at 360 mV was noticed together with again the hydrogen formation in the negative voltage range.

During the forward scan, the resonance wavelength increased linear to the potential up to 500 mV, deviated at higher potential and dropped back to the linear curve at around 400 mV during the backward scan (figure 4.3b). The deviation from linearity matched with the current increase at the voltammogram at 650 mV and 360 mV. Similar to the peak shift response in figure 4.2b, the wavelength with increasing voltage is again shifted more into the red by about 2.4 nm.

The same behavior as for the resonance peak shift was also shown by the radius of curvature (figure 4.3d). Whereas in the peak intensity change (figure 4.3c) the hysteresis could not be clearly observed.

All changes of parameters showed reversible behavior.

An applied voltage over 1000 mV

At a higher voltage range the resonance peak shift lost its linear behavior. For the results seen in figure 4.4, the voltage between the reference and the working electrode was increased up to 1500 mV.

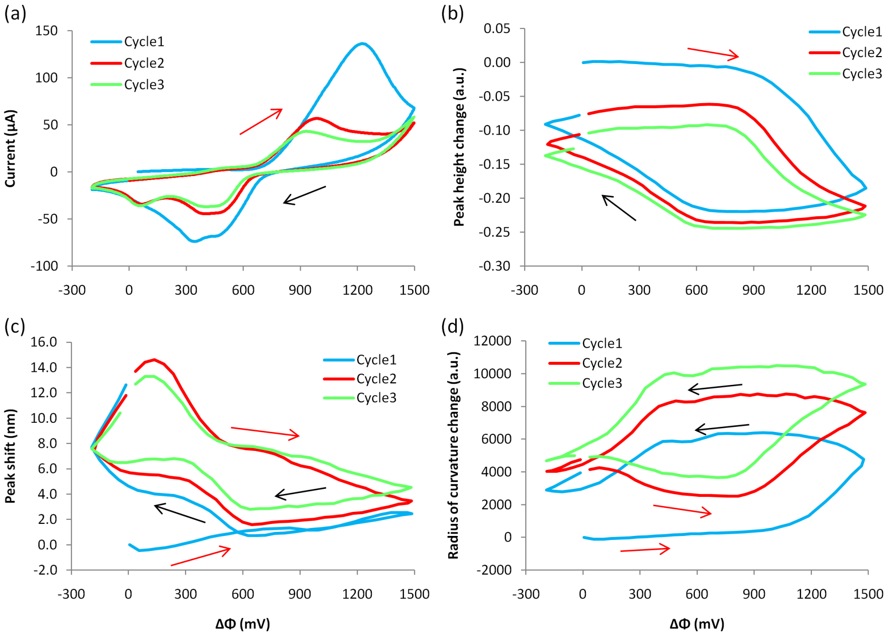

Figure 4.4: (a) Cyclic voltammetry, (b) synchronized peak position, (c) synchronized peak height and (d) synchronized peak radius of curvature plots with potential scan from −200 mV up to 1500 mV in 100 mM sodium chloride solution. The three different cycles are shown in different colors. Scan speed was set to 10 mV/s.

A slight increase in the current with its peak at about 520 mV was overlaid to the almost linear increase in the beginning (figure 4.4a). Between the different cycles the peaks in the cyclic voltammetry at about 1200 mV showed a significant change. The high current peak in the forward scan shifted from 1200 mV at the first cycle, forwarded to 950 mV in the second and 910 mV respectively in the third cycle. The current itself decreased for almost 70 %, from 133 µA down to 56 µA from the first to the second cycle and to 40 mV in the third cycle. At the applied potential of 1500 mV the current changed from 71 µA at the first cycle to 55.8 µA at the second cycle and 51.6 µA in the third.

In the backward scan the peak in the current at 350 mV also decreased, and seemed to shift to an applied voltage of 60 mV in the second and third scan. The value of the current decreased from −73 µA in first cycle down to −45 µA in the second cycle and finally to −36 µA in the third cycle. Altogether, a current decrease of about 50 % occurred.

The LSPR wavelength shift corresponding to the described voltammetry can be seen in figure 4.4b. In the first cycle the resonance peak again started with an almost linear shift and saturated at about 700 mV. With increasing voltage the shift first decreased but increased again until the turning point of the voltage. In the forward scan of the first cycle the overall red shift was about 3 nm. The first remarkable difference to the other two scans occurred in the backward scan of the first cycle. The peak shift decreased linearly back to 530 nm but started to increase at 630 mV up to a wavelength of about 539 nm at −200 mV. This behavior in the backward scan stayed the same over all three cycles: first the linear decrease during 1500 mV to 630 mV and afterwards an increase of the resonance wavelength up to 539 nm. At 1500 mV, at the starting point of the backward scan, the resonance wavelength shift increased 1nm in each cycle (1.Cycle about 534 nm, 2.Cycle about 535 nm and 3.Cycle about 536 nm).

In the second and third cycle the peak shift in the forward scan increased steeply to a resonance wavelength of 546 nm in the second and 544 nm in the third scan at a voltage of 135 mV. After this peak value the resonance wavelength decreased again steeply down to 539 nm at 516 mV and less steep, down to 535 nm in the second cycle respectively 536 nm in the third cycle at a voltage of 1500 mV. The overall peak shift was 13 nm, measured from the peak in the backward scan at 627 mV to the peak in the forward scan at 135 mV.

The change in the radius of curvature increased in the first forward scan very slightly linear until a voltage of about 1000 mV (figure 4.4d). From that point the radius of curvature increased rapidly until the turning point of the forward scan and a slight increase until the applied potential came back again to 1000 mV in the backward scan. Afterwards it almost stayed constant until it started to decrease again at an applied voltage of 400 mV. When the applied voltage was flipped at −200 mV the value of the radius of curvature increased again until an applied potential of 0 mV. In the second and third scan the radius of curvature first decreased from 0 mV until 300 mV in the forward scan and a very slight decrease until about 900 mV where the curvature showed again a fast increase until a voltage of

1500 mV in the forward scan. The backward scan looked similar to the first scan cycle. It started with a very slight increase until the applied voltage reached 1000 mV then stayed almost constant down to an applied voltage of 400 mV where it decreased and after the turning point increased again.

The peak height changed basically opposite to the radius of curvature (figure 4.4c). When the curvature increased, a decrease in the peak height could be noticed and vice versa. When the applied voltage in the backward scan reached the turning point the peak height was slightly lower than the one at the maximum applied voltage of 1500 mV. The overall peak height decreased over the three cycles.

After the scan was finished the surface had noticeably changed. To get more details from the changes of the surface the sample was examined in an scanning electron microscope (SEM). As seen in figure 4.5 the SEM scan showed that in some regions the gold nanoparticles shrank whereas in other regions on the surface, they agglomerated.

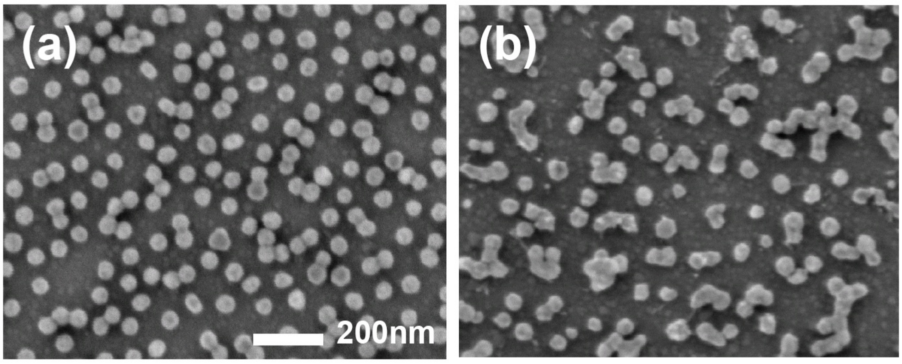

Figure 4.5: SEM pictures taken after the cyclic voltammetry with a scan range from (a)−200 mV to 800 mV and (b) −200 mV to 1500 mV. Both samples were used the first time.

4.3.2 Dynamics of the electric double layer forming at different concentrations

It was expected to gain more information of the dynamics of electric double layer forming from the measurement of the localized surface plasmon resonance shift at different concentrations of the solution.

In figure 4.6 the recorded resonance peak shift after stepwise potential application at different salt concentrations are plotted over time.

Although the signal from the measurement with 0.1 mM concentrated sodium chloride solution was unstable, the overall shift of the LSPR frequency shift tended to be higher for higher salt concentration and the overall shift was decreasing when measured in solutions

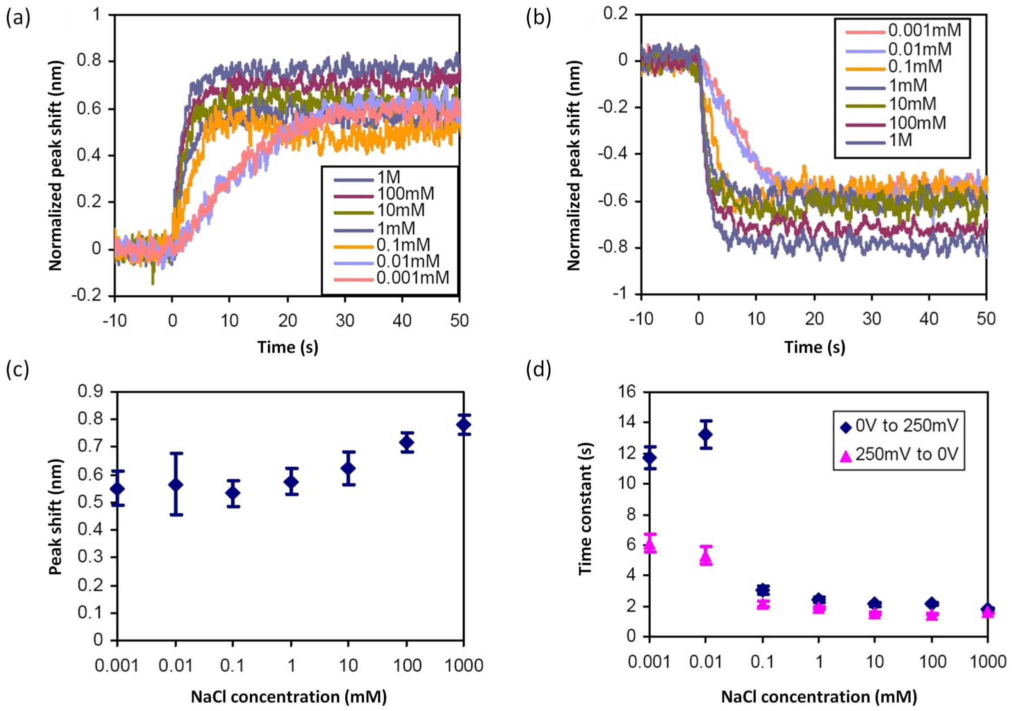

Figure 4.6: Dynamics of the peak shift at different concentrations after a stepwise potential was applied.

(a) The potential step was applied from 0 mV to 250 mV and for (b) from 250 mV to 0 mV. The magnitudes are normalized to the measurement at a concentration of 1 M to eliminate the variation of different samples and positions. The overall peak shift at different concentrations is again summarized in (c). The time constant for potential application from 0 mV to 250 mV and 250 mV to 0 mV respectivley are shown in (d).

with less salt concentration. For lower salt concentrations also a slower dynamic of the resonance peak and curvature shift could be seen. This behavior was similar for the positive jump of potential as well as for the negative jump of potential. At concentrations less than 0.01 mM no difference in the peak and curvature shift response to the applied voltage jump could be seen. The electrochemical cell can also be interpreted by a resistance-capacitor pair where the charge at one side of the electrode is optically monitored [74], [75]. The related time constant of the equivalent circuit (product of capacitance and resistance) is thus also related to the concentration. The concentration dependent part of the resistance is mainly the resistance of the solution and therefore inversely proportional to the ion concentration. The capacitance corresponds to the diffusion layer capacitance, which is proportional to the square root of the concentration [76]. The time constants of the different concentrations are plotted in 4.6d. With increasing concentrations the time constant decreased, whereas with higher salt concentrations (>1 mM) this effect was reduced. This is probably due to the higher value of the Stern layer capacitance.

4.4 Discussion

Parallel to the presented experiments, a numerical simulation of the system was done by a multiple multi-pole program (MMP). The predictions of the simulation helped to give a better interpretation of the above presented measurements and will therefore be included in the following discussion even if the simulations were not focus of this work (see also [77]). In all cyclic voltammetry scans up to 800 mV the shift of the LSPR peak was reversible which indicated that at the end of the scan the gold particles did not differ from their original state. This could also be confirmed by the SEM images which were taken after the scan (figure 4.5).

4.4.1 An applied voltage of maximal 500 mV

According to the DLVO theory, the applied potential at the surface will form an electric double layer in solution. Close to the surface, formation of the dense Stern layer will occur, merging into bulk concentration through diffusion layer at greater distance from the surface. Due to the application of positive potential at the sample surface, molecules residing on the surface will be displaced by chloride ions. Finally the Stern layer will consists merely of chloride ions. Hydrated chloride ions show a higher polarizability (see B) than water and, as it can be seen in equation 2.11, a change to a higher refractive index in the surrounding of a plasmonic nanoparticle will result in a red shift of the resonance peak [32]. Indeed the experiments showed an increasing red shift of the LSPR-peak when the voltage was increased (figures 4.2b to 4.4b). This sensibility of the system against the double layer formation could be confirmed by application of a jump potential to solutions of different concentrations. The difference in the chloride concentration will lead to a different shielding of the electric field (see 2.2.1). Therefore the structure of the electric double layer will change. This fits the peak shift response in 4.6.

Beside the LSPR peak shift, an increasing radius of curvature and a decreasing absorption were noticed in the scans. This is contrary to the effect expected by the refractive index change due to the electric double layer formation. According to equation 2.7, the higher dielectric constant of the chloride layer would result in an enlarged extinction cross section lowering the detected intensity on the CCD. Furthermore, the broadening of the resonance peak is related to the dephasing of the collective plasma oscillations and therefore more influenced by the properties of the plasmon supporting media than by the surrounding. Change in the electron density inside the gold particles close to their surface would be an explanation of the recorded resonance damping (intensity decrease and peak broadening, *i.e.*, radius of curvature increase). The formation of chloride ions on the surface could cause a change of the electron density in the presented system. Since charge compensation of the negative ion at the surface lead to electron depletion inside the gold nanoparticles close to their surface.

In the work of Xia *et al.* [78] it has been shown that already at potentials lower than the reaction potential, formation of metal oxide or metal halide could be possible. This would also give a possible explanation of the plasmon damping in figure 4.2. Chemical bonds of the atoms close to the surface would occur (chemisorption) leading to a electron depletion in the outer region of the gold particle.

To be able to find the coherent scenario for the measured resonance response of the system, the in the following described models were simulated (MMP-simulation) and compared. The influence of the ITO substrate below the plasmonic nanoparticles is negligible since the contact area is expected to be small. The hot spot, where the strong electric field is excited, is typically at the side of the particle with transmission configuration, therefore resulting in negligible sensitivity to the substrate. Therefore only scattering on free particles was simulated to gain higher accuracy because of the lowered computer load.

Formation of chloride ion layer

For the simulation of the spectra, the dielectric constant of chloride layer was calculated according to the Clausius-Mosotti equation (see B equation B.1). Previous to the simulation an estimation of the concentration of chloride ions in the diffusion layer was done according to the Gouy-Chapmann theory of charged interfaces. It showed that with a reasonable effective surface potential ($<100\,\mathrm{mV}$) only a shift smaller than $0.2\,\mathrm{nm}$ can be explained (section B).

Thus, for the simulation, only a dense monolayer of chloride ions (ionic diameter $0.362\,\mathrm{nm}$ [79]) was considered neglecting the diffusion layer into the bulk. The hexag-

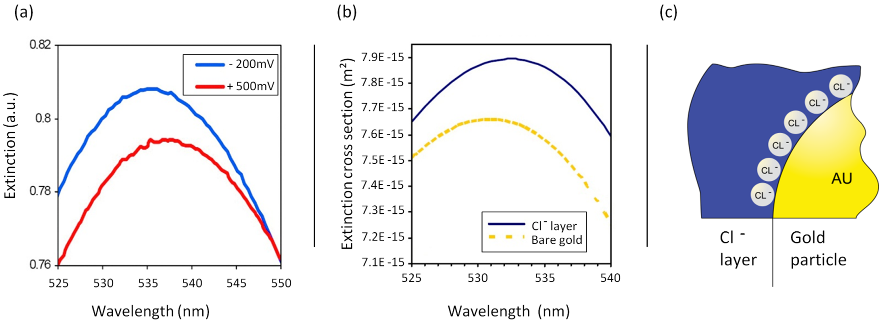

Figure 4.7: Simulation results of the LSPR peak shift due to a chloride monolayer at the surface of the gold nanoparticle compared with the experimental extinction spectra.
(a) Magnified experimental extinction spectra at the potential of −200 mV and 500 mV.(b) Simulated extinction spectra with chloride ion layer of 0.362 nm adsorbed at the surface.(c) Schematic illustration of the gold particle with the adsorbed chloride ions similar to the simulation model.

onal packing resulted in a dielectric constant of the chloride monolayer of 3.0.
The results (figure 4.7) showed a resonance peak shift of 1.2 nm which was less than the 1.4 nm in the experiment. Besides the model resulted in a slight plasmon energy increase (peak height) together with a raduis of curvature decrease, not explaining the observed resonance damping in the experiment. Considering that such a dense packing of chloride ions is overestimated, the measured LSPR response can not be explained solely by simple ion adlayer formation.

Electron depletion layer inside the particle

The second model tried to investigate the influence of electron depletion on the LSPR response. Considering only the depletion of the conduction band, the electron depletion can be directly related to the Drude plasma frequency [80]. The change in the volume plasma frequency will furthermore lead to different optical properties. For the calculation of the dielectric constant the modified Drude model, similar to the one proposed by Etchegoin *et al*. [81] was used.

$$\epsilon_{Au}(\lambda) = \epsilon_\infty - \frac{1}{\frac{\lambda_p^2}{\lambda}\left(\frac{1}{\lambda} - \frac{\mathrm{j}}{\gamma_p}\right)} + \sum_{i=1,2}\left(\frac{A_i}{\lambda_i}\left[\frac{\mathrm{e}^{j\phi_i}}{\frac{1}{\lambda_i} - \frac{1}{\lambda} - \frac{\mathrm{j}}{\gamma_i}} + \frac{\mathrm{e}^{-\mathrm{j}\phi_i}}{\frac{1}{\lambda_i} + \frac{1}{\lambda} + \frac{\mathrm{j}}{\gamma_i}}\right]\right) \tag{4.1}$$

The parameters in the equation were obtained by fitting the model with the experimental data for the dielectric constant of gold by Johnson and Christy [41]. With increasing depletion, the real part of the dielectric constant of gold becomes positive, giving rise to non-metallic behavior of the depletion layer. The influence of the depletion on the imaginary part was marginal, whereas it needs to be mentioned that only the Drude term was

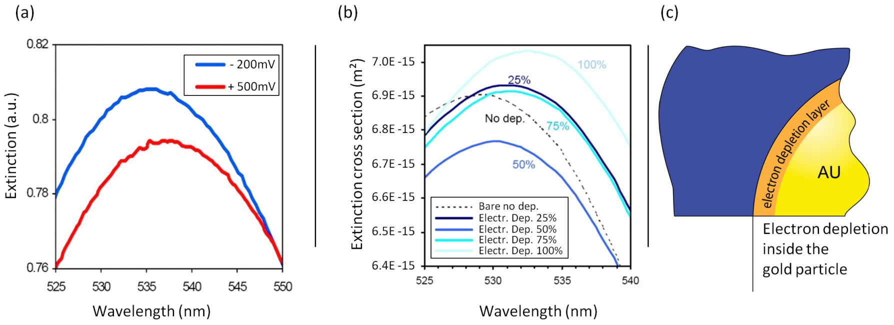

Figure 4.8: Simulation results of the LSPR peak shift response to electron depletion at the gold surface, compared with the experimental extinction spectra.
(a) Magnified experimental extinction spectra at the potential of $-200\,\text{mV}$ and $500\,\text{mV}$. (b) Simulated extinction spectra for pure depletion layer with $0\,\%$(bare), $25\,\%$, $50\,\%$, $75\,\%$ and $100\,\%$ electron depletion at the outmost $0.28\,\text{nm}$ of the gold surface. (c) Schematic illustration of the electron depletion layer.

linearly changed with increasing depletion ($0\,\%$, $25\,\%$, $50\,\%$ and $75\,\%$ depletion).
In figure 4.8b, the results of the simulation at different electron densities are shown. Depletion was approximated to occur within the thickness of one atomic layer. Therefore the depletion layer was introduced in the simulation as a $0.28\,\text{nm}$ shell inside the metal using the different dielectric constants. As it can be seen, the spectra response showed a quite complex behavior which can most probably be explained by the high variation of the real part of the dielectric constant in the range of the resonance wavelength ($500\,\text{nm}$–$550\,\text{nm}$) [73].

Formation of an absorbing layer due to metal halide formation

The results from the electron depletion layer led to the last model where an oxide/halide formation was assumed in the interface area. Even below the oxidation potential some groups observed a pre-oxide formation at the surface [78]. Such pre-oxide layer would have absorbing properties (non-zero imaginary part of the dielectric constant) comparable to the simulated depletion layer [82]. Therefore it was expected that such absorbing layer would also be generated by gold-chloride ion pair. Observed resonance damping, which is essentially the lowering of peak height and the increase of radius of curvature (peak broadening) could already be observed due to the silver iodine formation in the study by Mulvaney [80].

In the simulation model, a gold pre-oxide/chloride layer was introduced as an absorbing (lossy) layer (figure 4.9b) at the interface with a thickness of $0.23\,\text{nm}$ ($\sim$size of an atomic monolayer). Half of the layer was inside and half of it was outside since it was assumed

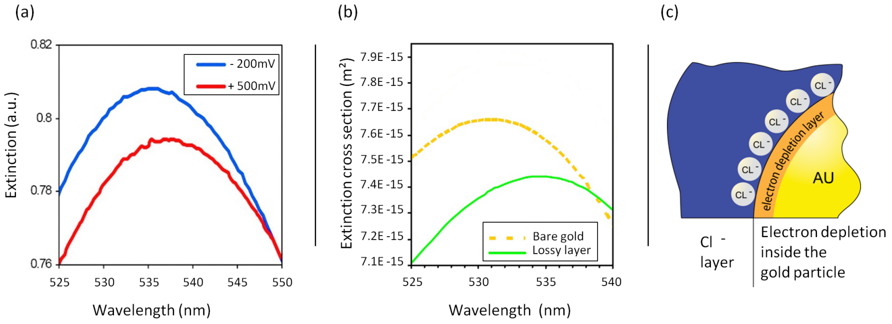

Figure 4.9: Simulation results of the LSPR peak shift response to lossy layer formation at the gold surface, compared with the experimental extinction spectra.
(a) Magnified experimental extinction spectra at the potential of −200 mV and 500 mV. (b) Simulated extinction spectrum for lossy layer formation at the outmost 0.23 nm of the gold surface compared to the extinction spectrum of bare gold. (c) Schematic illustration of the lossy layer consisting of adsorbed ions at the surface and a resulting electron depletion layer at the gold.

that the layer will be formed together with the adsorbed ions leading to a change in the electron density in the metal. The resulting simulated resonance peak shift is shown in figure 4.12.

Considering the three simulations it seems that the only possible explanation of the observed LSPR response in the experiments is a resonance damping by depletion of the valence electrons.

4.4.2 Kinetics and salt concentration

Due to the different concentrations of ions in the solution, the time until the potential distribution stabilized was also expected to be different. At lower ion concentrations less charge carriers are available in solution leading to a longer relaxation time of the system. Hence the formation of the electric double layer will also take longer, until enough ions reside on the surface to establish the potential. As it can be seen in figure 4.6, the response in the resonance peak shift at a positive applied potential really showed a slower response at lower concentrations.

Below a salt concentration of 0.01 mM the kinetics were roughly the same. At this low salt concentration the hydrogen carbonate which is typically present (concentration of ∼0.001 mM–0.01 mM HCO_3^-) probably starts to play a role.

When the salt concentration was higher than 1 mM, the change in the time constant was not significant anymore. The most likely explanation is, that at these concentrations the potential distribution is less affected by the diffusion layer and the solution resistance than by closer vicinity of the electrode (Stern layer capacitance).

The peak shift responded similar when the potential was released as shown in figure 4.6b.

Again at lower salt concentrations the time until the peak shift stabilized increased. This means that at lower salt concentrations, the negatively charged ions reside longer at the surface. Since the desorption also includes a restructuring of the surface layer, a possible explanation could be that a decoupling of the negative ions and the positive surface holes is only possible when the charge in the metal is effectively screened. Again, the time until a counter ion arrives at the surface would be dependent on the concentration.

4.4.3 An applied voltage of maximum 800 mV

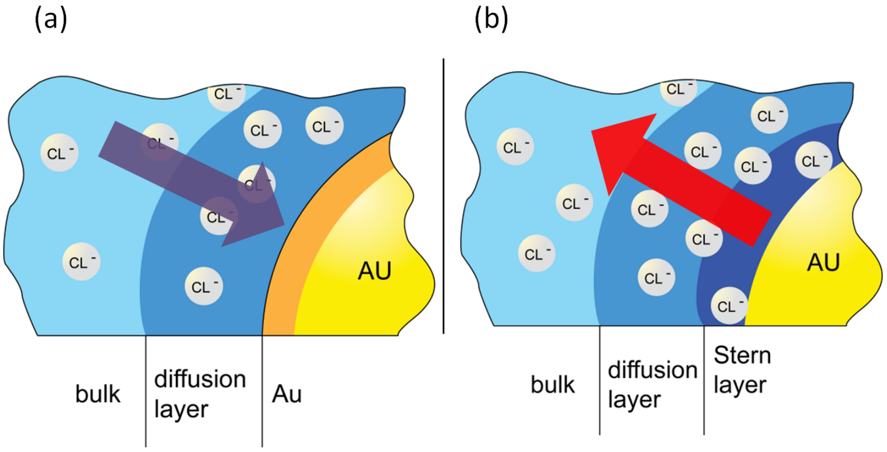

Figure 4.10: Schematics of the surface region during the forward and backward scan respectively at an applied potential of maximal 800 mV.
(a) During the forward scan chloride ions are attracted to the surface and gold chloride is formed at the layer outside the gold particle. (b) This layer is again fully desorbed in the backward scan and the chloride ions dissolve into the solution.
The probably occuring electron depletion at the outmost gold surface is not shown in the figures.

At this voltage level, a reaction was already noticeable in the related cyclic voltammetry (figure 4.3a). The oxidation and reduction peaks correspond to the reported standard potential in literature for gold chloride reaction ([83]; $[AuCl_4]^- + 3e^- \rightleftharpoons Au(s) + 4Cl^-$). Again the gold chloride formation on the surface could be introduced as a lossy layer at the interface (electron depletion due to chemisorption), which would be consistent with the simulation. When the applied potential is released again this process must be fully reversible since the measured LSPR parameter returned back to their initial values. Since the reduction process needs a certain excess potential, this would explain the hysteresis loop. In figure 4.10 schematics of the different surface structure in vicinity of gold between the forward and backward scan are shown.

4.4.4 An applied voltage over 1000 mV

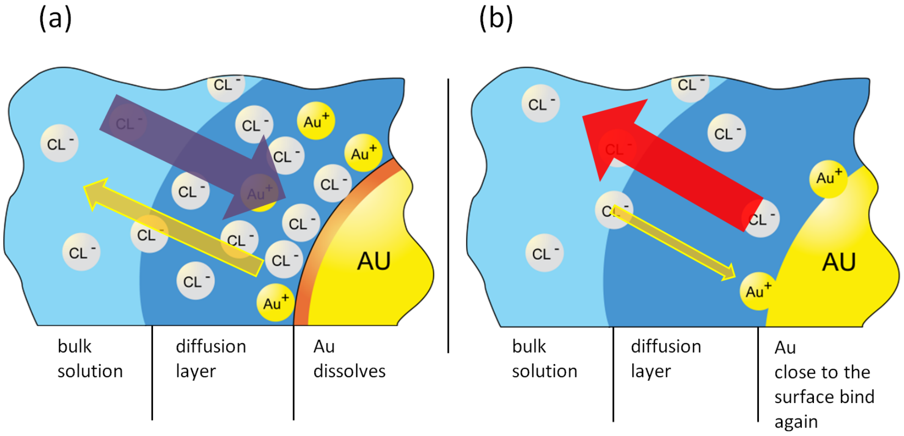

Figure 4.11: Schematics of the surface region during the forward and backward scan respectively at an applied potential of maximal 1500 mV.
(a) During the forward scan chloride ions are attracted to the surface. At this potential range the excess potential of gold oxidation is already reached. Gold ions dissolve into solution. (b) In the backward scan some of the gold ions are re-positioned during the reduction process. Note that the particle shape changes during the process indicated in (b) by a shrank particle (the black line indicates the old interface).

According to literature values, oxidation of gold was expected at a voltage level around 1 V against Ag/AgCl [82]. Applying a voltage in this range showed clearly a change in the resonance peak response. The irreversibly in the LSPR peak response to the applied voltage indicated a permanent change in either the particle shape or size [44],[45]. This theory was supported by the SEM pictures taken after the scan, which showed clearly different shaped particles and coagulated gold particles at some places. Dissolution of gold ions into the solution followed by the re-deposition during the reduction process could caused transformation of the particle shape. In figure 4.11, schematics of the surface structure in the forward and backward scan respectively are shown. Coagulation of the particles could be explained by a lost connection of whole gold particles to the ITO substrate. This would release the applied potential to the particle and the particle would immediately be attracted again by the positive voltage and reconnect.

4.5 Conclusion

In conclusion, the results of a combined electrochemical and optical sensor have been presented in this chapter. Cyclic voltammetry and LSPR sensing were synchronized to investigate the sensitivity of the LSPR to the electrochemical processes. At an applied potential where no reaction was expected, an almost linear shift of the LSPR peak to lower frequencies was recorded when increasing the positive applied potential on the working electrode. The observed increase in the radius of curvature of the resonance as well as the absorption decrease at the resonance frequency could not be explained by the expected EDL-formation alone. In figure 4.12, the recorded peak height change and radius of curvature change is shown in comparison with the results of the different simulations. Numerical simulation therefore suggested a formation of a lossy layer by electron depletion and negative ion adsorption.

At higher applied potentials reaction could already be observed in the CV suggestion gold halide formation. Again the recorded LSPR peak response was explained by electron depletion inside the gold nanoparticles close to their surface due to the binding. This process showed to be totally reversible since the peak parameter decreased to their primary state again.

At an applied potential above the oxidation potential of gold, gold was found to be dissolved and during the reduction re-deposited. This resulted in an irreversible spectra response of the LSPR peak parameters.

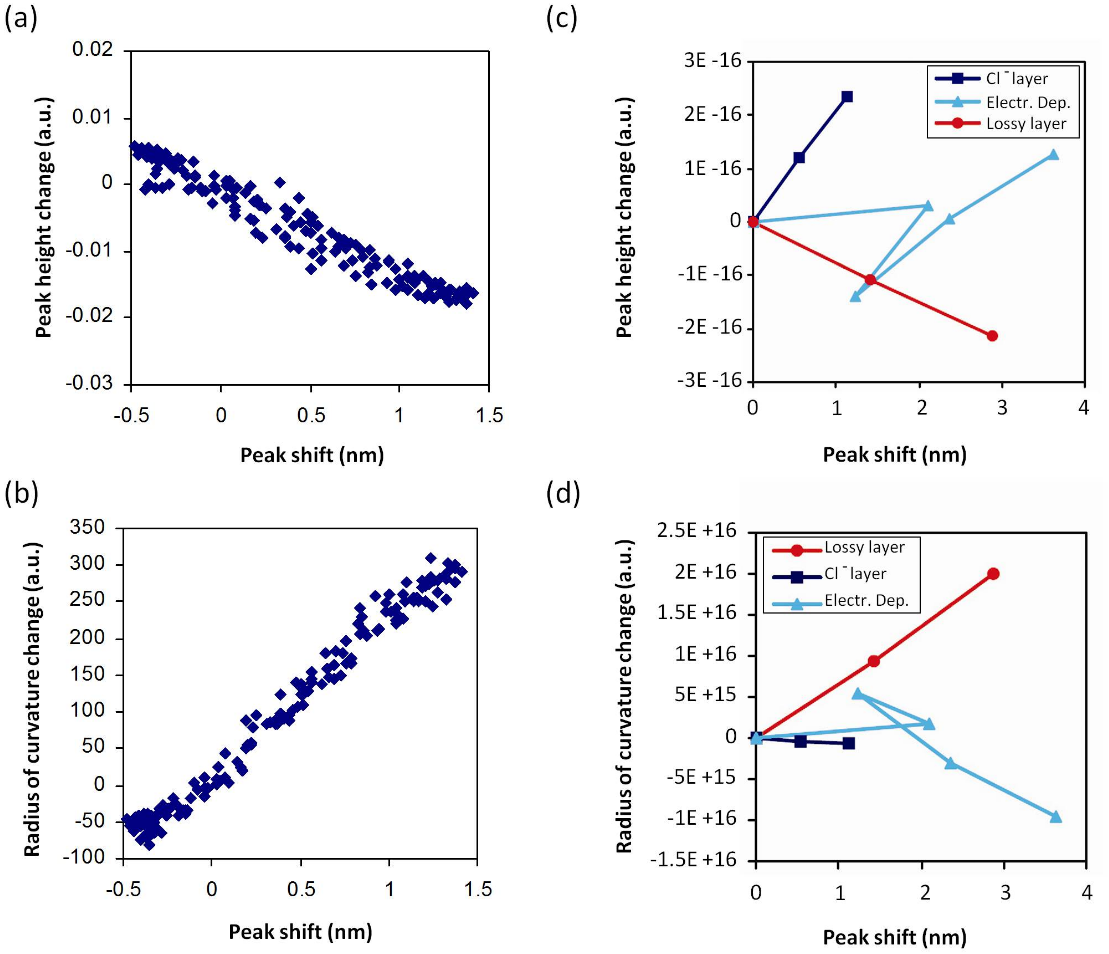

Figure 4.12: Summary of the different simulation results compared with the experimental results. (a) Peak height change and (b) radius of curvature change of the experimental results at the scan range of −200 mV to 500 mV.(c) Results of the different simulated layer models of the resonance peak height chance and the (d) radius of curvature change. The lines and points of the depletion layer correspond to: bare(origin), 25 %, 50 %, 75 % and 100 % (peak shift of 3.8 nm) of electron depletion at the outmost 0.28 nm of the gold surface. The lines are connected in the same order. Note that the simulation results are based on extinction cross section, while the experimental values are based on extinction.

Chapter 5

Enhancement of chemical reaction by LSPR

5.1 Introduction

In this chapter the measurements on an influence of LSPR on the electron transfer rate in electrochemical surface reactions are presented. In several works the enhancement effect due to surface collective oscillations has been reported [84]. The local field enhancement due to the interference of surface plasmon polaritons is utilized in surface enhanced Raman scattering (SERS) [85], [86], but also showed to have an important influence in laser assisted field emission [87]. The possible excitation of the surface plasmon band of gold nanoparticles, with light in the visible frequency range, was furthermore reported to be successfully utilized in charge separation processes at functionalized gold nanoparticles [88], [89], [90].

As already mentioned in section 2.2.3, the rate constant at electrochemical reactions at electrodes is highly dependent on the electric field over the surface layer. The local field enhancement at the LSPR could therefore influence the reaction occurring at the electrode (gold nanoparticle-electrolyte) interface. To investigate the influence of light on the electron transfer rate in the used setup, the current was recorded at a constant voltage with and without light.

5.2 Experimental setup

Depending on the experiment three different substrates were used. A bare ITO slide, like the one used for gold deposition (see section 3.2), was used for the control experiments.

For the solid gold film the glass slide was cleaned and sputter coated with an adhesive layer of approximately 2 nm of chromium followed by a deposition of 70 nm of gold. Before the slide was mounted into the smaller flow cell (see section 3.1), it was rinsed with water, with sodium dodecyl sulfate (SDS) and pure Isopropanol and gently wiped during rinsing to remove contamination from the former experiments.

Gold plasmonic nanoparticles were deposited on the bare ITO slide as described in section 3.2.

Once the sample and the flow cell were cleaned and treated in the plasma following the procedures from section 3.2.2, the samples were mounted in the flow cell and filled with solution. Afterwards the three electrodes (working electrode, reference electrode and counter electrode) were connected to the potentiostat and the circuit was kept open for about 60 min to stabilize the electrode layer. In 5.1 the basic principle of the measurement system can be seen.

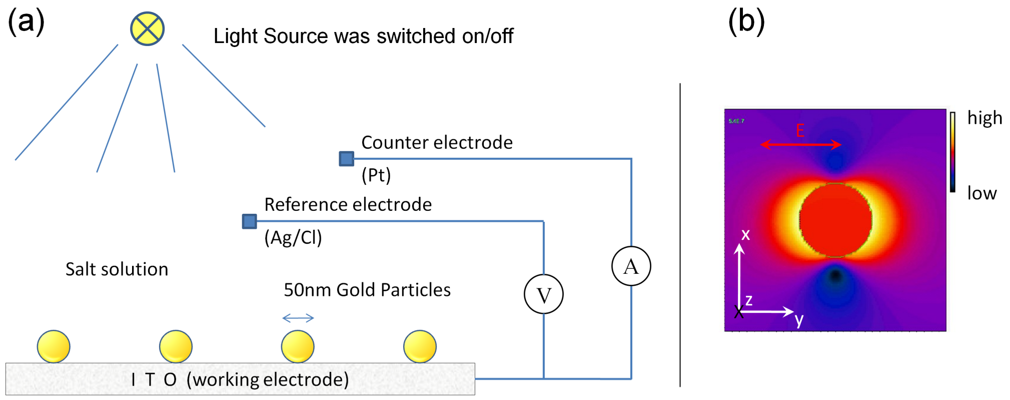

Figure 5.1: (a)Schematic illustration of the experimental setup. The flow cell was filled with salt solution and the current density was recorded at constant applied potential between the working electrode and the reference electrode. During the measurement the light was turned on and off. (b) Simulation of a 10 nm gold particle in water excited at the wavelength of 540 nm, which shows the localized field enhancement close to the surface.

The aim of this experiment was to see a current increase due to the increased reaction speed when the particles were illuminated by light. Therefore the potential between the reference and working electrode was kept constant and the current was recorded with the potentiostat. For illumination, a commercially available halogen and Xenon lamp have been used to see the effect of two different intensities. Unless specially noted, an IR-filter (cutoff of frequencies above ∼700 nm) and a UV-filter (cutoff of frequencies below 475 nm) have been used in the illumination path. After the current at a certain applied potential stabilized, a mechanical switch was opened, the light was guided through the optical system of the microscope and illuminated the sample. Since the absorption spectra was not expected to give any relevant information and the light power already saturated the CCD-device the absorption spectra was not recorded. Except for the experiment with the glass covered by a solid gold film, the same flow cell was used for all experiments (section 3.1). For the measurement with the solid gold film a smaller flow cell was used.

5.3 Results

In this section the main results are summarized. First the test of light influence on bare ITO substrate is presented.

5.3.1 Bare ITO

In this experiment, shown in figure 5.2, influence of light on the semiconductor substrate, *i.e.* ITO, was investigated at different applied potentials. Frequencies below a wavelength of 475 nm were cut out by a filter except at the measurement above 900 s in figure 5.2d where the filter was removed to see the effect of higher energy photons.

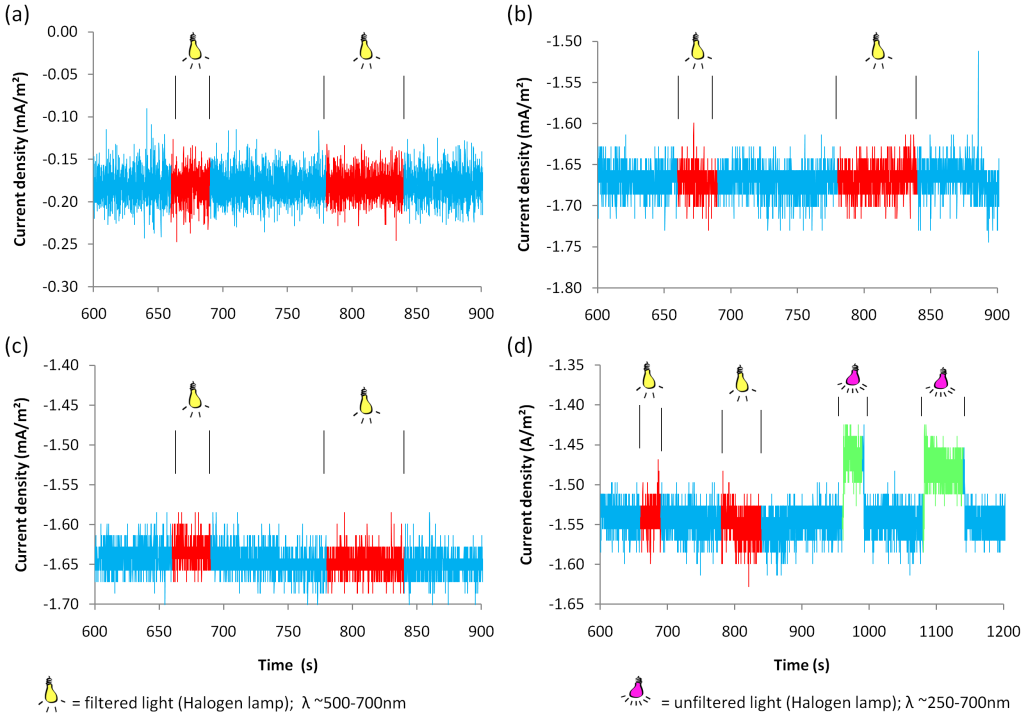

Figure 5.2: Recorded current density at constant applied potentials plotted as a function of time. The recorded current density when the light was turned on is indicated in a different color. The applied potential was (a) 100 mV, (b) 350 mV, (c) 500 mV and (d) 750 mV. In figure (d) the UV-filter was removed before the last two times the light was turned on. This is indicated with green color.

100 mV

In figure 5.2a the response in the current density over time, at an applied voltage of 100 mV is shown. After 660 s a mechanical shutter was switched and the light was shined onto the sample. As it can be seen in figure 5.2a no change in the current density could be observed when the sample was illuminated.
The light was switched off after 30 s and switched on again at an overall recording time of 780 s. Also at this time no change in the recorded current density during the 60 s of illumination could be noticed.

350 mV and 500 mV

The recorded current density at an applied potential of 350 mV is shown in figure 5.2b. Again no change in the current density between the illuminated sample (second 660 to 690 and second 780 to 840) and the sample measured in the dark was noticed. Also at 500 mV, no increase in the current density was noticed when the sample was illuminated by halogen light (second 660 to 690 and second 780 to 840) as shown in figure 5.2c.

750 mV

When the bare ITO sample was measured at 750 mV with the UV-filter present, again no difference in the current density between the illuminated sample (second 660 to 690 and second 680 to 840) and the sample measured in the dark was recorded as shown in figure 5.2d.
Only when the UV-filter was removed (second 960 to 990 and second 1080 to 1140), an increase in the current by 1 mA/m^2 at a clamped voltage of 750 mV, could be investigated. The current increased immediately after the light was turned on and decreased to its primary state after the light was turned off again.

5.3.2 ITO covered with plasmonic nanoparticles

In figure 5.3 the current increase due to the light at different voltage levels is shown when a sodium chloride solution was used on gold nanoparticles deposited on an ITO substrate. Again an additional filter was used to cut out frequencies higher than 475 nm.

100 mV

At an applied voltage of 100 mV as shown in figure 5.3a, no increase in the current density was noticed when sample was illuminated with the halogen lamp.

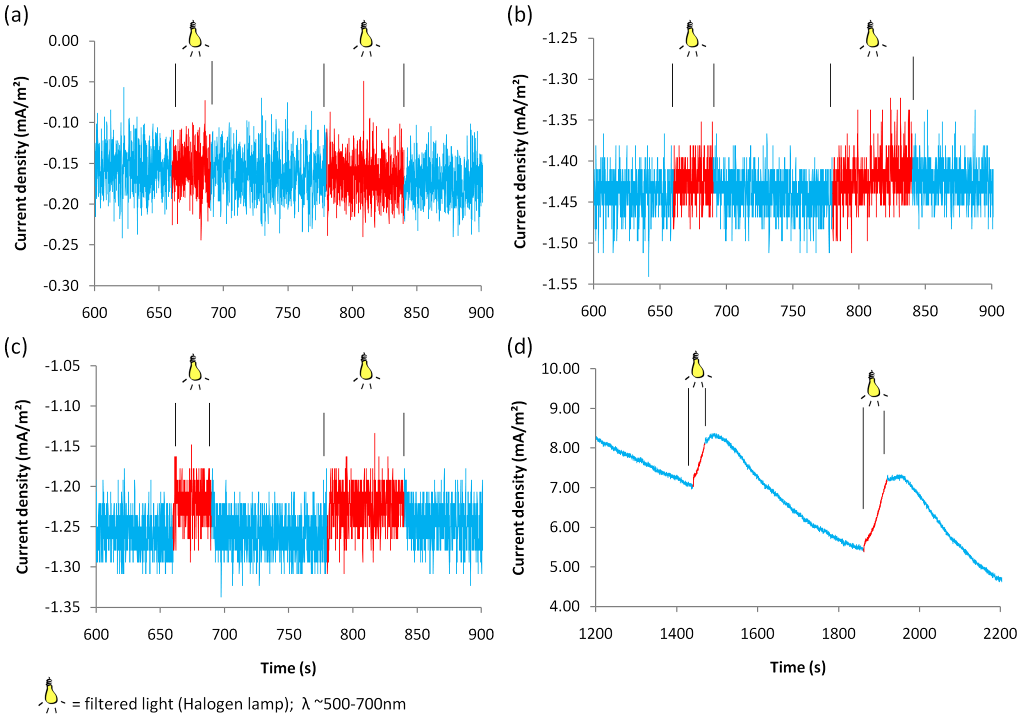

Figure 5.3: Recorded current density at constant applied potentials plotted as a function of time. The recorded current density when the light was turned on is indicated in a different color. The applied potential was (a) 100 mV, (b) 350 mV, (c) 500 mV and (d) 750 mV.

350 mV

In these plots already at a voltage of 350 mV (figure 5.3b), a slight increase in the current was observed after the light was turned on. Over a period of one minute, the increase in current density is about 14 µA/m^2 followed by the same amount of decrease back to the value before the light was turned on, whereas due to the noise level it is hard to analyze the kinetics.

500 mV

At a voltage level of 500 mV, again only a slight increase in the current density could be noticed as seen in figure 5.3c. The current density increase is about 29 µA/m^2 over a time of 1 min. Again due to the low signal to noise ratio, it was hard to tell if the current density increased immediately or gradually.

750 mV

When the applied voltage was increased over 700 mV, an obvious change in the current response due to the light emittance could be noticed as it can be seen in figure 5.3d. The figure shows the current increase at a fixed voltage of 750 mV. When the light was turned on (second 1440 to 1470) the current density raised within 50 ms by about 0.08 mA/m^2 and afterwards increased slightly by 0.93 mA/m^2 over a time of 29 s. Shortly after the light was turned off the current jumped back by about 0.07 mA/m^2 within 1.65 s but still increased slightly for another 10 s, stayed almost constant for about 20 s and later decreased slightly. The current before the light was turned on had a slight decrease, if this decrease is interpolated over the time, it could be assumed that the current after the light was turned off decreased back to the initial state when the light was turned off.

The second time the light was switched on (second 1862 to 1920) the response in the current density was similar to the first time. After the light was turned on, the current density changed again by about 0.08 mA/m^2 during 0.75 s and increased afterwards slightly by 1.7 mA/m^2 during 59 s. When the light was turned off the current density decreased by about 0.02 mA/m^2 during 0.75 s, stayed almost constant for about 40 s and decreased slowly.

5.3.3 ITO covered with plasmonic nanoparticles with Ferrocyanide solution

For the measurement shown in figure 5.4 the electrolyte was changed from sodium chloride, as in the other experiments presented above, to a solution of 0.1 M sodium sulfate and 1 mM potassium hexacyanoferrate(II)trihydrate ($K_4Fe(CN)_6$). In aqueous solution potassium ferrocyanide dissolves into the Ferrocyanide anion ($[Fe(CN)_6]^{4-}$) and is often used as

mediator in enzymatic sensors. It can be oxidized to ferricyanide $[\mathrm{Fe(CN)_6}]^{3-}$, according to the reaction $[\mathrm{Fe(CN)_6}]^{-3} + \mathrm{e}^- \rightleftarrows [\mathrm{Fe(CN)_6}]^{4-}$ with its standard state potential $E^{\ominus}$ at 360 mV against standard hydrogen electrode (SHE).
Ferrocyanide showed already a current increase at a potential of 60 mV when a voltage sweep was applied, in contrast to sodium chloride where a starting current increase could be noticed at about 200 mV. Also at the measurements presented in figure 5.4, a clear difference from the measurements with NaCl can be noticed.

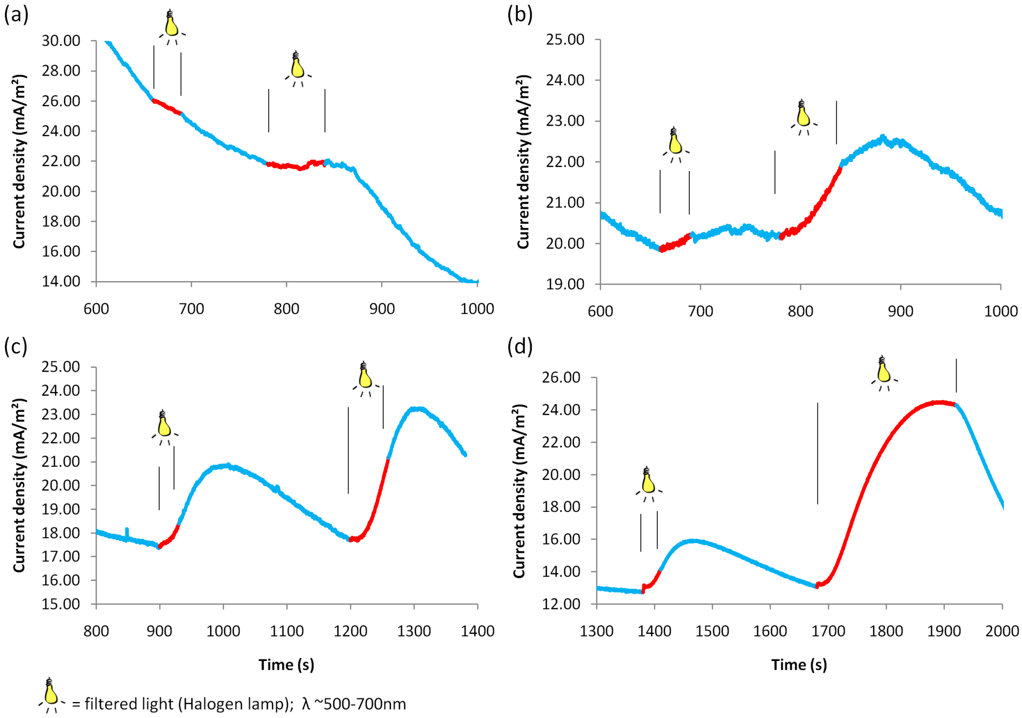

Figure 5.4: Recorded current density at constant applied potentials plotted as a function of time. The recorded current density when the light was turned on is indicated in a different color. In contrast to the other presented measurements the flow cell was filled with Ferrocyanide solution. The applied potential was (a) 0 mV, (b) 100 mV, (c) 150 mV and (d) 350 mV.

100 mV

While no current increase was noticed after the sample was radiated with halogen light at a fixed voltage of 0 mV (5.4a), already at a fixed voltage of 100 mV (5.4b) the current density started to increase noticeable when the light was turned on. The increase in current density at the first time the light was turned on was about 0.3 $\mathrm{mA/m^2}$ over 30 s and the second time an increase in the current density of roughly 1.7 $\mathrm{mA/m^2}$ over a time of 1 min could be measured from the recorded curves. Since the current density was still not stable when the light was turned on, the effective increase in current density was hard to measure. Also, the fast increase in the current density, right after the light was turned on, did not occur at this voltage level. This fast current density increase when the light was turned on, only started to become noticeable above an applied voltage of 350 mV as shown in figure 5.4d.

150 mV

In figure 5.4c the recorded current density change at an applied voltage of 150 mV is printed. Directly after the light was turned on no fast increase in the current density could be noticed. The current density increased slightly almost linear from 17.5 mA/m^2 by 0.95 mA/m^2 within a time of 30 s. At 150 mV, after the light was turned off, the current density still increased by another 2.38 mA/m^2 until it reached the peak value and started to decrease slowly by 2.86 mA/m^2 down to a current density of 17.9 mA/m^2. About 4 min after the light was turned off, the current density reached its initial state.

The second time while the light was turned on, the current density increased by 3.21 mA/m^2 until the Halogen light was turned off. Immediately after the light was turned off, the current decreased for 0.5 s and continued to increase for 30 s by 2.15 mA/m^2. The current density reached its peak at 23.1 mA/m^2. Afterwards, the current density decreased but the measurement was stopped before a stable value was reached.

350 mV

At an applied voltage of 350 mV (5.4d) the current density increased after the light was turned on within one second from 12.7 mA/m^2 by about 0.4 mA/m^2 and increased more slowly afterwards during a time of 29 s by 0.99 mA/m^2. When the light was turned off the current density still increased for another 47 s by about 1.73 mA/m^2 to decrease afterwards almost linearly down to 13.1 mA/m^2 which is again almost the same current density as the initial dark level.

The second time the light was turned on until the current density stopped to increase. Similar to the curve before again after the light was turned on the current density increased from 13 mA/m^2 by 0.17 mA/m^2 in a time of 0.35 s and slowly raised by 11.2 mA/m^2 to a maximum value of 24.4 mA/m^2. After this maximum value was reached the current density already started to decrease very slowly, even when the light was turned on and decreased much steeper than the first time. The current density decreased almost linearly by 6.5 mA/m^2 during 87 s before the recording was stopped.

5.3.4 ITO covered with plasmonic nanoparticles with constant flow

To further investigate the influence of a temperature increase due to light, the measurements shown in figure 5.5 were performed with a constant flow to eliminate the possible temperature increase of the whole flowcell. Basically, the increase in current density after the light was turned on followed the behavior of the experiment done without flow. The flow was always turned on a few seconds before the the light was shined onto the sample. Unless otherwise noted the flow rate was set to 3 ml/h.

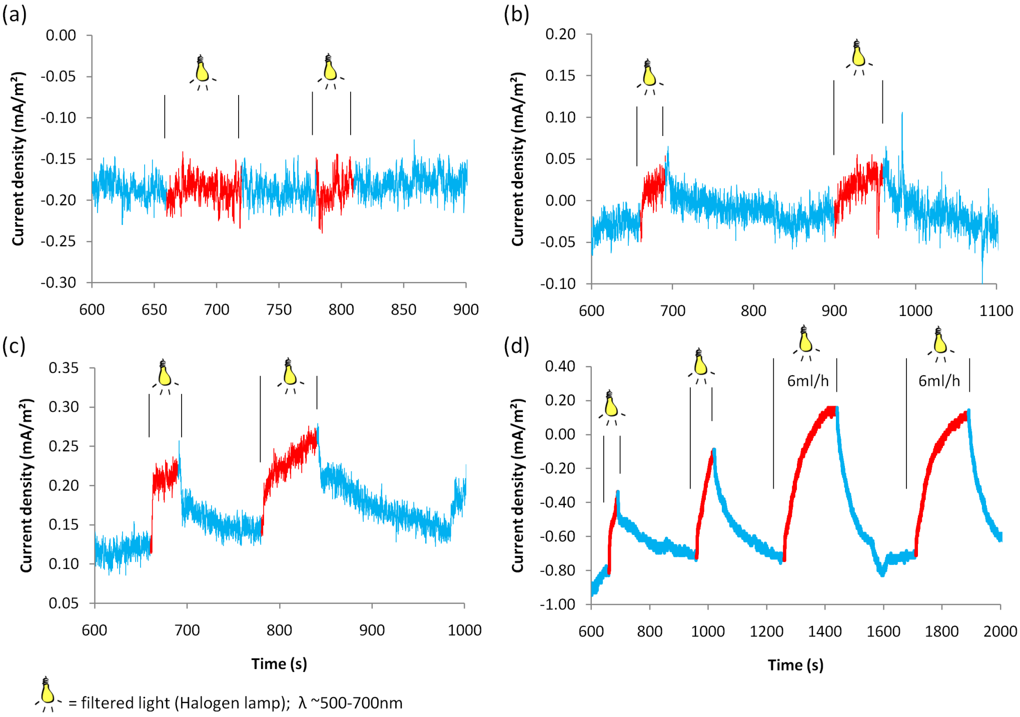

Figure 5.5: Recorded current density at constant applied potentials plotted as a function of time. The recorded current density when the light was turned on is indicated in a different color. Before the light was turned on, a constant flow was applied to exchange the solution during the measurement. The flow rate was set to 3 ml/h and 6 ml/h respectively in the last two times where the light was turned on in (d).The applied potential was (a) 100 mV, (b) 350 mV, (c) 500 mV and (d) 650 mV.

100 mV

At an applied voltage of 100 mV no change in current density could be noticed when the light was turned on as shown in figure 5.5a. But when the voltage level was increased to 350 mV (figure 5.5b) already a drift in the current density could be noticed.

350 mV

It was difficult to measure the effective increase in current density due to the unstable current density caused by the constant flow, but it was about 0.045 mA/m^2 within 30 s at

the first time the light was turned on.
At the second time light was emitted onto the sample the increase in current density was about 0.07 mA/m^2 in a time of 60 s. In both cases when the light was turned on, the current density did not show a noticeable fast increase at the beginning, which started to occur above a voltage level of 350 mV.

500 mV

At an applied voltage of 500 mV (figure 5.5c) the current density increased quickly by 0.07 mA/m^2 over a time of 1.2 s at the first (second 661.6 to 662.8) and 0.03 mA/m^2 over a time of 0.9 s at the second time (second 781.8 to 182.7) the light was switched on. With a constant flow the current density after the light was turned off decreased more slowly than it increased. During a time of 3.2 s the current density decreased by a value of 0.06 mA/m^2 at the first (second 691 to 694.2) and by 0.05 mA/m^2 during a time of 4.3 s at the second time (second 840 to 844.3) the light was switched off. After this faster decrease, the current density slowly drifted back nearly to the initial value before the light was turned on. While the sample was constantly irradiated with halogen light, the current density increased slowly at the first time by 0.03 mA/m^2 after a irradiation time of 28.2 s and at the second time the current density increased by 0.08 mA/m^2 at a irradiation time of 57.3 s.

650 mV

In figure 5.5d the recorded current density over time at an applied voltage of 650 mV is presented. The first time the light was turned on for 30 s. Again the current density increased fast right after the sample was radiated by light. Over a time of approximately 2.2 s the current density changed by 0.17 mA/m^2 and slightly increased later within a time of 27.5 s by a value of 0.29 mA/m^2. Similar to 5.5c, at which a voltage of 500 mV was applied, the current density decreased not as fast as it did at the experiments without constant flow, after the light was turned off. The current density decreased after the light was turned off by 0.1 mA/m^2 for 2.2 s and afterwards slightly decreased in 4.5 min down to 0.71 mA/m^2 which was about 0.1 mA/m^2 less than the current density before the light was turned on. This was almost the same current density as before the light was turned on (0.71 mA/m^2).
At the second time when the light was turned on, the change in current density was similar to the first one. The fast increase right after the light was turned on by 0.1 mA/m^2 for 1.3 s, a slower almost linear increase by 0.49 mA/m^2 during 57.8 s and after the light was turned off first a faster decrease by 0.06 mA/m^2 in the time of 2.3 s and a slight decrease in the time of 4 min down to 0.73 mA/m^2. Therefore the current density almost decreased to the same value before the light was turned on a second time.

In the last two cases the light was turned on, until a saturation in the current density increase could be noticed. Before the sample was radiated by light for the last time, the flow rate of the sodium chloride solution was increased up to 6 ml/h, which did not show any obvious difference in the current density increase. The current density increased again faster after the light was turned on by 0.07 mA/m^2 within 1.4 s at the third time, and by 0.04 mA/m^2 within 1.9 s at the fourth time the light was shined onto the sample. During the constant irradiation with the halogen light, the current density increased by 0.78 mA/m^2 slowly at the third time within 178.2 s and by 0.78 mA/m^2 at the fourth time within 178.4 s. When the light was turned off, no significant change in the speed of the current density decrease could be noticed. The current density decreased by -0.86 mA/m^2 after 170 s at the third time and at the fourth time by -0.83 mA/m^2 after 256.15 s. In both cases, the current density reached back to the initial value. After the light was turned off at the third time, the current density decreased by 0.86 mA/m^2 within 171 s going down to a current density of -0.73 mA/m^2, and at the fourth time by 0.83 mA/m^2 within 256 s to a value of -0.70 mA/m^2.
With the same sample and the same applied voltage level of 650 mV a control measurement without flow was conducted (data not shown). Basically it showed the same response to the light as the measurement with flow.

Two-electrode-system with Pt electrode

Not presented here are the experiments where the measurement was done in a two electrode system (the counter and reference electrode channel of the potentiostat were both connected to the platinum wire) to exclude the possibility that the Ag/AgCl becomes unstable under light. The results did not show any difference to the above presented measurements. Since the reference voltage changed (the platinum wire acts also as reference) the open circuit potential was measured at the mounted flow cell in a two (OCP of about 45 mV) as well as in a three electrode (OCP of about 295 mV) setup. The difference (-50 mV) was then used to adapt the applied jump in the potential (a jump to 0 mV in the three electrode setup corresponded to a jump to -250 mV).

Solid gold film on glass

In the last presented figures 5.6 a glass slide coated with a solid gold film was used instead of the ITO substrates as the working electrode. The measurement was meant as a control to see if the noticed current increase was mainly caused by a LSPR related effect. As shown in figure 5.6, the sample showed a similar response to the illumination as the ITO substrates covered with gold plasmonic nanoparticles.

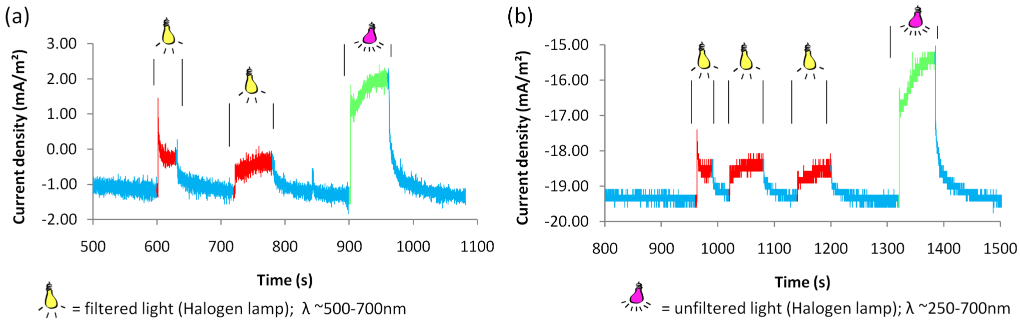

Figure 5.6: Recorded current density at constant applied potentials plotted as a function of time. The recorded current density when the light was turned on is indicated in a different color. In this measurements a glass slide coated with a solid gold film was used as working electrode. The applied potential was (a) 450 mV and (b) 500 mV. Before the light was turned on the last time, the UV-filter was removed at each applied voltage (a,b). This is indicated with green color.

450 mV

At an applied voltage of 450 mV (figure 5.6a) the current density increased by 2.6 mA/m^2 right after the light was turned on within 1.5 s. Then it decreased slightly in contrast to the second and third time the sample was illuminated where the current increased. During the illumination of 30 s the current density decreased by 1.7 mA/m^2. After the light was turned off, the current density decreased from -0.27 mA/m^2 down to -0.57 mA/m^2 (0.30 mA/m^2) within 0.7 s.

At the second illumination, the current density jumped by 0.69 mA/m^2 within 0.9 s and slightly increased within 60 s by 0.14 mA/m^2. When the light was turned off the current density decreased from -0.44 mA/m^2 down to -0.54 mA/m^2 (-0.10 mA/m^2) within 0.55 s. Before the light was turned on the third time (second 900 to 961), the UV-filter was removed. The current density jumped by 2.66 mA/m^2 within 2 s. Then it increased slightly by 0.62 mA/m^2 within 60 s and after the light was turned off the current density decreased from 1.94 mA/m^2 down to 0.81 mA/m^2 (-1.13 mA/m^2) within 0.9 s.

500 mV

At an applied voltage of 500 mV (figure 5.6b) the current density increased right after the light was turned on (second 963.25) by 2.03 mA/m^2 within 0.1 s. Similar to the behavior at an applied voltage of 450 mV, the current density decreased slightly in contrast to the following cases where the current density increased, while the sample was illuminated. The current density decreased by -1.01 mA/m^2 within 3.5 s and stayed constant for 26 s until the light was turned off. When the light was turned off the current density decreased by -0.51 mA/m^2 within 1.80 s.

At the second illumination, the current density increase right after the light was turned on was less than at the first time. The current density increased by 0.51 mA/m^2 within 0.95 s and increased slightly by 0.51 mA/m^2 within 59.45 s. After the light was turned off the current density decreased by -0.68 mA/m^2 within 0.75 s and after a decrease by -0.08 mA/m^2 within 4.3 s the initial value of -19 mA/m^2 was reached again.

At the third time the current density increased, right after the sample was illuminated, by 0.34 mA/m^2 within 0.59 s and later increased slightly by 0.51 mA/m^2 within 59.6 s. When the light was turned off, the current density decreased by -0.51 mA/m^2 within 1 s and reached the initial value of -19.25 mA/m^2 after 24.3 s and a decrease in the current density by -0.34 mA/m^2.

Before the light was turned on a fourth time, the UV-filter was removed again. After the light was turned on, the current density increased by 2.87 mA/m^2 within 0.75 s, slightly increased by 1.18 mA/m^2 within 42.2 s and stayed almost constant at a value of -15.54 mA/m^2 for another 20.3 s. When the light was turned off the current density decreased by -1.52 mA/m^2 within 1 s and after a decrease of -1.86 mA/m^2 within 24.3 s a stable value of -18.92 mA/m^2 was reached.

5.4 Discussion

To begin with, it has to be noted that a change in the speed of an ongoing surface reaction after the sample was irradiated by light could not directly be associated with the LSPR effect because the sample with a solid gold film onto a glass slide showed the same behavior as with plasmonic particles: current increase by light. At the same voltage level, the change in current density by light illumination was even higher for solid gold films than the sample with plasmonic nanoparticles.

In the following section it is tried to specify the effects which lead in their combination to the noticed increase of current density.

Influence of the semiconductor substrate

At the measurements done with bare ITO substrate an increase in current could only be measured after the UV-filter was removed. According to literature values for the band gap of ITO between 3.5 eV–4.3 eV, this increase is probably caused due to photoexcitation [91]. Since an increase in current density after illumination was measured with plasmonic particles and with solid gold films, although the UV-filter was present, the direct influence of the semiconductor could be excluded.

The localized electric field enhancement due to the LSPR of the attached gold nanoparticles, could influence the band transitions of ITO. But since the highest field enhancement is expected to be perpendicular to the propagation direction of the light and the recorded increase in the current density also occurred at the solid gold substrate, this effect was not further investigated.

Ferrocyanide solution

The measurement with Ferrocyanide solution showed interesting results. Even when the light was turned off, the current density still increased (figure 5.4). This behavior needs further investigation, since when the light is turned off, no additional energy is present and therefore the current density could at most stay constant at its level. Only restructuring of the surface layer could be found as a possible explanation so far.

Change in the ohmic resistance due to temperature increase

Temperature increase in the gold nanoparticles would lead to a change in resistance and therefore a change in the recorded current density. Compared to the total resistance of the electrochemical cell, the influence of gold is very small. As well as the positive temperature coefficient of gold would lead to an increase of resistance when the temperature is increased. Therefore the high positive increase in the current density can not be explained. The semiconducting properties of ITO would result in a decrease of resistance, but as already mentioned before at the measurement of bare ITO no direct influence was noted.

Local Temperature increase

In the field of medical research the high absorbing property of gold plasmonic nanoparticles at their resonance frequency has been used to thermally destroy cancer cells [92], [93]. Therefore a dissipation of the electromagnetic radiation into heat in the gold crystal needs also to be considered. Whereas more than 50 °C are not expected with halogen lamp illumination since in previous experiments, where DNA immobilized (~20base pairs) onto gold plasmonic nanoparticles was investigated, denaturation could not be recorded [64]. It also needs to be mentioned that in the referenced papers in contrast to this experiment much higher light intensities where used in the lower frequency range. In all experiments presented in this section an infrared filter was used which should also lower the temperature increase of the nanoparticles.

The local temperature increase at the surface could lead to a higher chemical reaction rate. According to transition state theory the rate constant can be written as

$$k = B\mathrm{e}^{\frac{-\Delta\overline{G}^{0^*}}{RT}} \tag{5.1}$$

where $\overline{G}^{0^*}$ is the activation Gibbs energy and B being a constant with the same dimensions as k. Furthermore, the current density can thus be written as

$$j = FB_{\mathrm{an.}}\mathrm{e}^{\frac{-\Delta\overline{G}^{0^*}_{\mathrm{an.}}}{RT}}\mathrm{e}^{\frac{(1-\alpha)\Delta\phi F}{RT}} - FB_{\mathrm{cat.}}\mathrm{e}^{\frac{-\Delta\overline{G}^{0^*}_{\mathrm{cat.}}}{RT}}\mathrm{e}^{\frac{-\alpha\Delta\phi F}{RT}} \tag{5.2}$$

where $\overline{G}^{0^*}$ is again the activation Gibbs energy for the cathodic and anodic electron transfer respectively, α the transfer coefficient and $\Delta\phi$ the potential difference between the bulk metal and the bulk solution, which is related with the overpotential by $\Delta\phi = E_{eq.} + \eta$. Hence an increase of the solution temperature in close vicinity of the gold nanoparticle would increase the current density. Since the relaxation of surface plasmon excitations is a non radiative process, damping is due to electron-electron, electron-phonon scattering, scattering at lattice defects *etc.* [73]. Phonon scattering would heat up the gold nanoparticle, explaining the increase of current density. Laser induced temperature increase of plasmonic gold nanoparticles, leading to an increase in the measured current could already be shown by L. B. Lowe *et al.* [94]. Although the volume of the nanoparticles used in the work of L. B. Lowe was less than the particle size used in this work, local temperature increase is the most proper explanation of the current increase considering that an increase in current density was also recorded on a solid gold film.

5.5 Conclusion

In this chapter, the results investigating an influence of the LSPR on electrochemical reactions have been presented. It was shown that the current density increased when the sample with attached gold plasmonic particles was illuminated. Since the increase in current density already occurred at a lower applied potential when the solution was exchanged with ferrocyanide, the increase could be directly related to an increased electrochemical reaction at the electrode. Furthermore an increase in current density was also recorded when conducting the same experiment with a solid gold film acting as working electrode. Therefore the measured increase in current density was explained by temperature increase of the gold due to the light, although it needs to be mentioned, that the reason for the increase in current density still needs further investigation.

Chapter 6

Summary

6.1 Electric Double Layer formation

In the presented experiments, the combination of cyclic voltammetry with localized surface plasmon resonance sensing showed a complementary information of electric double layer formation and chemical reaction. At low applied potentials, a linear response in the resonance shift was observed indicating a response to ion adsorption on the surface of the nanoparticles. The sensitivity of the LSPR signal to the surface layer could also be confirmed at a kinetic experiment. At lower salt concentrations the optical signal showed slower response when a small step potential was applied. Furthermore it could be shown that the observed increase in the localized surface plasmon peak width, as well as the decrease in absorption could not be explained by simple ion adsorption forming an electric double layer (Stern layer in combination with a diffusive layer). A possible explanation was given by introducing an electron depletion layer in the outer shell of the gold nanoparticles together with an ion layer at the surface.

Above a potential of 500mV, a hysteresis loop was noticed in the optical signal together with oxidation and reduction peaks in the cyclic voltammetry. The hysteresis response indicated a sensitivity of the optical signal to the surface species. Again the resonance dumping was explained by a change in the electron density at the interface layer due to a reversible ionic binding event.

At the oxidation potential of gold an irreversible response in the resonance peak shift was observed, which is most likely caused by dissolution and re-deposition of gold during the reduction process. SEM pictures recorded after the cycles confirmed the restructuring of the gold nanoparticles.

The simple setup of the localized surface plasmon system compared to other optical systems is, without question, a big advantage for future applications. During this work it has been shown that a combination of an electrochemical system with the optical system could improve the understanding of surface processes. Thinking of the complexity of certain biological membrane, the possibility to gain a local information about an ongoing process (by LSPR) together with an information about the involved species (by CV) would become a helpful and useful tool in future studies. Although it needs to be mentioned that the presented system is still not fully understood. With the help of the simulation the observed response could be better interpreted and further information in the interaction of the measured optical parameters could be gained. Whereas it needs to be mentioned that the classical description of the electron depletion layer might not be sufficient anymore and one should think of a quantum description of the material properties.

For further information more details on the ion adsorption and the EDL would be helpful. Surface enhanced Raman scattering could provide useful information on the gold halide and oxide formation. Furthermore impedance spectroscopy could lead to more information of the EDL-capacitance and thickness of the Stern layer.

6.2 Enhancement of chemical reaction by LSPR

In the second part of the work, it was shown that the current increased when the sample with immobilized plasmonic nanoparticles was illuminated with light. Taking into account other possible influences the current increase was most likely caused by an enhancement of surface reaction. Furthermore, after considering possible other influences, the observed increase in chemical reaction was explained by a local temperature increase. This was also confirmed by a measurement done on a solid gold film, since the recorded current density also increased under illumination.

Although an influence of the LSPR on the reaction enhancement could not be observed directly, the influence of LSPR can still not be excluded. The solid gold film needs to be characterized better, since the local temperature increase should intuitively be less, because of the increased volume of gold. At both samples a mapping of the temperature increase would bring helpful information.

For further investigation of the LSPR influence the illumination should also be changed from white light to laser light. This would allow to illuminate the sample directly with the resonance frequency of the particles and as a control also illumination out of the resonance frequency would be possible. Additionally a direct observation of the light intensity of certain wavelengths would become possible, allowing to investigate the influence of eventually occurring photoexcitation processes (linear increase with light intensity). Furthermore a more detailed theoretical model on the electron transfer process is needed to be able to calculate absolute values of the current density increase due to the temperature.

Increased electron-phonon scattering should also have an influence on the resonance damping. Therefore continuous spectra measurements of a sample illuminated with two different intensities should be conducted.

Bibliography

[1] Thews, G., Lang, F. & Schmidt, R. F. *Physiologie des Menschen* (Springer, Berlin, 2000). 1, 3

[2] Fraden, J. *Handbook of modern sensors : physics, designs, and applications* (Springer / AIP Press, New York, 2004), 3rd edn. 1, 2, 3

[3] Fernicola, V. C. *et al.* Investigations on exponential lifetime measurements for fluorescence thermometry. *Review of Scientific Instruments* **71**, 2938–2943 (2000). URL `http://link.aip.org/link/?RSI/71/2938/1`. 2

[4] Trah, H.-P., Suzuki, Y., Yokomori, I. & Marek, J. *Sensors for automotive applications*, vol. 4 of *Sensors applications* (Wiley-VCH, Weinheim, 2003). 2

[5] Alberts, B. *et al. Molecular Biology of the Cell* (Garland Science, 2002), 4th edn. 3

[6] McNaught, A. D. & Wilkinson, A. *IUPAC, Compendium of Chemical Terminology (the "Gold Book")* (Blackwell Scientific Publications, Oxford, 1997), 2nd edn. 4

[7] Zourob, M. (ed.) *Recognition Receptors in Biosensors* (Springer, 2010). 4, 6

[8] Borisov, S. M. & Wolfbeis, O. S. Optical Biosensors. *Chemical Reviews* **108**, 423–461 (2008). URL `http://dx.doi.org/10.1021/cr068105t`. 4

[9] Moerner, W. E. New directions in single-molecule imaging and analysis. *Proceedings of the National Academy of Sciences* **104**, 12596–12602 (2007). URL `http://www.pnas.org/content/104/31/12596.abstract`. 4, 8

[10] Manuel, M. *et al.* Determination of probable alcohol yield in musts by means of an SPR optical sensor. *Sensors and Actuators B: Chemical* **11**, 455 – 459 (1993). URL `http://www.sciencedirect.com/science/article/B6THH-44B6SFG-JB/2/b183109328500e6332caf2f040ea4c0f`. 5

[11] Dostálek, J. *et al.* Surface plasmon resonance biosensor based on integrated optical waveguide. *Sensors and Actuators B: Chemical* **76**, 8 – 12 (2001).

URL http://www.sciencedirect.com/science/article/B6THH-43556PR-2/2/3575e8883284d25080c2b497b9f9530b. 5

[12] Mouvet, C. *et al.* Determination of simazine in water samples by waveguide surface plasmon resonance. *Analytica Chimica Acta* **338**, 109 – 117 (1997). URL http://www.sciencedirect.com/science/article/B6TF4-3S9MBXF-F/2/c2c8929c50dae9dd37423bc2a30bafb2. 5

[13] Feijter, J. A. D., Benjamins, J. & Veer, F. A. Ellipsometry as a tool to study the adsorption behavior of synthetic and biopolymers at the air-water interface. *Biopolymers* **17**, 1759–1772 (1978). URL http://dx.doi.org/10.1002/bip.1978.360170711. 5

[14] Vörös, J. *et al.* Optical grating coupler biosensors. *Biomaterials* **23**, 3699 – 3710 (2002). URL http://www.sciencedirect.com/science/article/B6TWB-45JPG0B-2/2/55801406361cf2883135c192be7a0f2c. 5

[15] Fan, X. *et al.* Sensitive optical biosensors for unlabeled targets: A review. *Analytica Chimica Acta* **620**, 8 – 26 (2008). URL http://www.sciencedirect.com/science/article/B6TF4-4SJ2WV7-1/2/b631bf29724d89506db27aaac298026a. 5, 12

[16] Bornhop, D. J. *et al.* Free-Solution, Label-Free Molecular Interactions Studied by Back-Scattering Interferometry. *Science* **317**, 1732–1736 (2007). URL http://www.sciencemag.org/cgi/content/abstract/317/5845/1732. 5

[17] Armani, A. M., Kulkarni, R. P., Fraser, S. E., Flagan, R. C. & Vahala, K. J. Label-Free, Single-Molecule Detection with Optical Microcavities. *Science* **317**, 783–787 (2007). URL http://www.sciencemag.org/cgi/content/abstract/317/5839/783. 5

[18] Zoski, C. G. *Handbook of Electrochemistry* (Elsevier Science, Amsterdam, 2007), 1st edn. 6, 7

[19] Bakker, E. & Pretsch, E. Potentiometric sensors for trace-level analysis. *TrAC Trends in Analytical Chemistry* **24**, 199 – 207 (2005). URL http://www.sciencedirect.com/science/article/B6V5H-4FDMYP7-7/2/62103c3d210523c570084abe62470afc. 7

[20] D'Orazio, P. Biosensors in clinical chemistry. *Clinica Chimica Acta* **334**, 41 – 69 (2003). URL http://www.sciencedirect.com/science/article/B6T57-491PW75-3/2/2911a37c4f44dfb2e6dfd2ef455c8776. 7

[21] Bard, A. J. & Faulkner, L. R. *Electrochemical Methods: Fundamentals and Applications* (John Wiley & Sons, 2000), 2nd edn. 8

[22] Miklos, G. L. G. & Maleszka, R. Protein functions and biological contexts. *Proteomics* **1**, 169–178 (2001). URL `http://dx.doi.org/10.1002/1615-9861(200102)1:2<169::AID-PROT169>3.0.CO;2-C`. 8

[23] Lee, H. J., Wark, A. W. & Corn, R. M. Microarray methods for protein biomarker detection. *The Analyst* **133**, 975–983 (2008). URL `http://dx.doi.org/10.1039/b717527b`. 8

[24] Venkatasubbarao, S. Microarrays - status and prospects. *Trends in Biotechnology* **22**, 630 – 637 (2004). URL `http://www.sciencedirect.com/science/article/B6TCW-4DPC6P0-5/2/b37dbb8497d6ca490584aaca72e245db`. 8

[25] Kambhampati, D. *Protein Microarray Technology* (Wiley-VCH, Weinheim, 2004), 1st edn. 8

[26] Wulfkuhle, J. D., Liotta, L. A. & Petricoin, E. F. Proteomic applications for the early detection of cancer. *Nature Reviews Cancer* **3**, 267–275 (2003). URL `http://dx.doi.org/10.1038/nrc1043`. 8

[27] Phizicky, E., Bastiaens, P. I. H., Zhu, H., Snyder, M. & Fields, S. Protein analysis on a proteomic scale. *Nature* **422**, 208–215 (2003). URL `http://dx.doi.org/10.1038/nature01512`. 8

[28] Cooper, M. A. Optical biosensors in drug discovery. *Nature Reviews Drug Discovery* **1**, 515–528 (2002). URL `http://dx.doi.org/10.1038/nrd838`. 8

[29] Volle, J. N. *et al.* Enhanced sensitivity detection of protein immobilization by fluorescent interference on oxidized silicon. *Biosensors and Bioelectronics* **19**, 457 – 464 (2003). URL `http://www.sciencedirect.com/science/article/B6TFC-4967FXF-2/2/6f8f6ff3cf379588ac716a5dd325be26`. 8

[30] Bras, M. *et al.* Optimisation of a silicon/silicon dioxide substrate for a fluorescence DNA microarray. *Biosensors and Bioelectronics* **20**, 797 – 806 (2004). URL `http://www.sciencedirect.com/science/article/B6TFC-4C8NKC4-4/2/7233a45611984b1ee91b5e7bdc8b2c74`. Microarrays for Biodefense and Environmental Applications. 8

[31] Schultz, D. A. Plasmon resonant particles for biological detection. *Current Opinion in Biotechnology* **14**, 13 – 22 (2003). URL `http://www.sciencedirect.com/science/article/B6VRV-47NFBJN-3/2/02c60b3eb3f5152a41f17021df880011`. 9

[32] Anker, J. N. *et al.* Biosensing with plasmonic nanosensors. *Nature Materials* **7**, 442–453 (2008). URL `http://dx.doi.org/10.1038/nmat2162`. 9, 37

[33] Giacomini, K. M., Huang, S.-M., Tweedie, D. J. & Benet, L. Z. Membrane transporters in drug development. *Nature Reviews Drug Discovery* **9**, 215–236 (2010). URL `http://dx.doi.org/10.1038/nrd3028`. 9

[34] Bohm, D. & Pines, D. A Collective Description of Electron Interactions: III. Coulomb Interactions in a Degenerate Electron Gas. *Physical Review* **92**, 609–625 (1953). 11

[35] Ritchie, R. H. Plasma Losses by Fast Electrons in Thin Films. *Physical Review* **106**, 874–881 (1957). 12

[36] Maier, S. A. *Plasmonics: Fundamentals and applications* (Springer, 2007), 1st edn. 12

[37] Stern, E. A. & Ferrell, R. A. Surface plasma oscillations of a degenerate electron gas. *Physical Review* **120**, 130–136 (1960). 12

[38] Born, M. *Optik* (Springer, Berlin, Heidelberg, 1972), 3rd edn. 12

[39] Stratton, J. A. *Electromagnetic Theory* (McGraw-Hill, New York, 1941), 1st edn. 12

[40] Novotny, L. & Hecht, B. *Principles of Nano-Optics* (Cambridge University Press, Cambridge, 2006), 1st edn. 13

[41] Johnson, P. B. & Christy, R. W. Optical Constants of the Noble Metals. *Physical Review B* **6**, 4370–4379 (1972). 15, 39

[42] Kreibig, U., Schmitz, B. & Breuer, H. D. Separation of plasmon-polariton modes of small metal particles. *Physical Review B* **36**, 5027–5030 (1987). 14

[43] Willets, K. A. & Van Duyne, R. P. Localized Surface Plasmon Resonance Spectroscopy and Sensing. *Annual Review of Physical Chemistry* **58**, 267–297 (2007). URL `http://arjournals.annualreviews.org/doi/abs/10.1146/annurev.physchem.58.032806.104607`. 15

[44] Haynes, C. L., Haes, A. J., McFarland, A. D. & Duyne, R. P. Nanoparticles with Tunable Localized Surface Plasmon Resonances. *Radiative Decay Engineering* 47–99 (2005). URL `http://dx.doi.org/10.1007/0-387-27617-3_3`. 15, 43

[45] Nehl, C. L. & Hafner, J. H. Shape-dependent plasmon resonances of gold nanoparticles. *Journal of Materials Chemistry* **18**, 2415–2419 (2008). URL `http://dx.doi.org/10.1039/b714950f`. 15, 43

[46] Jung, L. S., Campbell, C. T., Chinowsky, T. M., Mar, M. N. & Yee, S. S. Quantitative Interpretation of the Response of Surface Plasmon Resonance Sensors to Adsorbed Films. *Langmuir* **14**, 5636–5648 (1998). URL `http://pubs.acs.org/doi/abs/10.1021/la971228b`. `http://pubs.acs.org/doi/pdf/10.1021/la971228b`. 15

[47] Haes, A. J. & Van Duyne, R. P. A unified view of propagating and localized surface plasmon resonance biosensors. *Analytical and Bioanalytical Chemistry* **379**, 920–930 (2004). URL `http://dx.doi.org/10.1007/s00216-004-2708-9`. 15

[48] Haes, A. J. & Van Duyne, R. P. A Nanoscale Optical Biosensor: Sensitivity and Selectivity of an Approach Based on the Localized Surface Plasmon Resonance Spectroscopy of Triangular Silver Nanoparticles. *Journal of the American Chemical Society* **124**, 10596–10604 (2002). URL `http://dx.doi.org/10.1021/ja020393x`. 15

[49] Auerbach, D. (ed.) *Nonaqueous Electrochemistry* (Marcel Dekker, Inc., New York, Basel, 1999). 16

[50] Bockris, J. O. & Reddy, A. K. N. *Ionics*, vol. 1 of *Modern Electrochemistry* (Plenum Press, 1998), 2nd edn. 16

[51] Bagotsky, V. S. *Fundamentals of Electrochemistry* (Wiley-Intersciene, 2005), 2nd edn. 16

[52] Israelachvili, J. *Intermolecular & Surface Forces* (Academic Press, London, 1998). 17

[53] Golovnev, A. & Trimper, S. Exact solution of the Poisson–Nernst–Planck equations in the linear regime. *The Journal of Chemical Physics* **131**, 114903 (2009). URL `http://link.aip.org/link/?JCP/131/114903/1`. 17

[54] Biesheuvel, P., van Soestbergen, M. & Bazant, M. Imposed currents in galvanic cells. *Electrochimica Acta* **54**, 4857 – 4871 (2009). URL `http://www.sciencedirect.com/science/article/B6TG0-4W15KVM-H/2/c15c7d924a008b3a45220e177e71c9c5`. 17

[55] Torrie, G. M. & Valleau, J. P. A Monte Carlo study of an electrical double layer. *Chemical Physics Letters* **65**, 343 – 346 (1979). URL `http://www.sciencedirect.com/science/article/B6TFN-44FDDNH-DS/2/6b837f97f546b65f72a28bc089ce8d97`. 17

[56] Bard, A. J., Stratmann, M. & Unwin, P. R. (eds.) *Instrumentation and Electroanalytical Chemistry*, vol. 3 of *Encyclopedia of Electrochemistry* (Wiley-VCH, Weinheim, 2003). 19

[57] Bockris, J. O., Reddy, K. N., Amulya & Gamboa-Aldeco, M. *Fundamentals of Electrodics*, vol. 2A of *Modern Electrochemistry* (Kluwer Academic, Plenum Publishers, New York, 2000), 2nd edn. 19, 20

[58] Marcus, R. A. Electron transfer reactions in chemistry. Theory and experiment. *Reviews of Modern Physics* **65**, 599–610 (1993). URL `http://link.aps.org/doi/10.1103/RevModPhys.65.599`. 20

[59] Kuznetsov, A. M. *Charge Transfer in Physics, Chemistry and Biology: Physical Mechanisms of Elementary Processes and an Introduction to the Theory* (Gordon and Breach Publishers, 1995). 20

[60] Sun, J., Velamakanni, B. V., Gerberich, W. W. & Francis, L. F. Aqueous latex/ceramic nanoparticle dispersions: colloidal stability and coating properties. *Journal of Colloid and Interface Science* **280**, 387 – 399 (2004). URL `http://www.sciencedirect.com/science/article/B6WHR-4DB57NT-5/2/3822d5a6c725ba4bccda1be427f1410d`. 23

[61] Fang, A., Ng, H., Su, X. & Li, S. F. Y. Soft-Lithography-Mediated Submicrometer Patterning of Self-Assembled Monolayer of Hemoglobin on ITO Surfaces. *Langmuir* **16**, 5221–5226 (2000). URL `http://pubs.acs.org/doi/abs/10.1021/la991574o`. `http://pubs.acs.org/doi/pdf/10.1021/la991574o`. 23

[62] Kim, J. S. *et al.* X-ray photoelectron spectroscopy of surface-treated indium-tin oxide thin films. *Chemical Physics Letters* **315**, 307 – 312 (1999). URL `http://www.sciencedirect.com/science/article/B6TFN-3Y9G7P8-1/2/91831d53669dcca2bf2160245c9c708f`. 23

[63] Murthy, V. S., Cha, J. N., Stucky, G. D. & Wong, M. S. Charge-Driven Flocculation of Poly(l-lysine)Gold Nanoparticle Assemblies Leading to Hollow Microspheres. *Journal of the American Chemical Society* **126**, 5292–5299 (2004). URL `http://pubs.acs.org/doi/abs/10.1021/ja038953v`. 23

[64] Sannomiya, T. *Optical BioSensing Based on Localized Surface Plasmon Resonance: Experiments & Simulations*. Ph.D. thesis, ETH Zürich (2009). 27, 59

[65] Jiang, X. *et al.* Electrochemical surface plasmon resonance studies on the deposition of the charge-transfer complex from electrooxidation of o-tolidine and effects of dermatan sulfate. *Electrochemistry Communications* **10**, 1235 – 1237 (2008). URL `http://www.sciencedirect.com/science/article/B6VP5-4SSY91Y-1/2/cdaa0ffcd182f398977074a67fd3cda4`. 28

[66] Zhang, N., Schweiss, R., Zong, Y. & Knoll, W. Electrochemical surface plasmon spectroscopy–Recent developments and applications. *Electrochimica Acta* **52**, 2869 – 2875 (2007). URL `http://www.sciencedirect.com/science/article/B6TG0-4MFTVSN-4/2/4f5b15c913900b1d0bdac2ed2b9b12c5`. 28

[67] Sardar, R., Funston, A. M., Mulvaney, P. & Murray, R. W. Gold Nanoparticles: Past, Present, and Future. *Langmuir* **25**, 13840–13851 (2009). URL `http://dx.doi.org/10.1021/la9019475`. 28

[68] Miyazaki, T. *et al.* Electrical Control of Plasmon Resonance of Gold Nanoparticles Using Electrochemical Oxidation. *The Journal of Physical Chemistry C* **113**, 8484–8490 (2009). URL `http://dx.doi.org/10.1021/jp901408w`. 28

[69] Leroux, Y. *et al.* Tunable Electrochemical Switch of the Optical Properties of Metallic Nanoparticles. *ACS Nano* **2**, 728–732 (2008). URL `http://dx.doi.org/10.1021/nn700438a`. 28

[70] Novo, C., Funston, A. M., Gooding, A. K. & Mulvaney, P. Electrochemical Charging of Single Gold Nanorods. *Journal of the American Chemical Society* **131**, 14664–14666 (2009). URL `http://dx.doi.org/10.1021/ja905216h`. 28

[71] Stankowski, S. & Ramsden, J. J. Voltage-dependent coupling of light into ITO-covered waveguides. *Journal of Physics D: Applied Physics* **35**, 299–302 (2002). URL `http://stacks.iop.org/0022-3727/35/i=4/a=304`. 28

[72] Ung, T., Giersig, M., Dunstan, D. & Mulvaney, P. Spectroelectrochemistry of Colloidal Silver. *Langmuir* **13**, 1773–1782 (1997). URL `http://dx.doi.org/10.1021/la960863z`. 28

[73] Kreibig, U., Vollmer, M. & Toennies, P. *Optical Properties of Metal Clusters*, vol. 25 of *Springer Series in Materials Science* (Springer, Berlin, Heidelberg, 2010). 30, 40, 60

[74] Bazant, M. Z., Thornton, K. & Ajdari, A. Diffuse-charge dynamics in electrochemical systems. *Physical Review E* **70**, 021506– (2004). URL `http://link.aps.org/doi/10.1103/PhysRevE.70.021506`. 37

[75] Sannomiya, T., Hafner, C. & Vörös, J. Strain mapping with optically coupled plasmonic particles embedded in a flexible substrate. *Optics Letters* **34**, 2009–2011 (2009). URL `http://ol.osa.org/abstract.cfm?URI=ol-34-13-2009`. 37

[76] Butt, H. J., Graf, K. & Kappl, M. *Physics and Chemistry of Interfaces* (Wiley-VCH, Weinheim, 2003). 37

[77] Sannomiya, T., Dermutz, H., Hafner, C., Vörös, J. & Dahlin, A. B. Electrochemistry on a Localized Surface Plasmon Resonance Sensor. *Langmuir* **26**, 7619–7626 (2010). URL `http://pubs.acs.org/doi/abs/10.1021/la9042342`. `http://pubs.acs.org/doi/pdf/10.1021/la9042342`. 37

[78] Xia, S. J. & Birss, V. I. A multi-technique study of compact and hydrous Au oxide growth in 0.1 M sulfuric acid solutions. *Journal of Electroanalytical Chemistry* **500**, 562 – 573 (2001). URL `http://www.sciencedirect.com/science/article/B6TGB-42HXG5H-25/2/de55b6331825ee630cc8d2a599d868c8`. 38, 40

[79] Kordes, E. Direkte Berechnung der Ionenradien in Alkalihalogeniden aus der Lichtbrechung bzw. Molrefraktion und dem Ionenabstand. *Mineralogy and Petrology* **8**, 13–23 (1962). URL `http://dx.doi.org/10.1007/BF01128389`. 38, 78, 79

[80] Mulvaney, P. Surface Plasmon Spectroscopy of Nanosized Metal Particles. *Langmuir* **12**, 788–800 (1996). URL `http://pubs.acs.org/doi/abs/10.1021/la9502711`. `http://pubs.acs.org/doi/pdf/10.1021/la9502711`. 39, 40

[81] Etchegoin, P. G., Ru, E. C. L. & Meyer, M. An analytic model for the optical properties of gold. *The Journal of Chemical Physics* **125**, 164705 (2006). URL `http://link.aip.org/link/?JCP/125/164705/1`. 39

[82] Horkans, J., Cahan, B. & Yeager, E. Electrode potential scanning ellipsometric spectroscopy: Study of the formation of the anodic oxide film on noble metals. *Surface Science* **46**, 1 – 23 (1974). URL `http://www.sciencedirect.com/science/article/B6TVX-46SXKKF-JR/2/6187590ad74e9240caedf7b8ee96c57a`. 40, 43

[83] Hu, Z. & Ritzdorf, T. Cyanide- and Thiourea-Free Electrochemical Etching of Gold for Microelectronics Applications. *Journal of The Electrochemical Society* **154**, D543–D549 (2007). URL `http://link.aip.org/link/?JES/154/D543/1`. 42

[84] Falk, A. L. *et al.* Near-field electrical detection of optical plasmons and single-plasmon sources. *Nature Physics* **5**, 475–479 (2009). URL `http://dx.doi.org/10.1038/nphys1284`. 46

[85] Brolo, A. G., Irish, D. E. & Smith, B. D. Applications of surface enhanced Raman scattering to the study of metal-adsorbate interactions. *Journal of Molecular Structure* **405**, 29 – 44 (1997). URL `http://www.sciencedirect.com/science/article/B6TGS-3S9K0K2-25/2/1710cfdef5206aef12d9412878e0f8eb`. 46

[86] Jeanmaire, D. L. & Duyne, R. P. V. Surface raman spectroelectrochemistry: Part I. Heterocyclic, aromatic, and aliphatic amines adsorbed on the anodized silver electrode. *Journal of Electroanalytical Chemistry* **84**, 1 – 20 (1977). URL `http://www.sciencedirect.com/science/article/B6TGB-4K7KHS0-2/2/a20190416a0b038565c326fed3ce49af`. 46

[87] Yanagisawa, H. *et al.* Laser-induced field emission from a tungsten tip: Optical control of emission sites and the emission process. *Physical Review B* **81**, 115429– (2010). URL `http://link.aps.org/doi/10.1103/PhysRevB.81.115429`. 46

[88] Nakanishi, H. *et al.* Photoconductance and inverse photoconductance in films of functionalized metal nanoparticles. *Nature* **460**, 371–375 (2009). URL `http://dx.doi.org/10.1038/nature08131`. 46

[89] Du, L. *et al.* Plasmon-Induced Charge Separation and Recombination Dynamics in Gold–TiO_2 Nanoparticle Systems: Dependence on TiO_2 Particle Size. *The Journal of Physical Chemistry C* **113**, 6454–6462 (2009). URL `http://dx.doi.org/10.1021/jp810576s`. 46

[90] Tian, Y., Wang, X., Zhang, D., Shi, X. & Wang, S. Effects of electron donors on the performance of plasmon-induced photovoltaic cell. *Journal of Photochemistry and Photobiology A: Chemistry* **199**, 224 – 229 (2008). URL `http://www.sciencedirect.com/science/article/B6TGY-4STB0FP-1/2/9c957ac48de389c11ac2a6b650212855`. 46

[91] Balasubramanian, N. & Subrahmanyam, A. Electrical and optical properties of reactively evaporated indium tin oxide (ITO) films-dependence on substrate temperature and tin concentration. *Journal of Physics D: Applied Physics* **22**, 206–209 (1989). 58

[92] El-Sayed, I. H., Huang, X. & El-Sayed, M. A. Selective laser photo-thermal therapy of epithelial carcinoma using anti-EGFR antibody conjugated gold nanoparticles. *Cancer Letters* **239**, 129 – 135 (2006). URL `http://www.sciencedirect.com/science/article/B6T54-4H6PKX0-1/2/01bb371832529939d40849f76e12aeda`. 59

[93] Huang, X., Jain, P. K., El-Sayed, I. H. & El-Sayed, M. A. Determination of the Minimum Temperature Required for Selective Photothermal Destruction of Cancer Cells with the Use of Immunotargeted Gold Nanoparticles. *Photochemistry and Photobiology* **82**, 412–417 (2006). URL `http://dx.doi.org/10.1562/2005-12-14-RA-754`. 59

[94] Lowe, L. B. *et al.* Laser-Induced Temperature Jump Electrochemistry on Gold Nanoparticle-Coated Electrodes. *Journal of the American Chemical Society* **125**, 14258–14259 (2003). URL `http://dx.doi.org/10.1021/ja036672h`. 60

[95] Morse, P. M. & Feshbach, H. *Methods of theoretical physics*, vol. Part II (Feshbach Publishing, LLC, Minneapolis, 1953,1981). 73

[96] Abramowitz, M. & Stegun, I. A. *Handbook of Mathematical Functions* (Dover Publications Inc., 1965). 74

[97] Lide, D. R. (ed.) *CRC Handbook of Chemistry and Physics* (CRC Press, 2008), 89th edn. 79

Appendices

Appendix A

Overview of the Mie Scattering

Scattering by a round particle in an isotrope media is accurately described by the concept of classical electrodynamics. Starting with the Maxwell's wave equations in free space (source free $\rho = 0$, $\boldsymbol{J} = 0$)

$$\nabla^2 \times \boldsymbol{E} = \epsilon_0 \mu_0 \frac{\partial^2 \boldsymbol{H}}{\partial t^2} \tag{A.1a}$$

$$\nabla^2 \times \boldsymbol{H} = \epsilon_0 \mu_0 \frac{\partial^2 \boldsymbol{E}}{\partial t^2} \tag{A.1b}$$

Now in all generality, an harmonic time dependence of the electric and magnetic field is assumed ($\boldsymbol{E}(\boldsymbol{r}, t) = \Re\left\{\underline{\boldsymbol{E}}(\boldsymbol{r}) e^{-\mathrm{j}\omega t}\right\}$, $\boldsymbol{H}(\boldsymbol{r}, t) = \Re\left\{\underline{\boldsymbol{H}}(\boldsymbol{r}) e^{-\mathrm{j}\omega t}\right\}$). After inserting this in (A.1a) and (A.1b) this leads to the electromagnetic wave equations for time-harmonic fields:

$$\nabla^2 \times \boldsymbol{E} - k^2 \boldsymbol{E} = 0 \tag{A.2a}$$

$$\nabla^2 \times \boldsymbol{H} - k^2 \boldsymbol{H} = 0, \tag{A.2b}$$

$k = \omega \sqrt{\mu_0 \epsilon_0}$ being the wavenumber. Since a planar wave is scattered at a spherical particle, the solution of (A.2a) in spherical coordinates is of interest. Therefore one can define the three vector spherical harmonics according to Morse and Feshbach [95], which express a vector field in terms of component scalar fields bearing a simple relationship to the boundary surface:

$$\boldsymbol{V}^{(1)}_{mn}(\theta, \phi) = \boldsymbol{P}_{mn}(\theta, \phi) = \hat{r} Y^m_n(\theta, \phi) \qquad (n = 0, 1, 2, \dots) \tag{A.3a}$$

$$\begin{aligned} \boldsymbol{V}^{(2)}_{mn}(\theta, \phi) &= \boldsymbol{B}_{mn}(\theta, \phi) = r \nabla \left[Y^m_n(\theta, \phi) \right] \qquad (n = 1, 2, 3, \dots) \\ &= \left[\hat{\theta} \frac{\mathrm{d}}{\mathrm{d}\theta} P^m_n(\cos(\theta)) + \hat{\phi} \frac{\mathrm{j}m}{\sin(\theta)} P^m_n(\cos(\theta)) \right] \mathrm{e}^{\mathrm{j}m\phi} \end{aligned} \tag{A.3b}$$

$$\begin{aligned} \boldsymbol{V}^{(2)}_{mn}(\theta, \phi) &= \boldsymbol{C}_{mn}(\theta, \phi) = \nabla \times \left[\boldsymbol{r} Y^m_n(\theta, \phi) \right] \qquad (n = 1, 2, 3, \dots) \\ &= \left[\hat{\theta} \frac{\mathrm{j}m}{\sin(\theta)} P^m_n(\cos(\theta)) - \hat{\phi} \frac{\mathrm{d}}{\mathrm{d}\theta} P^m_n(\cos(\theta)) \right] \mathrm{e}^{\mathrm{j}m\phi} \end{aligned} \tag{A.3c}$$

Where $Y_n^m(\theta,\phi)$ are the complex scalar spherical harmonics $Y_n^m(\theta,\phi) = \mathrm{e}^{\mathrm{j}m\theta} P_n^m(\cos(\phi))$ and $P_n^m(x)$ the associated Legendre function [96]. The three regular vector spherical waves $Rg\boldsymbol{L}_{mn}$, $Rg\boldsymbol{M}_{mn}$, $Rg\boldsymbol{N}_{mn}$ can then be defined as

$$\begin{aligned} Rg\boldsymbol{L}_{mn}(kr,\theta,\phi) &= \frac{\gamma'_{mn}}{k}\nabla\left[Rg\psi_{mn}(kr,\theta,\phi)\right] \\ &= \gamma'_{mn}\left[\boldsymbol{P}_{mn}(\theta,\phi)\frac{\mathrm{d}j_n(kr)}{\mathrm{d}r} + \boldsymbol{B}_{mn}(\theta,\phi)\frac{j_n(kr)}{kr}\right] \end{aligned} \tag{A.4a}$$

$$\begin{aligned} Rg\boldsymbol{M}_{mn}(kr,\theta,\phi) &= \gamma_{mn}\nabla\times\left[\boldsymbol{r}Rg\psi_{mn}(kr,\theta,\phi)\right] \\ &= \gamma_{mn} j_n(kr)\boldsymbol{C}_{mn}(\theta,\phi) \end{aligned} \tag{A.4b}$$

$$\begin{aligned} Rg\boldsymbol{N}_{mn}(kr,\theta,\phi) &= \frac{1}{k}\nabla\times Rg\boldsymbol{M}_{mn}(kr,\theta,\phi) \\ &= \gamma_{mn}\left\{\boldsymbol{P}_{mn}(\theta,\phi)\frac{n(n+1)j_n(kr)}{kr} + \boldsymbol{B}_{mn}(\theta,\phi)\frac{1}{kr}\frac{\mathrm{d}[krj_n(kr)]}{\mathrm{d}r}\right\} \end{aligned} \tag{A.4c}$$

where Rg stands for regular, indicating the three sets of solutions of the first kind being finite at $r = 0$. By replacing the spherical Bessel function $j_n(kr)$ by the spherical Hankel function $h_n = j_n(kr) + \mathrm{j}n_n(kr)$, where $n_n(kr)$ stands for the spherical Neumann function, one gets the sets of solutions for the outgoing waves. In equation (A.4a) through (A.4c) $\gamma'_{mn} = \sqrt{\frac{(2n+1)(n-m)!}{4\pi(n+m)!}}$ and $\gamma_{mn} = \sqrt{\frac{(2n+1)(n-m)!}{4\pi n(n+1)(n+m)!}}$. $Rg\psi$ is are the scalar functions being a solution of the Helmholtz wave equation $\nabla^2\psi + k^2\psi = 0$. Furthermore the general solutions can be constructed by integrating the vector spherical harmonics over all possible directions. The vector spherical wave functions can be expressed as integral representations of the vector spherical harmonics

$$Rg\boldsymbol{L}_{mn}(kr,\theta,\phi) = \frac{(-\mathrm{j})^{n-1}}{4\pi}\gamma'_{mn}\int_{4\pi}\mathrm{d}\Omega'\mathrm{e}^{\mathrm{j}kr\hat{r}\hat{r}'}\boldsymbol{P}_{mn}(\theta',\phi') \tag{A.5a}$$

$$Rg\boldsymbol{M}_{mn}(kr,\theta,\phi) = \frac{(-\mathrm{j})^{n}}{4\pi}\gamma_{mn}\int_{4\pi}\mathrm{d}\Omega'\mathrm{e}^{\mathrm{j}kr\hat{r}\hat{r}'}\boldsymbol{C}_{mn}(\theta',\phi') \tag{A.5b}$$

$$Rg\boldsymbol{N}_{mn}(kr,\theta,\phi) = \frac{(-\mathrm{j})^{n-1}}{4\pi}\gamma_{mn}\int_{4\pi}\mathrm{d}\Omega'\mathrm{e}^{\mathrm{j}kr\hat{r}\hat{r}'}\boldsymbol{B}_{mn}(\theta',\phi') \tag{A.5c}$$

where Ω' is the surface and θ', ϕ' are the angular variables that indicate the direction $\hat{r}'$.

A.1 Scattering

Let the sphere be centered at the origin and the incident wave be along the $\hat{z}$ direction($\hat{k}_i = \hat{z}$). The observation direction $\hat{k}_s$ be in the $y-z$ plane, with $\phi = 90$ degree(figure A.1). With the aid of (A.5a) through (A.5c) it is now possible to express an incident electromagnetic

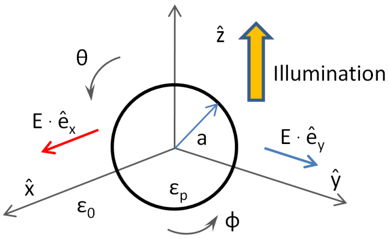

Figure A.1: Geometry of a sphere with radius a and a dielectric constant of ϵ_p. The incident wave propagates in the $+\hat{z}$ direction.

plane wave propagating in the $\hat{z}$ direction and the polarization vector $\hat{e}_i$ by

$$\boldsymbol{E}_i = \hat{e}_i \mathrm{e}^{\mathrm{j}kz} = -\sum_{n=1}^{\infty}\sum_{m=-1,1} \mathrm{j}^n \frac{(2n+1)}{n(n+1)} \left[\frac{\hat{e}_i \cdot \boldsymbol{C}_{-mn}(0,0)}{\gamma_{mn}} Rg\boldsymbol{M}_{mn}(kr,\theta,\phi) - \frac{\hat{e}_i \cdot \boldsymbol{B}_{-mn}(0,0)}{\gamma_{mn}} Rg\boldsymbol{N}_{mn}(kr,\theta,\phi) \right] \tag{A.6}$$

considering that $\boldsymbol{B}_{-mn}(\theta=0,\phi) = \boldsymbol{C}_{-mn}(\theta=0,\phi) = 0$ unless $m = \pm 1$. Since the fields $\boldsymbol{E}$ and $\boldsymbol{H}$ are purely solenoidal, it is sufficient to expand them in terms of $\boldsymbol{M}$ and $\boldsymbol{N}$ alone. If, however, the divergence of the function does not vanish, terms in $\boldsymbol{L}$ must be included.

To solve the boundary problem the scattered field can be expanded by

$$\boldsymbol{E}_s = -\sum_{n=1}^{\infty}\sum_{m=-1,1} \mathrm{j}^n \frac{(2n+1)}{n(n+1)} \left[\frac{\hat{e}_i \cdot \boldsymbol{C}_{-mn}(0,0)}{\gamma_{mn}} b_n \boldsymbol{M}_{mn}(kr,\theta,\phi) + \frac{\hat{e}_i \cdot \boldsymbol{B}_{-mn}(0,0)}{\gamma_{mn}} a_n \boldsymbol{N}_{mn}(kr,\theta,\phi) \right] \tag{A.7}$$

and the internal field by

$$\boldsymbol{E}_{\mathrm{int}} = -\sum_{n=1}^{\infty}\sum_{m=-1,1} \mathrm{j}^n \frac{(2n+1)}{n(n+1)} \left[\frac{\hat{e}_i \cdot \boldsymbol{C}_{-mn}(0,0)}{\gamma_{mn}} d_n Rg\boldsymbol{M}_{mn}(k_p r,\theta,\phi) - \frac{\hat{e}_i \cdot \boldsymbol{B}_{-mn}(0,0)}{\gamma_{mn}} c_n Rg\boldsymbol{N}_{mn}(k_p r,\theta,\phi) \right] \tag{A.8}$$

Note that the wavenumber for the internal field k_p is different to the wavenumber outside the sphere. The factors b_n, a_n and d_n, c_n can be solved by matching the boundary conditions. The boundary conditions are the continuity of $\hat{n} \times \boldsymbol{E}$ and $\hat{n} \times \boldsymbol{H}$ (which is proportional to $\hat{n} \times \nabla \times \boldsymbol{E}$). This leads to the boundary condition at $r = a$, where a is the radius of the sphere

$$\hat{r} \times (\boldsymbol{E}_i + \boldsymbol{E}_s) = \hat{r} \times \boldsymbol{E}_{\mathrm{int}} \tag{A.9a}$$

$$\hat{r} \times (\nabla \times \boldsymbol{E}_i + \nabla \times \boldsymbol{E}_s) = \hat{r} \times \nabla \times \boldsymbol{E}_{\mathrm{int}} \tag{A.9b}$$

b_n, a_n and d_n, c_n can then be solved by comparing the coefficients of $\boldsymbol{M}$ and $\boldsymbol{N}$ considering in (A.9b) that $\nabla \times \boldsymbol{M} = k\boldsymbol{N}$ and $\nabla \times \boldsymbol{N} = k\boldsymbol{N}$. This leads to

$$a_n = -\frac{k_p^2 a^2 j_n(k_p a)\frac{\mathrm{d}[ka j_n(ka)]}{\mathrm{d}r} - k^2 a^2 j_n(ka)\frac{\mathrm{d}[k_p a j_n(k_p a)]}{\mathrm{d}r}}{k_p^2 a^2 j_n(k_p a)\frac{\mathrm{d}[ka h_n(ka)]}{\mathrm{d}r} - k^2 a^2 h_n(ka)\frac{\mathrm{d}[k_p a j_n(k_p a)]}{\mathrm{d}r}} \tag{A.10a}$$

$$b_n = -\frac{j_n(k_p a)\frac{\mathrm{d}[ka j_n(ka)]}{\mathrm{d}r} - j_n(ka)\frac{\mathrm{d}[k_p a j_n(k_p a)]}{\mathrm{d}r}}{j_n(k_p a)\frac{\mathrm{d}[ka h_n(ka)]}{\mathrm{d}r} - h_n(ka)\frac{\mathrm{d}[k_p a j_n(k_p a)]}{\mathrm{d}r}} \tag{A.10b}$$

$$c_n = \frac{\mathrm{j}k_p a}{k_p^2 a^2 j_n(k_p a)\frac{\mathrm{d}[ka h_n(ka)]}{\mathrm{d}r} - k^2 a^2 h_n(ka)\frac{\mathrm{d}[k_p a j_n(k_p a)]}{\mathrm{d}r}} \tag{A.10c}$$

$$d_n = \frac{\mathrm{j}}{ka}\frac{1}{j_n(k_p a)\frac{\mathrm{d}[ka h_n(ka)]}{\mathrm{d}r} - h_n(ka)\frac{\mathrm{d}[k_p a j_n(k_p a)]}{\mathrm{d}r}} \tag{A.10d}$$

In the far field

$$\begin{aligned}\boldsymbol{E}_s = -\frac{\mathrm{j}\mathrm{e}^{\mathrm{j}kr}}{kr}\sum_{n=1}^{\infty}\sum_{m=-1,1}\frac{(2n+1)}{n(n+1)}\{&b_n\left[\hat{e}_i \cdot \boldsymbol{C}_{-mn}(0,0)\right]\boldsymbol{C}_{mn}(\theta,\phi) \\ &+ a_n\left[\hat{e}_i \cdot \boldsymbol{B}_{-mn}(0,0)\right]\boldsymbol{B}_{mn}(\theta,\phi)\}\end{aligned} \tag{A.11}$$

Setting for the Legendre functions

$$\pi_n(\cos\theta) = -\frac{P_n^1(\cos\theta)}{\sin\theta}$$

$$\tau_n(\cos\theta) = -\frac{\mathrm{d}P_n^1(\cos\theta)}{\mathrm{d}\theta}$$

and considering the special case when $\cos\theta = \pm 1$, where $\pi_n(1) = \tau_n(1) = \frac{n(n+1)}{2}$ and $\pi_n(-1) = -\tau_n(-1) = (-1)^{n+1}\frac{n(n+1)}{2}$ the vector spherical harmonics for $m+1$ can also be expressed as

$$\begin{aligned}\boldsymbol{B}_{1n}(\theta,\phi) &= -\left[\hat{\theta}\tau_n(\cos\theta) + \hat{\phi}\,\mathrm{j}\pi_n(\cos\theta)\right]\mathrm{e}^{\mathrm{j}\phi} \\ \boldsymbol{C}_{1n}(\theta,\phi) &= -\left[\hat{\theta}\,\mathrm{j}\pi_n(\cos\theta) - \hat{\phi}\tau_n(\cos\theta)\right]\mathrm{e}^{\mathrm{j}\phi}\end{aligned} \tag{A.12a}$$

and for $m = -1$

$$\begin{aligned}\boldsymbol{B}_{-1n}(\theta,\phi) =& \frac{1}{n(n+1)}\left[\hat{\theta}\tau_n(\cos\theta) - \hat{\phi}\,\mathrm{j}\pi_n(\cos\theta)\right]\mathrm{e}^{-\mathrm{j}\phi} \\ \boldsymbol{C}_{-1n}(\theta,\phi) =& -\frac{1}{n(n+1)}\left[\hat{\theta}\,\mathrm{j}\pi_n(\cos\theta) + \hat{\phi}\tau_n(\cos\theta)\right]\mathrm{e}^{-\mathrm{j}\phi}\end{aligned} \tag{A.12b}$$

For $\theta = 0$, without loss of generality $\phi = 0$ and

$$\begin{aligned}
\boldsymbol{B}_{1n}(0,0) &= -\frac{n(n+1)}{2}\left(\hat{\theta} + \mathrm{j}\hat{\phi}\right)\mathrm{e}^{\mathrm{j}\phi} = -\frac{n(n+1)}{2}\left(\hat{x} + \mathrm{j}\hat{y}\right) \\
\boldsymbol{C}_{1n}(0,0) &= -\frac{n(n+1)}{2}\left(\mathrm{j}\hat{\theta} - \hat{\phi}\right)\mathrm{e}^{\mathrm{j}\phi} = -\mathrm{j}\frac{n(n+1)}{2}\left(\hat{x} + \mathrm{j}\hat{y}\right) \\
\boldsymbol{B}_{-1n}(0,0) &= \frac{1}{2}(\hat{x} - \mathrm{j}\hat{y}) \\
\boldsymbol{C}_{-1n}(0,0) &= -\frac{\mathrm{j}}{2}\left(\hat{x} - \mathrm{j}\hat{y}\right)
\end{aligned} \tag{A.13}$$

With (A.12a), (A.12b) and (A.13), equation (A.11) summing over $m = 1, -1$ can thus be written

$$\begin{aligned}
\boldsymbol{E}_s = -\frac{\mathrm{j}\mathrm{e}^{\mathrm{j}kr}}{2kr}\sum_{n=1}^{\infty}\frac{(2n+1)}{n(n+1)}\Big\{&-a_n\left[\hat{e}_i\cdot(\hat{x} - \mathrm{j}\hat{y})\right]\left[\hat{\theta}\tau_n(\cos\theta) + \hat{\phi}\,\mathrm{j}\pi_n(\cos\theta)\right]\mathrm{e}^{\mathrm{j}\phi} \\
&- a_n\left[\hat{e}_i\cdot(\hat{x} + \mathrm{j}\hat{y})\right]\left[\hat{\theta}\tau_n(\cos\theta) - \hat{\phi}\,\mathrm{j}\pi_n(\cos\theta)\right]\mathrm{e}^{-\mathrm{j}\phi} \\
&+ \mathrm{j}b_n\left[\hat{e}_i\cdot(\hat{x} - \mathrm{j}\hat{y})\right]\left[\hat{\theta}\,\mathrm{j}\pi_n(\cos\theta) - \hat{\phi}\tau_n(\cos\theta)\right]\mathrm{e}^{\mathrm{j}\phi} \\
&+ \mathrm{j}b_n\left[\hat{e}_i\cdot(\hat{x} + \mathrm{j}\hat{y})\right]\left[\hat{\theta}\,\mathrm{j}\pi_n(\cos\theta) + \hat{\phi}\tau_n(\cos\theta)\right]\mathrm{e}^{-\mathrm{j}\phi}\Big\}
\end{aligned} \tag{A.14}$$

One can now set the field along the axis and from (A.14) for $\hat{e}_i = \hat{x}$, $\phi = 90°$

$$\boldsymbol{E}_s = -\frac{\mathrm{j}\mathrm{e}^{\mathrm{j}kr}}{kr}\hat{\phi}\sum_{n=1}^{\infty}\frac{(2n+1)}{n(n+1)}\left[a_n\pi_n(\cos\theta) + b_n\tau_n(\cos\theta)\right]$$

and for polarization in $\hat{e}_i = \hat{y}$, $\phi = 90°$

$$\boldsymbol{E}_s = \frac{\mathrm{j}\mathrm{e}^{\mathrm{j}kr}}{kr}\hat{\theta}\sum_{n=1}^{\infty}\frac{(2n+1)}{n(n+1)}\left[a_n\tau_n(\cos\theta) + b_n\pi_n(\cos\theta)\right]$$

and thus for the unpolarized

$$\boldsymbol{E}_s = \frac{\mathrm{j}\mathrm{e}^{\mathrm{j}kr}}{kr}\left[\hat{\theta}S_2(\theta)\cos\phi - \hat{\phi}S_1(\theta)\sin\phi\right] \tag{A.15}$$

where

$$\begin{aligned}
S_1(\theta) &= \sum_{n=1}^{\infty}\frac{(2n+1)}{n(n+1)}\left[a_n\pi_n(\cos\theta) + b_n\tau_n(\cos\theta)\right] \\
S_2(\theta) &= \sum_{n=1}^{\infty}\frac{(2n+1)}{n(n+1)}\left[a_n\tau_n(\cos\theta) + b_n\pi_n(\cos\theta)\right]
\end{aligned}$$

The scattering cross section can then be calculated by integrating the total scattered power $(E_s)^2$ around the sphere

$$\sigma_s = \frac{\pi}{k^2}\int_0^{\pi}\mathrm{d}\theta\sin\theta\left(|S_1(\theta)|^2 + |S_2(\theta)|^2\right) = \frac{2\pi}{k^2}\sum_{n=1}^{\infty}(2n+1)\left(|a_n|^2 + |b_n|^2\right) \tag{A.16}$$

Appendix B

Influence of diffusion layer on the LSPR shift

The refractive index of the diffusion layer was approximated by the Clausius-Mosotti relation:

$$\frac{n^2-1}{n^2+2} = \frac{4\pi}{3}\sum_i (N_i \alpha_i) \tag{B.1}$$

N is the concentration and α is the polarizability of the molecule/atom/ion. For Cl^- a polarizability of 3.65 Å^3 and for Na^+ a polarizability of 0.086 Å^3 was used [79]. Both values are for hydrated ions. Considering a density for pure water of 998 kg/m^3 at 20 °C the concentration of H_2O in pure water is $c_{\text{pure}} = 55.4\,\text{M}$ and a polarizibility of H_2O of 1.47 Å^3. The refractive index n can therefore be calculated from equation (B.1) when the ion and water concentration are known.

Relating to the theory of Gouy-Chapman of the diffusive layer (see also 2.2.2) the potential drop $\Phi(z)$ in the diffusive layer for 1:1 salts like NaCl, is given by:

$$\Phi(z) = \frac{2kT}{e}\log\left(\frac{1+\gamma \mathrm{e}^{-\kappa z}}{1-\gamma \mathrm{e}^{-\kappa z}}\right) \tag{B.2}$$

where k is the Boltzmann constant, T the absolute temperature, e the elementary charge, κ^{-1} the Debye length and γ is related to the surface potential ψ_0:

$$\gamma = \tanh\left(\frac{e\psi_0}{4kT}\right) \tag{B.3}$$

In the presence of a Stern layer, the potential drop over the Stern layer should be subtracted from the surface potential to yield ψ_0. The Debye length can be calculated from the bulk concentration c_{bulk} by

$$\kappa^{-1} = \sqrt{\frac{\epsilon_0\epsilon_r RT}{2F^2 c_{\text{bulk}}}} \tag{B.4}$$

where R is the Gas constant, F the Faraday constant, ϵ_0 the dielectric constant of free space and ϵ_r the dielectric constant of the medium.

The concentration of ions in the diffusive layer can be assumed to follow a Boltzmann distribution and therefore

$$c(z) = c_{\text{bulk}} \mathrm{e}^{\pm \frac{e\Phi(z)}{kT}} \tag{B.5}$$

Any change in the concentration of ions would change the concentration of water. The concentration of water can be estimated by assuming that each ion blocks a volume (V_{Cl^-} and V_{Na^+}) equal to a sphere with a radius of the dry ion. The dry ion radii were assumed to be $r_{textCl^-} = 1.8\,\text{Å}$ and $r_{\text{Na}^+} = 0.9\,\text{Å}$ [79]. The water concentration can then be calculated by

$$c_{\text{H}_2\text{O}} = c_{\text{pure}} \left(1 - c_{\text{Cl}^-} V_{\text{Cl}^-} - c_{\text{Na}^+} V_{\text{Na}^+}\right) \tag{B.6}$$

In reality this approximation leads to a small underestimation of the water concentration (and therefore also to an underestimation of the absolute value of the refractive index n), since the volume excluded by dissolved NaCl is about 10 % larger in reality and only slightly dependent on the concentration of NaCl [97]. With the known change of concentration over the distance the refractive index n can then be expressed as a function of the distance z via equation (B.1).

Furthermore the sensitivity S of the LSPR as a function of the distance z can be written as

$$S(z) = \frac{m}{\delta} \mathrm{e}^{-\frac{z}{\delta}} \tag{B.7}$$

assuming an exponential decay of the sensitivity distribution (see also 2.1.5). In equation (B.7) m is the bulk sensitivity (in nm/RIU), and δ is the decay length of the sensitivity. Both m and δ can be determined experimentally by adsorbing layers with known thickness and refractive index. Finally the resulting peak shift due to the diffusive layer is then calculated as

$$\Delta\lambda_{peak} = \int_0^{\infty} \Delta n(z) S(z)\,\mathrm{d}z \tag{B.8}$$

Δn is the change of refractive index versus the bulk liquid refractive index, *i.e.* it is assumed that $c(z) = c_{\text{bulk}}$ when no potential is applied.

However for the peak shift of gold spheres, values of m and δ are typically 50–60nm/RIU and 10 nm respectively. For a potential of 100 mV (at potentials higher than 100 mV the predicted concentrations of Cl^- are no longer reasonable, since they are already higher than that of saturated NaCl) a resonance peak shift of ∼0.1 nm is predicted, which would be detectable but can not explain the observed peak shift in chapter 4.